Study of a MEMS Laser Range Finder: Integration, Performance and Design of a 2-Axis Mirror Control System

by

Daniel L. Zelazo

B.S., Electrical Science and Engineering (1999)
Massachusetts Institute of Technology

Submitted to the Department of Electrical Engineering and Computer Science
In Partial Fulfillment of the Requirements for the degree of

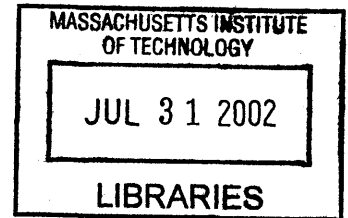## Master of Engineering in Electrical Engineering and Computer Science

at the

Massachusetts Institute of Technology

February 6, 2001

Author.........................
Department of Electrical Engineering and Computer Science
February 6, 2001

Certified by....................................
Dr. Mark Mescher
Senior Member of the Technical Staff, C.S. Draper Laboratory
Draper Laboratory Thesis Supervisor

Certified by....................................
Professor Jeffery H. Lang
Professor of Electrical Engineering and Computer Science
M.I.T. Thesis Supervisor

Accepted by....
~Arthur C. Smith
Chairman, Department Committee on Graduate Theses

Study of a MEMS Laser Range Finder: Integration, Performance and Design of a 2-Axis Mirror Control System

by

Daniel L. Zelazo

Submitted to the
Department of Electrical Engineering and Computer Science

February 6, 2001

In Partial Fulfillment of the Requirements for the Degree of
Master of Engineering in Electrical Engineering and Computer Science

Abstract

This thesis studies the feasibility of a microelectromechanical (MEMS) laser range finder. A MEMS laser range finder offers significant improvement in size, weight, and power consumption over traditional laser scanning devices. A detailed model of the mechanical and electrical dynamics of the MEMS system was developed and verified with experimental measurements. In addition, a controller was designed, implemented, and tested to control the outer axis rotation speed and the inner axis scan amplitude. The thesis explores the major issues and problems in the design of a 2-axis control system and offers suggestions for improvements.

Thesis Supervisor: Mark Mescher
Title: Senior Member of the Technical Staff, C.S. Draper Laboratory

Thesis Supervisor: Professor Jeffrey H. Lang
Title: Professor of Electrical Engineering and Computer Science

3

Acknowledgments

This thesis project embodies a compressed version of my educational experience. My academic journey has by no means been an individual effort. Rather, it has been a conglomeration of personal effort and external complimentary forces. It is a complex union between my relationships with my family, friends, and teachers. Without these forces, my education would be meaningless, and probably worthless.

Therefore, I cannot submit this work without thanking those people who were involved in its creation. I must offer a general thanks to Draper Laboratory for giving me the opportunity to do my graduate work at their lab. It was an amazing experience in every way, and the experiences I gained at Draper will undoubtedly guide me through my career as an engineer.

Dr. Mark Mecher, one of my Draper supervisors, has been there through the duration of this project. He has helped me along the way in every facet of this project. Our informal discussions on the details of this project were often more educational then many courses I have taken, and were always conducted in a jovial manner (regardless of the reality of the situation). Mark also has the unique distinction of being my only supervisor to stay at Draper for the duration of my entire fellowship, a feat in itself given my record.

On that note, I would like to thank my advisors of the past who are no longer at Draper. I would like to thank Atif Chaudhry for his help throughout the project, and his constant reminder to me of the pleasures of graduate school. Atif made sure I realized my fortunate position as a Draper fellow, and that was invaluable throughout the process. Dr. Jon Bernstien was the brain behind the LIDAR project. Although we only worked together very briefly, it was very educational watching an amazing engineer at work. Finally, Mike Piedmonte was the first Draper supervisor to take me on. He left before I found my project, but was instrumental in introducing me to important people at Draper.

In addition to the support I received from my supervisors, many other staff members also took time to help me in my endeavors. Specifically, I would like to thank Brent Appleby, Amy Duwel, Brad Blanchard, Chris Dever, Greg Kirkos, and Will McFarland Jr. for their extraordinary effort in helping me. Whether through informal discussions or technical instruction, they truly went above and beyond in walking me through my questions. I also would like to give a special thanks to Tony Emberley and Bob Visser in the Electromagnetic Lab for putting up with me for as long as they did. From teaching me how to use the electromagnet winding machine to putting up with my empty coke bottles, they were a real pleasure to work with. The Central Machine Shop also did a wonderful job machining the prototype. Finally, I would like to thank the Fiber Optics Lab for allowing me to camp out there and use their equipment.

At M.I.T., I would like to thank Prof. Lang for his involvement in my project. I would also like to thank all the other professors at the institute for inspiring me and helping me find my true passions in engineering.

Outside of the academic world, my family and friends were a constant source of support for me. Words cannot express my feelings towards my family. Abba, you instilled me with the notion of curiosity, the joys of science, and the true meaning of ∞. Emma, you have always been my emotional inspiration, teaching me the importance of family and spirituality. Maya and Eyton, thanks for making me laugh and letting me be my uncensored self in front of you. It has been more valuable then you may imagine. Grandpa, you taught me that education is a life long process and is not limited by the books I read and the exams I take. Those are only supplements to the people I interact with and my abilities to observe my surroundings. Thank you.

Without my friends, I would have no reason to work as hard as I did. I always looked forward to hanging out with my friends. Whether it was sharing a beer at the Thirsty Ear, biking across the country, skiing the Alps, exploring the meaning of life, or just sharing the perfect plate of nachos, my friends were always there for me, and complimented me in every way. My personal growth is a result of their companionship. Thank you.

I would like to dedicate this thesis to my Grandmother, Helene Zelazo, and my Grandfather, Akiva Macagon. My love will always be with them.

February 6, 2001

This thesis was prepared at the Charles Stark Draper Laboratory, Inc., under Independent Research and Development Project 13090.

Publication of this thesis does not constitute approval by Draper Laboratory of the findings or conclusions contained therein. It is published for the exchange and stimulation of ideas.

<div align="right">
Daniel L. Zelazo
</div>

Contents

5   Outer Axis Control   57

6   Inner Axis Control   67

7   Experimental Measurements and Results   89

8   Conclusions   97

List of Figures

List of Tables

Chapter 1

Introduction

Tactical autonomous vehicles are becoming smaller and can maneuver more aggressively with every generation. However, the effectiveness of these vehicles are often limited by the sensors that allow them to navigate autonomously. The size, power, and resolution of a sensor pose a significant constraint on the vehicle's design and capabilities. Today's silicon world offers the opportunity for these sensors to become smaller, more power efficient, and ultimately more suitable for small autonomous vehicles.

The range finder is a crucial sensor for any autonomous vehicle. Range finders produce 3-dimensional maps of an environment that are used by the vehicle for obstacle avoidance and target recognition. Range finders come in many forms including laser, radar, sonar, and ultrasonic. This thesis explores the feasibility of a micro-scanning laser range finder, or LIDAR.

The motivation behind the development of a LIDAR system is precisely due to the reasons mentioned above. Most existing scanning laser range finders are large and power hungry. The LIDAR system uses microelectromechanical systems (MEMS) technology to reduce the size, and subsequently, the weight and power consumption of a scanning laser range finder.

The remainder of this introduction will present a short review of existing scanning laser range finders. This will be compared to the LIDAR system being developed at Draper Labs. A system overview of the LIDAR, along with the goals of this thesis project will also be explained.

1.1   Scanning Laser Range Finders: Today's Options

Today's scanning laser range finders can be categorized depending on their actuation mechanisms, size and construction, and sensing and control methods.

Electro-optic and acousto-optic scanners are characterized by relatively high scan speed capability but relatively small scan angles. Independent control of two scanning axes is non-trivial. They can be small to moderate in size with modest power requirements; however, high voltages are typically required for large-aperture devices, which is a significant constraint for small vehicles. Insufficient scan angle is the primary technical constraint precluding them from consideration.

Electrostatically actuated MEMS mirrors have also been extensively researched [8] and are being developed for a large number of scanning applications. However, because of the inverse relationship between force and the air gap across which the actuating voltage is applied, large devices with substantial scan angles have not been realized. Several schemes using wafer thick comb drives [2] show promise for achieving large, high angle devices, however, there are multiple technical hurdles.

Magnetically-actuated MEMS-fabricated scanners have also been investigated [11]. A typical configuration consists of a mirror onto which a coil of wire is deposited (electroplated, etc.). Passing an alternating current through the coil generates a torque in the presence of an external magnetic field. Limitations on metal thickness result in high resistive losses in the coil and thus poor efficiency. Stresses in the metal and insulating

layers can generate significant curvature in the mirror surface, degrading the optical quality.

There are also many non-MEMS scanners currently in wide use. Traditional rotating-polygon scanners rely on high-speed motors and are limited in their scanning motions. They typically achieve two-axis scanning through two separate, orthogonal single-axis scanners, which sacrifices size, power, and control simplicity.

Galvanometer-based scanners are also common. They can operate at high speeds (kHz range), have excellent angle resolution and low wobble and jitter. However, they are large, heavy, and consume large amounts of power.

Magnetically driven resonant mode mirrors are also widely available. They operate at a fixed frequency and can have a variety of feedback mechanisms. They typically have long torsion-mode springs that add significantly to their size. The rotational inertial of these systems are also large relative to MEMS scanning mirrors, and consequently their drive electronics are larger and consume more power. These scanning systems have substantial scan angles (exceeding 20°) and operate at modest power levels (1 – 20 Watts). These scanners would be viable candidates for mobile LIDAR applications if the size and power requirements were substantially reduced.

1.2   The LIDAR Solution

The LIDAR solution is an attempt to optimize all of the aforementioned constraints for a scanning laser range finder. The prototype developed at Draper Laboratory demonstrated low power, size, and weight. The main advantage of Draper's LIDAR is the development of a single 2-axis MEMS micro-mirror. A photograph of the MEMS mirror assembly used in the prototype is given in Figure 1-1.
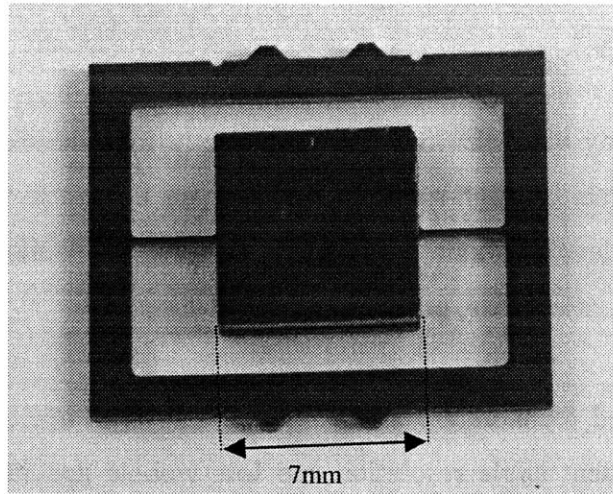
Figure 1-1: MEMS mirror with flexures and embedded magnet

The MEMS mirror uses electromagnetic actuation for the fast scan axis, referred to as the inner axis. The actuation is achieved by placing the MEMS assembly inside the air gap of an electromagnet. The MEMS assembly has an embedded permanent magnet. The magnetic field generated by the electromagnet produces a torque on the permanent magnet. The flexures in the MEMS assembly cause the mirror to oscillate. The flexures can be designed to achieve an inner axis scan frequency ranging from 100Hz to over 1KHz. By driving the inner axis near or at the resonant frequency (determined by the flexures), the drive power of the system is greatly reduced. The inner axis scan angle is designed to be approximately 25°.

A miniature DC motor with a cam-follower actuates the outer axis. The outer axis scan rate determines the frame rate of the entire scan, and can very from DC to approximately 30Hz. The scan amplitude of the outer axis is approximately 50°. Figure 1-2 shows a photograph of the prototype LIDAR system that was used for this thesis project.
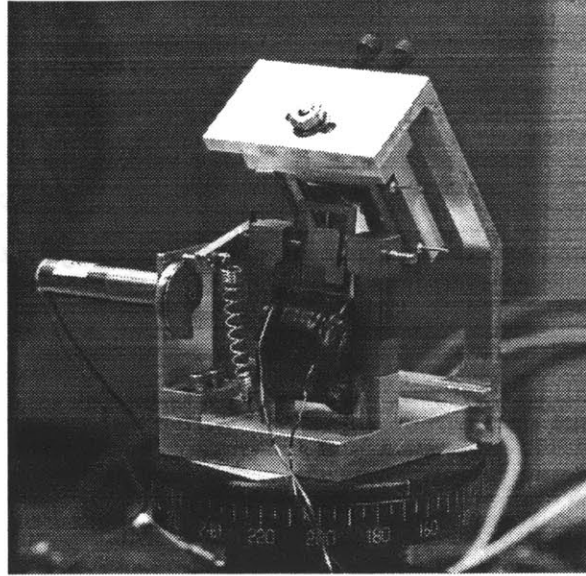
Figure 1-2: LIDAR prototype

1.3 Thesis Goals and Organization

Any scanning laser range finder must be able to maintain its frame rate and scanning amplitude. It is the objective of this thesis to design, implement, and integrate a 2-axis control system for the LIDAR. The system specifications require an outer axis scan rate of 2 Hz, and inner axis scan amplitude of 25°. The inner axis also must scan at a rate that is significantly higher then the outer axis. Therefore, the controller must control the speed of the motor driving the outer axis, and the amplitude of the inner axis scan. The process of developing such a controller is reflected in the organization of this thesis.

Chapter 2 gives a detailed description of the LIDAR prototype. It covers the mechanical properties and physical construction of the LIDAR. Chapter 3 focuses on the sensor used to close the loop of the LIDAR for feedback control. Chapter 4 develops a dynamic model of the 2-axis mirror. Chapter 5 details the control design and implementation for the outer axis. Chapter 6 presents the inner axis control design and implementation. Chapter 7 summarizes the experimental setup and measurements made to test the control.

Finally, chapter 8 concludes this thesis with suggestions for improvement and future development.

Appendices are offered as a supplement to the main text. They provide analyses that help to elaborate subtleties in the main chapters, but are in no way essential to the main body of this thesis.

Chapter 2

Physical Description of LIDAR Prototype

A bench-top test prototype of the MEMS LIDAR system was built to test the performance of the system and the controller. The prototype does not represent an optimized design for the LIDAR system, but rather a workable design that could be quickly developed and produced. Figure 2-1 shows a solid-body conception of the prototype.

DC Motor

Sensor with sensor mount

MEMS mirror

Motor mount with cam, cam follower, and cam arm
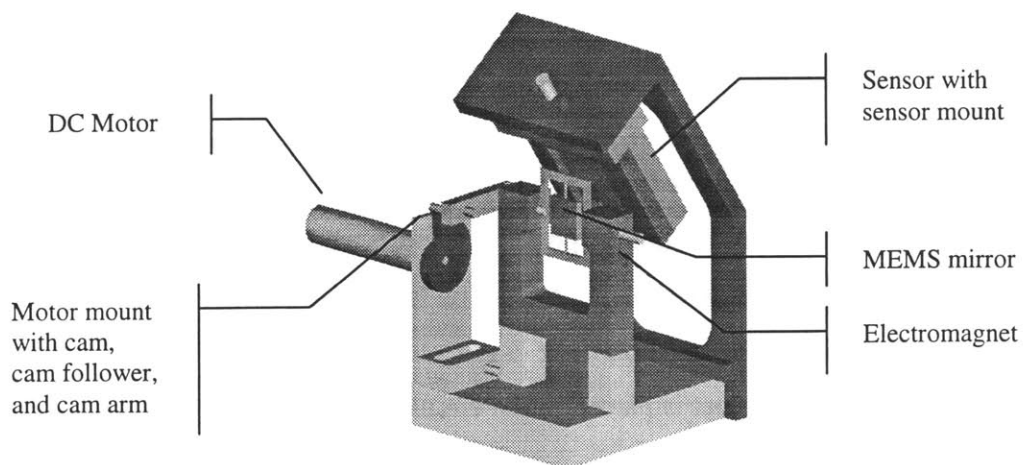
Electromagnet

Figure 2-1: MEMS LIDAR system prototype

The prototype consists of four components: the MEMS mirror, the electromagnet, the sensor mount, and the motor mount with the cam set-up. This chapter will detail each of these components. All of the mechanical drawings can be found in Appendix B.

2.1 MEMS Mirror

The MEMS mirror used in the prototype was designed and fabricated at Draper Labs. The mirror assembly has two main components. The first is the outer frame with the flexure beams and magnet housing. Figure 2-2 shows a drawing of the outer frame.
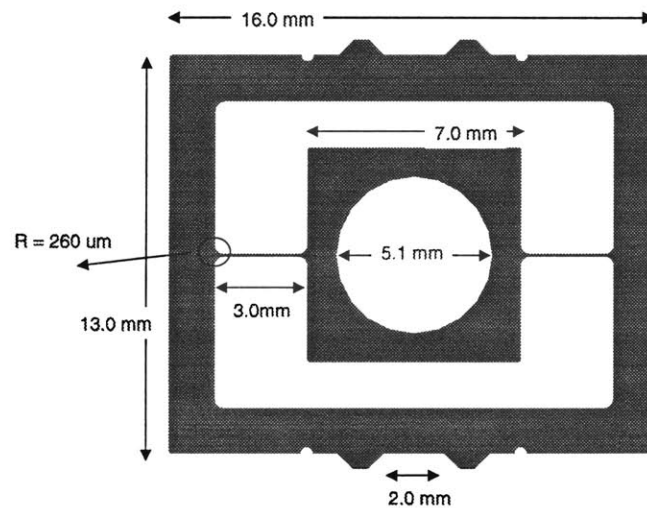
Figure 2-2: Drawing of outer frame of the MEMS mirror

The entire frame is 500 microns thick. The notches on the top and bottom of the frame allow the attachment of an aluminum post. The posts slide through the electromagnet and are attached to the cam assembly. The torsion bars were designed to have a resonant frequency between 200 to 1000 Hz. The inner rectangle is where the mirrors will be attached. A permanent magnet is placed in the circular hole.

The permanent magnet is part of the inner axis actuation scheme. The magnet used was a rare earth magnet. The magnet has a 5mm diameter. The thickness of the magnet was

1.5mm and had to be reduced to 1.0mm to provide a compact assembly. A summary of the permanent magnet characteristics is given in table 2-1.

Material	NdFeB
Diameter	5mm
Thickness	1mm (after reduction)
Density	7.4 g/cm^3
Residual Induction (Br)	1.08 Tesla
Magnetizing Force (Hs)	35000 Oersted

Table 2-1: Summary of permanent magnet properties

The magnet is sandwiched between two rectangular pieces of silicon, each with a polished, metallized mirror-surface on one side. Figure 2-3 shows a drawing of the mirror. The large hole in the middle does not go through the entire thickness of the silicon. It is intended to cover the magnet. The small holes also do not go all the way through and serve two purposes. They allow for the adhesive used to form a stronger bond between the frame and the mirror, and they also reduce the overall inertia of the mirror.

Hole diameter: 250 um
period: 400 um

Holes do not go thru:
(300 um deep)

7.0mm   5.10 mm
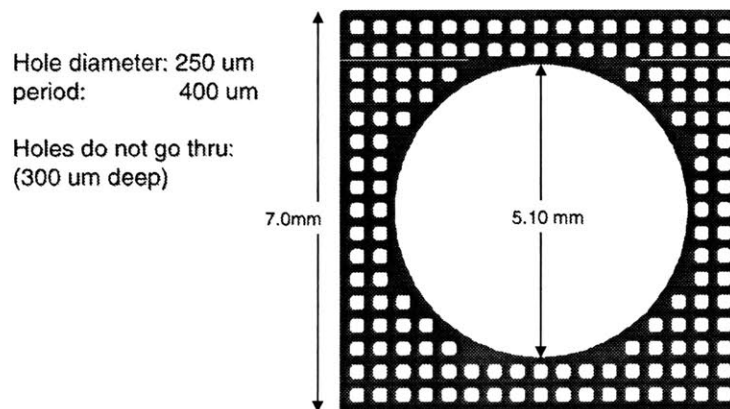
Figure 2-3: Drawing of mirror

The moments of inertia calculation and their values for the outer frame, the magnet, and the mirror are presented in Appendix C.

2.2 Electromagnet

The electromagnet was made from HyMu 80 steel. HyMu 80 has a high permeability, which is desirable for the electromagnet. The magnet core was machined from a solid block and is not laminated. This results in a less efficient electromagnet but is sufficient for the prototype. The electromagnet was manually wound with a 26-gauge (AWG) wire. Approximately 523 turns were wound. The number of turns were limited by the size of the mirror that sits in the magnet gap.

The magnet core rests on two posts to allow room for the volume of the wire turns. Tapped holes were drilled in the bottom to secure the magnet to the base.

2.3 Motor Mount with Cam Assembly

The motor mount has a threaded hole that matches the thread of the motor body. The motor shaft also has a flat that is used to help secure a cam with the use of a setscrew. The cam arm has a steel pin on one end that is used as the cam follower. There is also a pin protruding from the side, and at the bottom of the motor mount so a load spring can be attached. The load spring ensures that the cam arm will always be in contact with the cam. The other end of the cam arm has a clamp hole for the posts that are attached to the MEMS mirror. Moment of inertia calculations for the cam and the cam arm are in Appendix C.

The motor used to drive the outer axis is a Namiki coreless DC motor (7CL-17PG series). The motor has a 105:1 reduction gear box which makes it ideal to drive the outer axis. The characteristic speed-torque and current-torque curves are shown in figure 2-4.
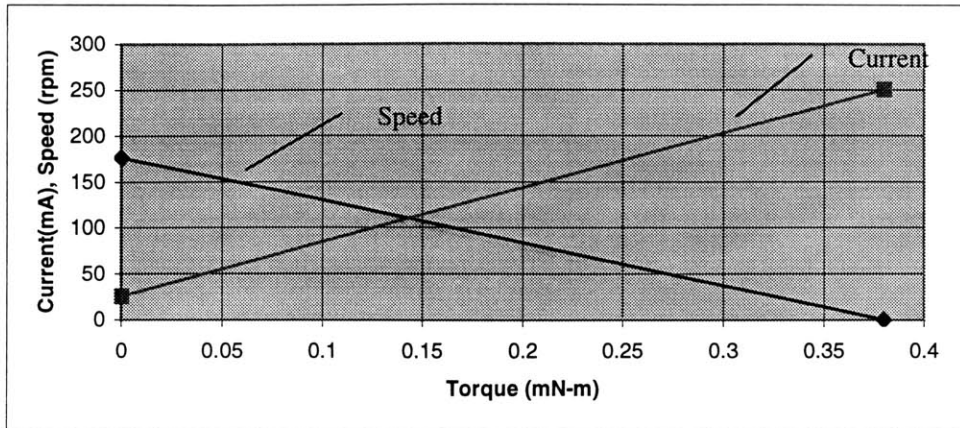
Figure 2-4: Speed –Torque and Current-Torque curves for the DC motor

2.4 Sensor Mount

The sensor mount is composed of two parts. The first is an aluminum block that is attached directly to the sensor with a strong adhesive tape. The block attaches to another mount that attaches to the main base plate. Both the sensor block and the mount have adjustment abilities. The details of the placement of the sensor mount are presented in chapter 3.

Chapter 3

Position Sensitive Detector

The LIDAR system requires a mirror position sensor for closed-loop feedback control. An attractive sensor to use for this application is one that does not add mechanical complexity to the plant or the actuator. For this reason, an optical sensor was chosen. A laser is reflected off the back portion of the MEMS mirror onto the sensor. The sensor outputs a current that is proportional to the distance from the center of the sensor to the actual point where the laser hits the sensor. Figure 3-1 shows a simplified 2-dimensional picture of the set-up.
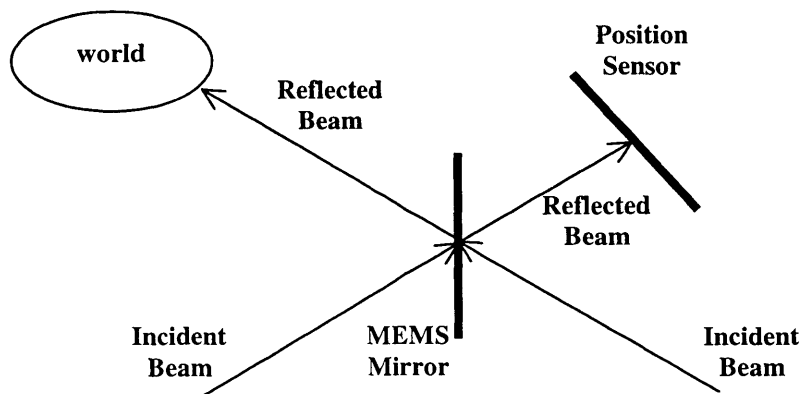
Figure 3-1. Position Sensor and MEMS Mirror Set-up

This section will discuss the details of the position sensor. This includes a model and explanation of how the sensor operates, selection criteria for this application, and physical integration into the whole system.

3.1 Sensor Selection

Selecting the proper sensor for this application involves an understanding of the system components and an idea of what an ideal sensor would provide. For this problem the sensor should be able to provide a high-resolution output corresponding to the position of the MEMS mirror as it oscillates. The sensor should also be a low-power device and have reasonable physical dimensions (relative to the rest of the system).

The laser used to test the system is a 10mW Helium Neon (HeNe) laser with 632.8nm wavelength. The laser can be attenuated and focused to adjust the power and beam diameter as necessary.

The sensor that best matched the requirements of the system was the UDT Duo-Lateral, Super Linear Position Sensitive Detector (PSD) DLS-10. The sensing area for the DLS-10 is 10mm x 10mm. The DLS-10 sensor has position accuracies of 99% over 64% of the sensing areas. The maximum power density allowable for the sensor is 1mW/cm^2. The sensor manufacturer also recommends that the incident beam be perpendicular to the active area with a spot size less than 1mm in diameter. All of the light source requirements can be met with appropriate attenuation and focusing of the HeNe laser.

3.2 Sensor Model

The duo-lateral photodiode operates on the same principle as a normal photodiode. As an incident light source hits the diode, a current is produced. The duo-lateral photodiode is a four terminal device. Each pair of nodes corresponds to one axis. The output current at

each node is proportional to the light source point of contact. Figure 3-2 shows a physical model of the duo-lateral photodiode [5].

The details of the photodiode are very involved, and fortunately can be aptly explained through an analogous circuit model of the device, as shown in figure 3-3 [5]. The P and N layer's resistance act as a current divider, as represented by a variable resistance in the circuit model. The parallel capacitance and resistance result from the properties of a photodiode. The output current at each electrode, as the model suggests, is proportional to the total inter-electrode resistance and distance from where the beam hits the sensor to each electrode.
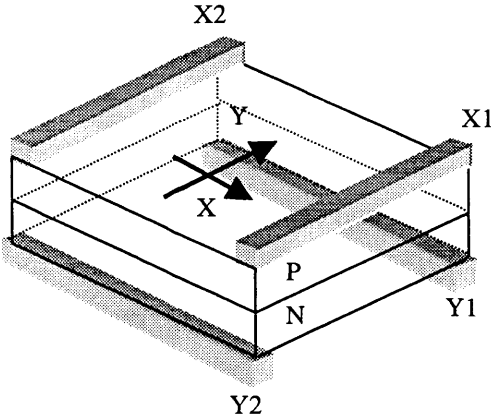
Figure 3-2: Physical representation of a duo-lateral photodiode
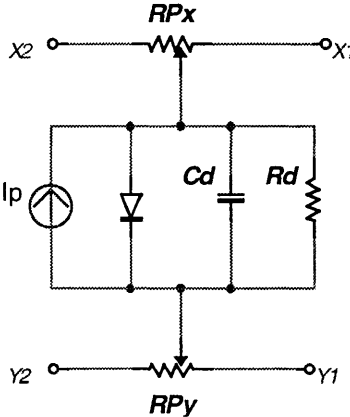
Figure 3-3: Circuit Model of duo-lateral photodiode

For a more in depth analysis of the photodiode, please refer to [5].

3.3   System Integration

There are numerous considerations that must be taken into account when integrating the sensor with the rest of the system.   Specifically, there are physical placement requirements and electrical requirements for the sensor.

3.3.1 Physical Integration

The placement criterion involves determining the optimal position of the sensor relative to the MEMS mirror. The operating requirements for the sensor, the size of the sensing area, and the size of the sensor package, all must be taken into account when determining the sensor placement.

The UDT sensor has position accuracies of 99% over 64% of the sensing area. All of the sensing, if possible, should occur within a square box covering 64% of the area. Figure 3-4 shows the two-dimensional sensing area of the sensor and the region of desired operation for the sensor.
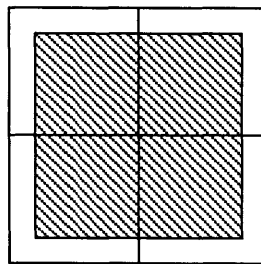
Figure 3-4: Sensing Area. Shaded region represents 64% of sensor area

However, the scan area shown can only be achieved if each axis scans through the same angle. This is not the case with the LIDAR system. Recall that the inner axis sweeps through 12.5° and the outer axis sweeps through 25° resulting in 25° and 50° optical scan of the laser respectively. Determining the distance from the MEMS mirror to the sensor is a straight-forward geometry problem. Figure 3-5 shows the geometry of the setup.
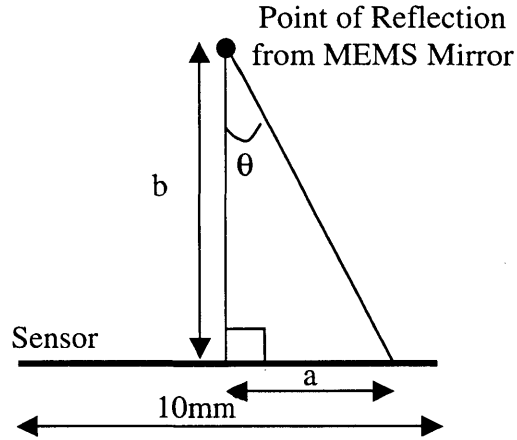
Figure 3-5: Geometry of sensor and mirror for sensor placement calculations

When the mirror is in its nominal (or unperturbed) position, the reflected laser should be normal to the sensor surface, as shown in Figure 3-5. The distance **b** from the point of reflection on the mirror to the center of the sensor depends on the desired sensing area and the angle θ that the laser sweeps. The angle θ is predetermined, and is 12.5° for the inner axis and 25° for the outer axis. The desired sensing area is free to be chosen. Therefore, the distance **b** can be calculated using trigonometry.

$$b = \frac{a}{\tan\theta}$$ (3-1)

Table 3-1 shows how the distance **b** varies with different values for the desired sensing area.

Inner Axis θ=12.5				Outer Axis θ=25			
	100%	90%	80%		100%	90%	80%
a (mm)	5	4.5	4		5	4.5	4
b (mm)	22.55	20.30	18.04		10.72	9.65	8.57

Table 3.1: Distance of Sensor to Mirror

Table 3-1 clearly shows that the distance **b** will be limited by the outer axis rotations. Sensing the position of the inner axis rotations is essential for accurate control so it is desirable to maximize the sensing area along the axis of the inner axis rotations while keeping the entire sensing area as close to the 64% sensing region described in Figure 3-4. Figure 3-6 shows the sensing area as a function of the distance **b** specified in table 3-1 (using the outer axis values).
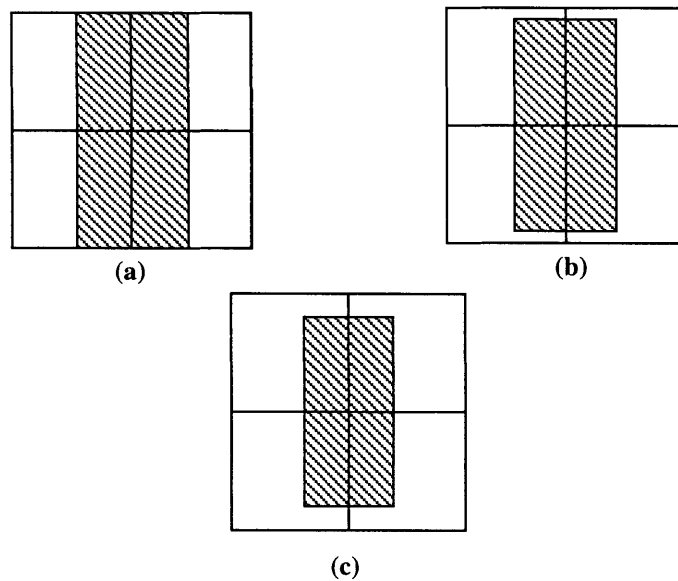
Figure 3-6: Available sensing area as a function of the distance b. (a) 47.6% fill (b) 38.52% fill (c) 15.2% fill

The design tradeoff is sensing area versus the distance from the sensor to the mirror. The closer the sensor is to the mirror the more linear the response, but it also decreases the total available sensing area.

There is another degree of difficulty in the sensor placement that is due to the incident laser beam. Obviously, the incident beam must have an unobstructed path to the mirror. Therefore, an optimal position angle for the sensor must be determined that gives the incident beam a clear path to the mirror, and allows the reflected beam to be normal to the sensor when the mirror is in its nominal position. This problem is also an exercise in geometry. Figure 3-7 shows the physical geometry of the sensor.
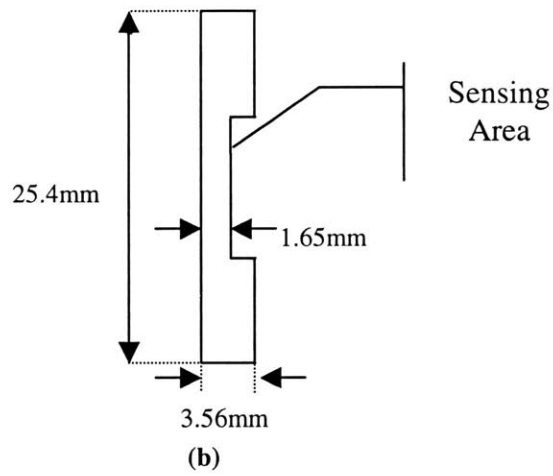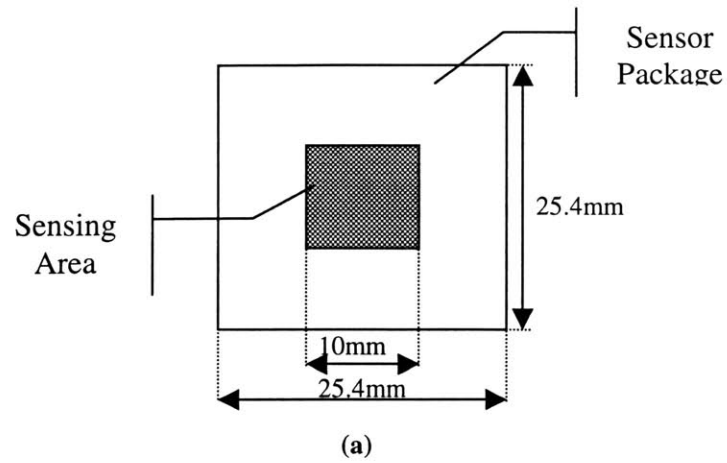
Figure 3-7: Physical Description of Sensor. (a) Top View (b) Cross-Sectional Side View

Figure 3-8 shows the geometry necessary to caclulate the optimal position angle for the sensor.
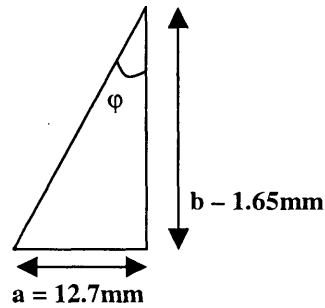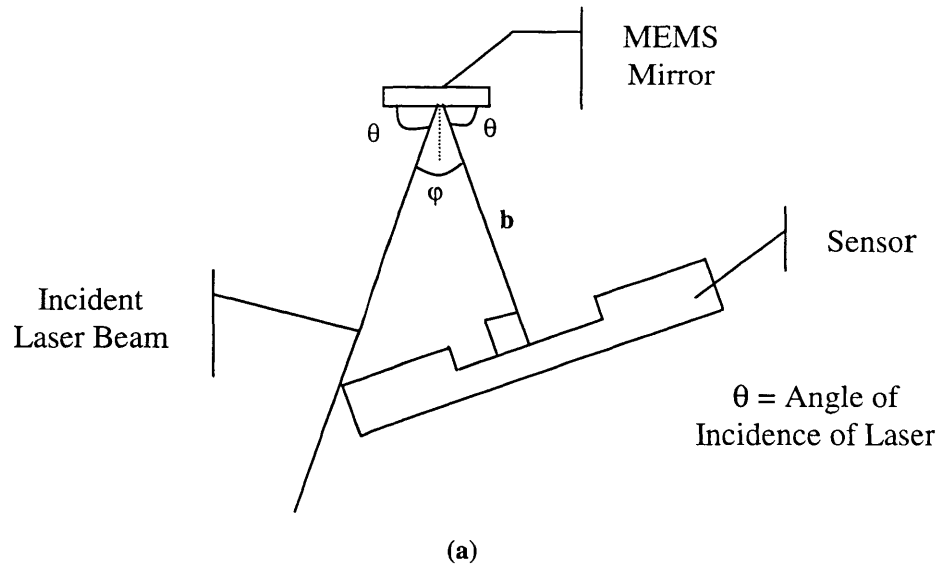
Figure 3-8: Geometry of Sensor with mirror and incident laser beam. (a) Physical picture (b) Simplified triangle of setup

The angles of interest are θ, the angle of incidence of the laser, and ϕ, the angle between the laser and the line normal to the sensor. The angle ϕ is also related to the position angle that the sensor should be placed in. ϕ can be found through a simple trigonometric identity, where the values of **b** are taken from Table 3-1.

$$\varphi = \tan^{-1}\left(\frac{12.7\,\text{mm}}{(b-1.65)\,\text{mm}}\right) \tag{3-2}$$

A subtle design point about tolerances should be made now. The picture in Figure 3-8 shows the incident laser beam just missing the sensor. Calculations from this picture would not allow any error in dimension measurements and set-up. Therefore, it is better engineering to allow a small tolerance on the distance **a**. Equation 3-2 now becomes:

$$\varphi = \tan^{-1}\left(\frac{(12.7 + \varepsilon)\,\text{mm}}{(b - 1.65)\,\text{mm}}\right) \qquad (3\text{-}3)$$

Table 3-2 shows how φ and θ change with **b** and ε.

ε (mm)	b (mm)	θ (degrees)	φ (degrees)
0	10.72	66.04	47.92
	9.65	64.55	50.90
	8.57	62.92	54.16
0.5	10.72	65.74	48.51
	9.65	64.26	51.48
	8.57	62.64	54.72
1	10.72	65.45	49.09
	9.65	63.97	52.05
	8.57	62.36	55.27

Table 3-2: Sensor placement parameters

To allow flexibility, the sensor mount has adjustments that allow both the distance **b** and the angles to change. The nominal position chosen has **b** = 9.65mm with ε = 0.5mm.

3.3.2 Electrical Integration

The electrical integration of the sensor involves determining the necessary electronics to interpret the sensor output and convert the signal into one that can be used with the controller.

As discussed earlier in the sensor model section, the sensor outputs four currents to represent the position of an incident laser onto the sensor. Figure 3-9 shows a simple schematic of the sensor with its output currents.
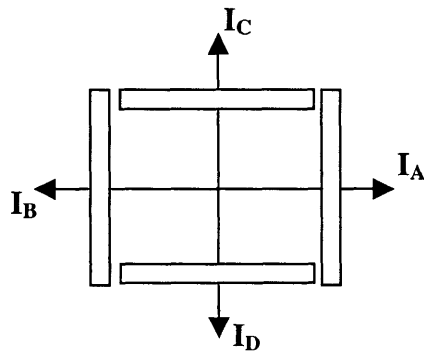
Figure 3-9: Sensor with output currents.

The output currents are typically on the order of μ-Amperes. If the controller is a voltage-controlled system, then the output currents of the sensor must be converted to a voltage. A current to voltage converter circuit can accomplish this. Figure 3-10 shows the schematic for a circuit used to convert current to voltage.

I(A) represents the current produced at one of the nodes of the photodiode. The amplifier also has an offset in order to place a bias on the photodiode. When the photodiode is operated in a reverse-biased mode, there is much more sensitivity to light. The circuit is used for each output node on the sensor. The transfer function from input current to output voltage is given below.
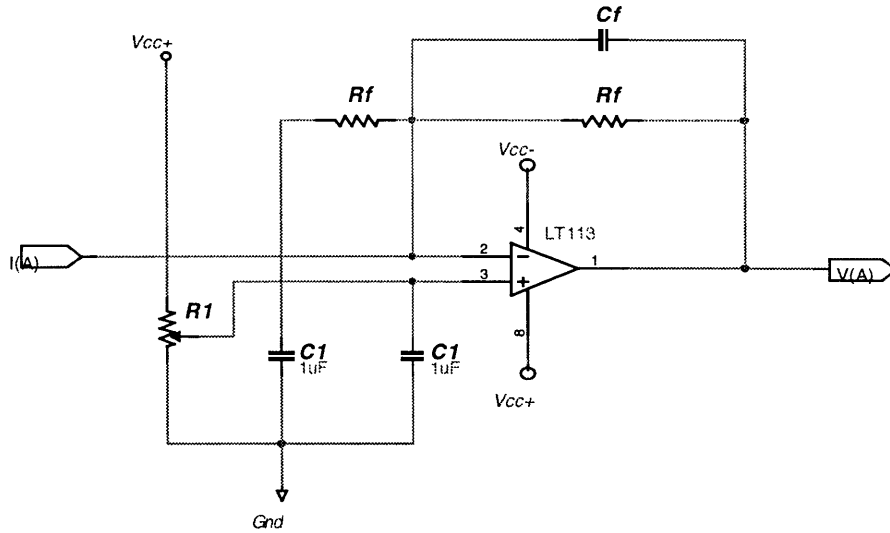
Figure 3-10: Current-to-Voltage converter for the photodiode

$$V(A) = V_b \left(1 + \frac{R_f C_f s}{(R_f C_f s + 1)(R_f C_1 s + 1)} \right) - \frac{R_f}{R_f C_f s + 1} I(A) \quad (3\text{-}4)$$

Using a potentiometer as a voltage divider generates the bias voltage Vb. The anodes should be negatively biased and the cathodes should be positively biased.

The resistor R_f must be large enough to amplify the small current into a workable voltage. For this application, R_f was chosen to be 5.1MΩ. The value for the capacitor C_f is given by the following formula. In the equation, f is the expected frequency that the light source will be moving on the sensor. For this application, f is assumed to be 300Hz.

$$C_f = \frac{1}{2\pi f R_f} \quad (3\text{-}5)$$

$$\approx 0.104nF$$

Once the output currents of the sensor are converted to voltages, another circuit stage must be implemented to convert each of the voltages into a position coordinate. The conversion formulas that relate output current to position are given in equations 3-6 and

3-7. The currents I_A, I_B, I_C, and I_D are all converted to voltage values A, B, C, and D respectively. The voltages are normalized and lie between –0.5 and 0.5 volts in ideal operating conditions.

$$X = \frac{A - B}{A + B} \qquad (3\text{-}6)$$

$$Y = \frac{C - D}{C + D} \qquad (3\text{-}7)$$

Implementation of equations 3-6 and 3-7 involve the use of summing amplifiers and a divider circuit. Figure 3-11 shows a schematic for the implementation of equation 3-6 (the implementation for equation 3-7 is identical). Only one axis is used in the control loop, so the signal processing only needs to be performed with either the cathode or anode voltages (depending on which one corresponds to the inner-axis position).

The divider circuit has a differential input, so only a summing amplifier is needed to produce the denominator. The divider circuit also has a gain of 10 at the output. This gain actually proves to be useful. As mentioned earlier, equations 3-6 and 3-7 produce a normalized output between –0.5 and 0.5 volts. The sensor is 10mm in width, or +/- 5mm from its center point. Multiplying the normalized position by 10 will correspond to its actual position in mm. It is also desirable for the output of the above circuit to represent the angle that the mirror is at, rather then the position of the reflected beam on the sensor. This conversion can be accomplished by choosing appropriate values for the resistor R1-R3. Referring to equation 1, the distance measure can be converted to an angle by using the small angle approximation. Therefore, the denominator in the expression should have a gain of ~9.65 (using the value of B calculated in table 1). Equations 3-8 and 3-9 show how to pick these resistor values. This value is also in mm, so the output of the circuit will now be a unitless value roughly corresponding to the angular position of the mirror.
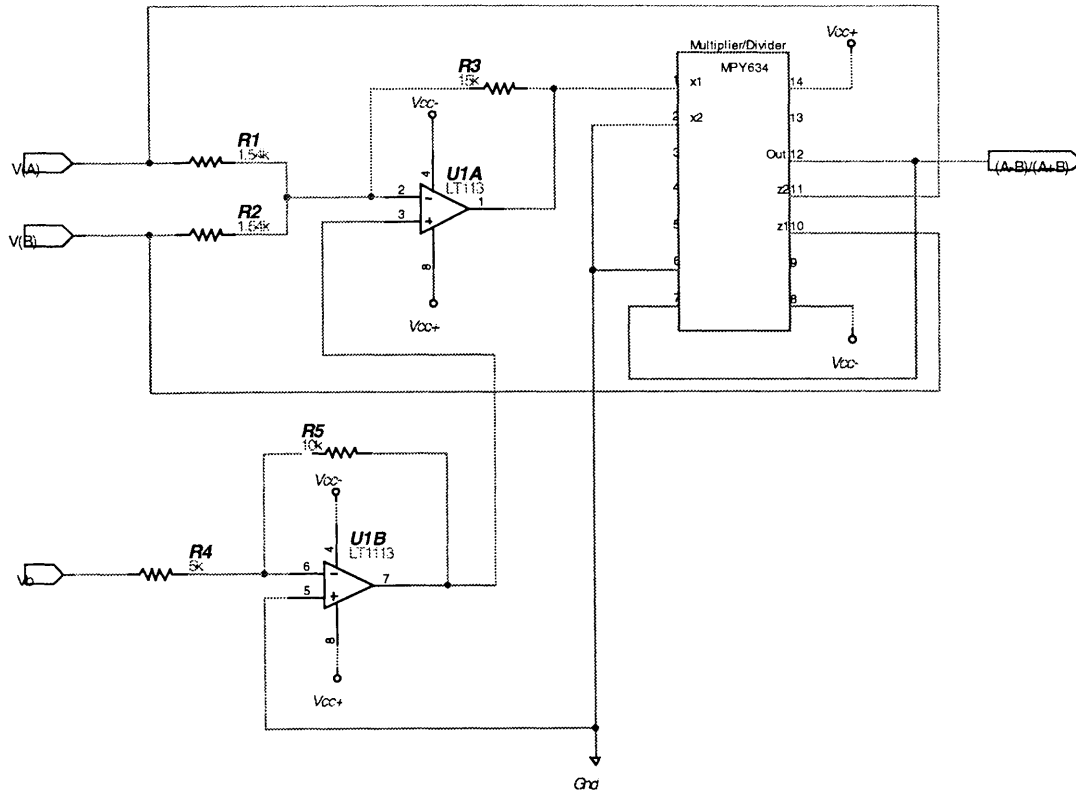
Figure 3-11: Circuit implementation of equation 3-5

$$R1 = R2 \tag{3-8}$$

$$R3 / R1 = 9.65 \tag{3-9}$$

Notice also in the circuit that the summing amplifier is biased by $-2V_b$ using the bias voltage from the current-to-voltage converter. Equation 3-4 shows that the output of the current-to-voltage converter has a frequency dependent function of the bias voltage. Figure 3-12 shows the bode plot of that function. The maximum gain is only 1×10^{-3} dB, and can therefore be assumed to be a unity gain. This term is doubled when it is passed through the summing amplifier (each input to the summing amp has that same bias term). However, the output of the summing amplifier should not be dependent of the bias voltage. Therefore, the bias voltage is passed through an inverting amplifier with a gain of 2. This term will negate the offset created in the current-to-voltage converter.
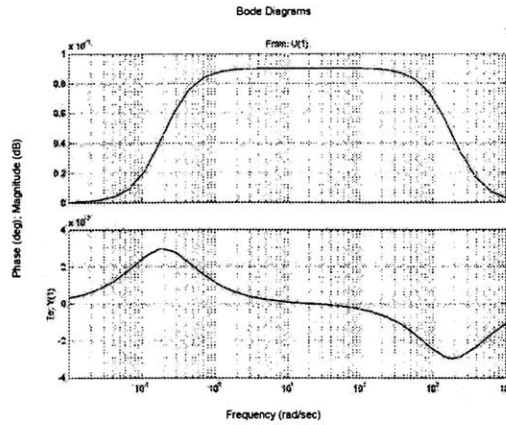
Figure 3-12: Bode plot of frequency dependant term in front of Vb in equation 3-4

The circuits in figures 3-10 and 3-11 combined with the photodiode sensor represent the entire sensor for the system. Using equations 3-4 through 3-7, an input-output relationship for the entire sensor can be written.

$$\theta \cong \frac{10}{9.65} \frac{I_A - I_B}{I_A + I_B} \qquad (3\text{-}10)$$

Note that if the position of the sensor is adjusted, the gain of the summing amplifier must be changed accordingly.

Using the above description, the sensor has no frequency dependency which makes its integration into the control system much easier.

Chapter 4

Dynamic Model of a 2-Axis Mirror

The LIDAR system has two degrees of rotation. In order to gain intuition on the dynamics of the mirror rotations, a study of the force-free dynamics of a 2-axis mirror is necessary. This study does not describe the complete dynamics of the system, but the results will prove useful for the control design. Deriving the equations of motion for the 2-axis mirror can be divided into three steps: 1) Determining the Euler angles for the system 2) Calculation of the moment of inertia of the 2-axis mirror and 3) Derivation of the equations of motion using LaGrangian dynamics. The moment of inertia calculations can be found in Appendix C. The derivation of the Euler angles and the equations of motion are given in the next two subsections.

4.1 Euler Angles and Coordinate Frames

Determining the Euler angles and choosing appropriate coordinate frames for the 2-axis mirror is necessary to efficiently calculate the LaGrange equations of motion. Indeed,

Newton's methods could directly be applied to this problem, but the complicated gyroscopic motion of the system discourages that approach.

Defining appropriate coordinate frames involves choosing an inertial frame and a moving body frame. Figure 4-1 is a simplistic, but sufficient representation of the 2-axis mirror. An associated coordinate frame (the inertial frame) is also shown in this figure.
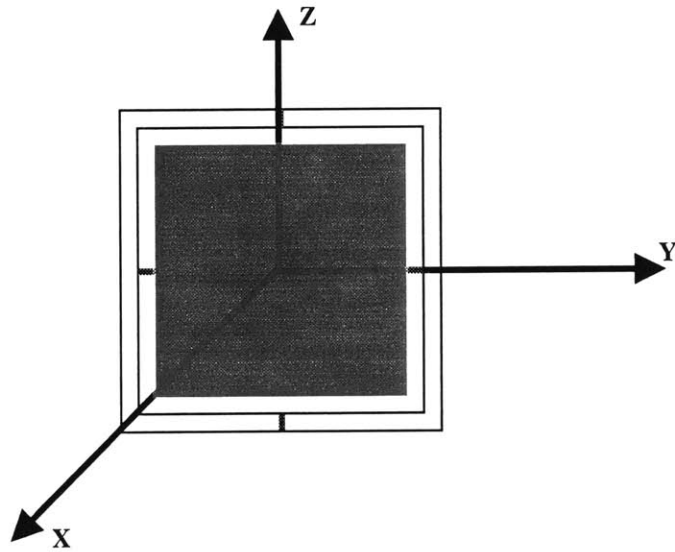
Figure 4-1: 2-Axis mirror

The mirror body (the shaded area in figure 4-1) can only rotate about one axis. The frame that the mirror is attached to can also rotate about one axis. Therefore, there are only two degrees of freedom, and consequently only two Euler angles. The Euler angles will be labeled as $\xi = \begin{bmatrix} \theta & \varphi \end{bmatrix}^T$. Given the Euler angles, the next step is to define proper coordinate frames and the transformation (or rotation) matrices needed to move from one frame to another.

There are three different coordinate frames that must be defined: an inertial coordinate frame, a moving coordinate frame, and a transition coordinate frame. The fixed (inertial)

coordinate frame will be denoted by capital, bold letters X, Y, and Z. The associated directional unit vectors for the fixed frame will be denoted as follows:

$$\hat{U}_{fixed} = \begin{bmatrix} \hat{u}_X & \hat{u}_Y & \hat{u}_Z \end{bmatrix}^T \qquad (4\text{-}1)$$

The transition coordinate frame represents the coordinates of the mirror body after one rotation. The transition coordinate frame will be denoted by lower-case, bold letters with primes: x', y', and z'. The associated directional unit vectors for the transition frame will be denoted as follows:

$$\hat{U}_{trans} = \begin{bmatrix} \hat{u}_{x'} & \hat{u}_{y'} & \hat{u}_{z'} \end{bmatrix}^T \qquad (4\text{-}2)$$

The moving coordinate frame, or the mirror body coordinate frame, will be denoted by the bold, lower-case letters x, y, and z. The associated directional unit vectors for the transition frame will be denoted as follows:

$$\hat{U}_{body} = \begin{bmatrix} \hat{u}_x & \hat{u}_y & \hat{u}_z \end{bmatrix}^T \qquad (4\text{-}3)$$

Moving from one coordinate frame to another is a performed by coordinate transformations, or rotations. The transformation matrices are found through simple geometry and trigonometry. The first possible rotation (counter-clockwise) is about the Z-axis by an angle θ. This rotation transforms the fixed coordinate frame into the transition coordinate frame.

$$\hat{U}_{trans} = \Lambda_\theta \hat{U}_{fixed} \qquad (4\text{-}4)$$

$$\Lambda_\theta = \begin{bmatrix} \cos\theta & -\sin\theta & 0 \\ \sin\theta & \cos\theta & 0 \\ 0 & 0 & 1 \end{bmatrix} \qquad (4\text{-}5)$$

47

The next possible rotation (counter-clockwise) is about the $\mathbf{y}'$-axis by an angle ϕ. This rotation transforms the transition coordinate frame into the mirror body coordinate frame.

$$\hat{\mathbf{U}}_{body} = \Lambda_\varphi \hat{\mathbf{U}}_{trans} \tag{4-6}$$

$$\Lambda_\varphi = \begin{bmatrix} \cos\varphi & 0 & -\sin\varphi \\ 0 & 1 & 0 \\ \sin\varphi & 0 & \cos\varphi \end{bmatrix} \tag{4-7}$$

The fixed coordinate frame can also be transformed into the body coordinate frame by combining the above two transformations.

$$\hat{\mathbf{U}}_{body} = \Lambda_\varphi \Lambda_\theta \hat{\mathbf{U}}_{fixed} = \Lambda_{\varphi\theta} \hat{\mathbf{U}}_{fixed} \tag{4-8}$$

$$\Lambda_{\varphi\theta} = \begin{bmatrix} \cos\varphi\cos\theta & -\cos\varphi\sin\theta & -\sin\varphi \\ \sin\theta & \cos\theta & 0 \\ \sin\varphi\cos\theta & -\sin\varphi\sin\theta & \cos\varphi \end{bmatrix} \tag{4-9}$$

It is also worth noting that rotation matrices have the following useful property:

$$\Lambda^{-1} = \Lambda^{T} \tag{4-10}$$

The results from this discussion will appear again in the moment of inertia calculations.

4.2   LaGrangian Dynamic Analysis

The last step in the analysis is to derive the Lagrangian Equations. The LaGrange method for deriving the equations of motion of a system is a very efficient method. It

draws heavily on the Euler angle calculations made earlier. The Euler angles will be referred to as the generalized coordinates for this system.

The first and most important step in the Lagrangian analysis is to calculate the energy of the system. The energy of a system contains two parts: kinetic energy and potential energy. Hamilton's Principle leads to the creation of an energy function, known as the Lagrangian. The Lagrangian (L) is the difference between the kinetic energy (T) and potential energy (U) of a system.

$$L = T - U \qquad (4\text{-}11)$$

This sub-section will be divided into three smaller sections. The first section will derive the kinetic energy for the system. The next section will derive the potential energy for the system. The final section will combine all the results and derive the equations of motion for the system.

4.2.1 Kinetic Energy

The kinetic energy of a rotating rigid body is given by the following equation:

$$T = \frac{1}{2}\bar{\omega}^T I \bar{\omega} \qquad (4\text{-}12)$$

The total kinetic energy of the system can be expressed as the superposition of the kinetic energy of the outer frame and the kinetic energy of the inner mirror body frame. Expressions for the angular velocity of the outer frame and the inner frame must be derived before the analysis proceeds.

The angular velocity of the outer frame is straightforward to calculate. The outer frame is constrained to rotations about the inertial frame **Z**-axis, or θ rotations. Recall that $\bar{\omega} = \bar{\mathbf{v}} \times \bar{\mathbf{r}}$, where $\bar{\mathbf{v}}$ is the tangential velocity of the rotating body and $\bar{\mathbf{r}}$ is the position

vector of any point on the rotating body. Therefore, the tangential velocity will be in the X-Y plane. The angular velocity vector due to θ rotation lies entirely in the $\hat{U}_z$ direction.

$$\omega_{frame,inertial} = \begin{bmatrix} 0 \\ 0 \\ \dot{\theta} \end{bmatrix} \qquad (4\text{-}13)$$

The kinetic energy for the outer frame can now be written:

$$\begin{aligned}
\mathbf{T}_{frame} &= \frac{1}{2} \vec{\omega}^{\mathbf{T}}_{frmae,inertial} \mathbf{I}_{frame} \vec{\omega}_{frame,inertial} \\
&= \frac{1}{2} \begin{bmatrix} 0 & 0 & \dot{\theta} \end{bmatrix} \begin{bmatrix} \mathbf{I}_{frame1} & 0 & 0 \\ 0 & \mathbf{I}_{frame2} & 0 \\ 0 & 0 & \mathbf{I}_{frame3} \end{bmatrix} \begin{bmatrix} 0 \\ 0 \\ \dot{\theta} \end{bmatrix} \\
&= \frac{1}{2} \mathbf{I}_{frame3} \dot{\theta}^2
\end{aligned} \qquad (4\text{-}14)$$

The next step is to determine the kinetic energy of the inner frame. This calculation is more complicated than the outer frame because the inner frame has two degrees of rotation. It can rotate through θ and φ. The angular velocity due to the φ rotation is easily described in the moving coordinate frame. The rotation is about the y-axis and the velocity component is entirely in the $\hat{U}_y$ direction.

$$\vec{\omega}_{inner,body} = \begin{bmatrix} 0 \\ \dot{\varphi} \\ 0 \end{bmatrix} \qquad (4\text{-}15)$$

The θ component for the inner body rotations comes from the fact that the inner frame is attached to the outer frame. Therefore, the inner frame angular velocity has an additional

50

component identical to the outer frame angular velocity. Before adding the two velocity components, both components must be expressed in terms of the same reference frame. The φ rotations are in the body frame and the θ rotations are in the inertial frame. Using a little foresight, it is computationally easier to represent the inner body angular velocity in the body frame. This will become apparent in the kinetic energy calculation. Equation 4-16 is the angular velocity of the inner frame in the body coordinate frame.

$$\bar{\omega}_{\text{inner,body}} = \begin{bmatrix} 0 \\ \dot{\varphi} \\ 0 \end{bmatrix} + \Lambda_{\varphi\theta} \begin{bmatrix} 0 \\ 0 \\ \dot{\theta} \end{bmatrix}$$

$$= \begin{bmatrix} -\dot{\theta}\sin\varphi \\ \dot{\varphi} \\ \dot{\theta}\cos\varphi \end{bmatrix} \tag{4-16}$$

Now, the kinetic energy for the inner frame can be calculated. Here is where the choice of coordinate frame makes a computational difference. In the body frame, the coordinate frame is attached to the mirror body. The inertia tensor for the body frame is a diagonal matrix. However, in the inertial frame, the inertia tensor contains product of inertia terms and increases the complexity of the calculation. Both tensors are shown below.

$$I_{\text{inner,body}} = \begin{bmatrix} I_1 & 0 & 0 \\ 0 & I_2 & 0 \\ 0 & 0 & I_3 \end{bmatrix}$$

$$I_{\text{inner,inertial}} = \Lambda_{\varphi\theta} I_{\text{inner,body}} \Lambda_{\varphi\theta}^T = \begin{bmatrix} I_{XX} & I_{XY} & I_{XZ} \\ I_{YX} & I_{YY} & I_{YZ} \\ I_{ZX} & I_{ZY} & I_{ZZ} \end{bmatrix}$$

51

$$I_{XX} = (I_1\cos^2\theta + I_2\sin^2\theta)\cos^2\varphi + I_3\sin^2\varphi$$

$$I_{XY} = I_{YX} = (I_1 - I_2)\cos\varphi\cos\theta\sin\varphi$$

$$I_{XZ} = I_{ZX} = (I_1\cos^2\theta + I_2\sin^2\theta - I_3)\cos\varphi\sin\varphi$$

$$I_{YY} = I_1\sin^2\theta + I_2\cos^2\theta$$

$$I_{YZ} = I_{ZY} = (I_1 - I_2)\sin\theta\sin\varphi\cos\theta$$

$$I_{ZZ} = (I_1\cos^2\theta + I_2\sin^2\theta)\sin^2\varphi + I_3\cos^2\varphi$$

Clearly, a diagonal matrix is much easier to work with than the other matrix. The kinetic energy of the inner frame is now a straightforward calculation.

$$\mathbf{T}_{inner} = \frac{1}{2}\vec{\omega}^T_{inner,body}\mathbf{I}_{inner,body}\vec{\omega}_{inner,body}$$

$$= \frac{1}{2}\begin{bmatrix} -\dot{\theta}\sin\varphi & \dot{\varphi} & \dot{\theta}\cos\varphi \end{bmatrix}\begin{bmatrix} I_1 & 0 & 0 \\ 0 & I_2 & 0 \\ 0 & 0 & I_3 \end{bmatrix}\begin{bmatrix} -\dot{\theta}\sin\varphi \\ \dot{\varphi} \\ \dot{\theta}\cos\varphi \end{bmatrix} \quad (4\text{-}17)$$

$$= \frac{1}{2}\dot{\theta}^2(I_1\sin^2\varphi + I_3\cos^2\varphi) + I_2\dot{\varphi}^2$$

The last step in determining the kinetic energy of the entire system is to add the kinetic energy of the outer frame and the inner frame. At first glance it may appear incorrect to add the kinetic energy of the outer frame which was calculated using inertial frame vectors and the kinetic energy of the inner frame which was calculated using body frame vectors. This is allowable because kinetic energy is a scalar quantity. The kinetic energy of a system is independent of the reference frame it is calculated in. Equation 4-18 is the kinetic energy for the entire system.

$$T = T_{frame} + T_{inner}$$

$$= \frac{1}{2}\left(\dot{\theta}^2(I_{frame3} + I_1\sin^2\varphi + I_3\cos^2\varphi) + I_2\dot{\varphi}^2\right) \quad (4\text{-}18)$$

4.2.2 Potential Energy

The potential energy of the mirror system is contained entirely in the flexure beams that connect the outer frame to the inner mirror body. The flexures act like springs. The potential energy of a spring is a function of the axial, torsional, and bending deformations of the spring. In the case of the mirror system, only torsional deformation is considered. The general form for the potential energy of a spring due to torsional deformation is given in equation 4-19.

$$U = \frac{1}{2}k\varphi^2 \tag{4-19}$$

In the equation, φ is the angular deflection of the spring, and k is the torsional spring constant of the flexures. k is a function of the material and dimensions of the flexure. The flexures are made of silicon material and have dimensions $txlxw$ (thickness x length x width).

$$k = \frac{Gt^3w}{16l}\left[\frac{16}{3} - 3.36\frac{t}{w}\left(1 - \frac{t^4}{12w^4}\right)\right] \tag{4-20}$$

G is the modulus of rigidity of silicon. It is calculated from the Poisson ratio of silicon (v) and Young's modulus of silicon (E) (values that are both looked up).

$$G = \frac{E}{2(1-v)} \tag{4-21}$$

The flexures are only deformed by rotations of the inner mirror body. Therefore, it is only a function of the angular position φ. It is also worth noting that the kinetic energy due to the angular rotation of the flexure is negligible relative to the kinetic energy of the

outer frame and inner frame. The moment of inertia of the flexure is significantly smaller than the rest of the system and can be ignored.

4.2.3 Equations of Motion

The kinetic energy and potential energy of the system is now completely determined. To calculate the equations of motion for the rotating mirror, we need to solve the Euler-Lagrange Equations.

$$\frac{d}{dt}\frac{\partial L}{\partial \dot{\xi}} - \frac{\partial L}{\partial \xi} = \sum_i \Xi_i \qquad (4\text{-}22)$$

The right side of equation 4-22 represents all generalized forces applied to the system. These forces include damping forces inherent in the system and drive forces from external actuators.

To begin, the partial derivatives with respect to ξ and $\dot{\xi}$ must be calculated.

$$\frac{\partial L}{\partial \theta} = 0 \qquad (4\text{-}23)$$

$$\frac{\partial L}{\partial \dot{\theta}} = \dot{\theta}(I_{frame3} + I_1\sin^2\varphi + I_3\cos^2\varphi) \qquad (4\text{-}24)$$

$$\frac{\partial L}{\partial \varphi} = \dot{\theta}^2(I_1 - I_3)\sin\varphi\cos\varphi - k\varphi \qquad (4\text{-}25)$$

$$\frac{\partial L}{\partial \dot{\varphi}} = I_2\dot{\varphi} \qquad (4\text{-}26)$$

54

The final step before piecing everything together is to calculate the time derivative portion of the equation.

$$\frac{d}{dt}\frac{\partial L}{\partial \dot{\theta}} = \ddot{\theta}\left(I_{frame\,3} + I_1\sin^2\varphi + I_3\cos^2\varphi\right) + 2\,\dot{\varphi}\dot{\theta}(I_1 - I_3)\sin\varphi\cos\varphi \quad (4\text{-}27)$$

$$\frac{d}{dt}\frac{\partial L}{\partial \dot{\varphi}} = I_2\ddot{\varphi} \quad (4\text{-}28)$$

Finally, equations 4-23 through 4-28 can be combined to yield the equations of motion for the 2-axis mirror system.

$$\ddot{\theta}\left(I_{frame\,3} + I_1\sin^2\varphi + I_3\cos^2\varphi\right) + 2\,\dot{\varphi}\dot{\theta}(I_1 - I_3)\sin\varphi\cos\varphi = \sum_i \Xi_i \quad (4\text{-}29)$$

$$I_2\ddot{\varphi} + \dot{\theta}^2(I_3 - I_1)\sin\varphi\cos\varphi + k\varphi = \sum_j \Xi_j \quad (4\text{-}30)$$

In a force-free system, the right-hand side of equations 4-29 and 4-30 equals 0. However, in the real world, such force-free systems do not exist. The most common external forces prevalent in any real world system are damping forces. Damping forces act to oppose the motion of a body. For most mechanical systems, the damping force is proportional to the velocity of the body.

In this system, there are two forms of damping present. The inner-axis resonates at a high enough frequency that air viscosity will affect its motion. The outer-axis is attached to a bearing system. The bearings are not frictionless and also oppose the motion of the outer axis. Equations 4-31 and 4-32 show the equations of motion with the damping terms added. The coefficient of damping due to air viscosity will be denoted by the symbol B_{air}. The coefficient of damping due to the bearing system will be denoted by the symbol B_{bb}.

$$\ddot{\theta}\left(I_{frame3} + I_1 \sin^2 \varphi + I_3 \cos^2 \varphi\right) + 2\dot{\varphi}\dot{\theta}(I_1 - I_3)\sin\varphi\cos\varphi = \sum_i \Xi_i - B_{bb}\dot{\theta} \quad (4\text{-}31)$$

$$I_2\ddot{\varphi} + \dot{\theta}^2(I_3 - I_1)\sin\varphi\cos\varphi + k\varphi = \sum_j \Xi_j - B_{air}\dot{\varphi} \quad (4\text{-}32)$$

The above equations show the non-linear coupled behavior of the system. This complicated description makes the design of a control system very difficult. Therefore, it would be useful to decouple and linearize the above equations. An important fact that will allow the system to be decoupled is the difference in the rotational speeds of the inner and outer axis. Recall that the inner axis will rotate on the order of hundreds of hertz, while the outer axis will only rotate at 2 Hz. Furthermore, the inner axis rotations have a small enough amplitude to use small angle approximations. Using the method of multiple scales, the above system is decoupled into the following pair of equations. The detailed analysis of the method of multiple scales is presented in Appendix D.

$$I_{frame3}\ddot{\theta} + B_{bb}\dot{\theta} = \sum_i \Xi_i \quad (4\text{-}33)$$

$$I_2\ddot{\varphi} + B_{\varphi}\dot{\varphi} + k\varphi = \sum_j \Xi_j \quad (4\text{-}34)$$

The decoupled, linear pair of equations will allow control systems to be designed for each axis independent of each other.

Chapter 5

Outer Axis Control

A DC motor is used to drive the outer-axis of the MEMS system. The system specifications require that the outer-axis rotate at a constant speed of 2Hz. To accomplish this a motor speed-controller must be designed.

There are numerous options available in designing a speed-controller. The LIDAR system already has a 2-axis position sensor that could be used to close a feedback loop around the motor. However, designing a speed-controller with the mirror position as the feedback element and motor input voltage (or current) as the command signal is non-trivial and not the most elegant way to approach the problem. The size of the system also places constraints on the types of sensors that might be added to close the feedback loop. Therefore, a feedback scheme using the back emf of the motor was used to control the speed. This chapter will present a workable model of a DC motor, followed by the controller design and implementation.

5.1 DC Motor Model

A simple model for a permanent magnet DC motor is given in figure 5-1. The applied voltage, v_a, is the input that drives the motor. The output of the system is the angular

velocity, ω(t), of the motor shaft. The resistor and inductor in the model come from the armature winding in the motor. These values vary with each motor and can be obtained experimentally. As the motor rotor rotates in the magnetic field of the permanent magnet it will generate a current through the armature windings. This current will act to oppose the affects of the input current, i_a. This phenomenon is a direct consequence of Faraday's Law of Induction. The opposing current will create a voltage at the terminals of the motor. This voltage is called the back electromotive force, or back emf, and will be denoted as v_{bemf}. The back emf is proportional to the speed of the motor shaft. The relationship is given in equation 5-1.

$$v_{bemf} = K_b \omega \qquad (5\text{-}1)$$
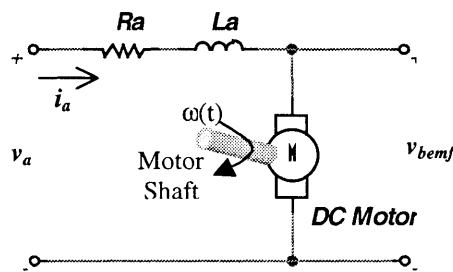
Figure 5-1: Permanent Magnet DC Motor Model

The motor torque is proportional to the input current. The relationship is shown in equation 5-2.

$$\tau_m = K_m i_a \qquad (5\text{-}2)$$

The constants K_b and K_m also are functions of the motor parameters and can be obtained experimentally. Conservation of energy requires that the electrical power into the motor must equal the mechanical output power (in a friction-free motor). Therefore, K_b and K_m must be equal.

Using the above model, a state-space representation of the system can be created. The states used in the state-space model are the current through the motor (i_a) and the back emf voltage (v_{bemf}). Using Kirchoff's Voltage Law, the first state equation can be written.

$$v_a = R_a i_a + L_a \frac{di_a}{dt} + v_{bemf} \tag{5-3}$$

The next state equation is determined from Newton's equations of motion for the motor shaft. The motor shaft is rigidly connected to a cam. The moment of inertia of the motor shaft and the cam can be calculated and will be denoted by **J**.

$$J\dot{\omega} = \tau_m - K_f \omega - \tau_D \tag{5-4}$$

Here, K_f is a linear coefficient of friction, and τ_D is any disturbance torque that acts on the cam and motor shaft. Substituting equations 5-1 and 5-2 into equations 5-3 and 5-4, and re-writing the equations in a vector/matrix notation, the state-space model can be written. The output of the state-space model will be defined as the angular velocity of the motor shaft.

$$\frac{d}{dt}\begin{bmatrix} i_a \\ v_{bemf} \end{bmatrix} = \begin{bmatrix} -\dfrac{R_a}{L_a} & -\dfrac{1}{L_a} \\ \dfrac{K_m K_b}{J} & -\dfrac{K_f}{J} \end{bmatrix}\begin{bmatrix} i_a \\ v_{bemf} \end{bmatrix} + \begin{bmatrix} \dfrac{1}{L_a} & 0 \\ 0 & -\dfrac{1}{J} \end{bmatrix}\begin{bmatrix} v_c \\ \tau_D \end{bmatrix}$$

$$\omega = \begin{bmatrix} 0 & \dfrac{1}{K_b} \end{bmatrix}\begin{bmatrix} i_a \\ v_{bemf} \end{bmatrix} \tag{5-5}$$

The above state-space model is a multi-input/single-output system. The system can be expressed compactly using a block diagram.

Motor Dynamics
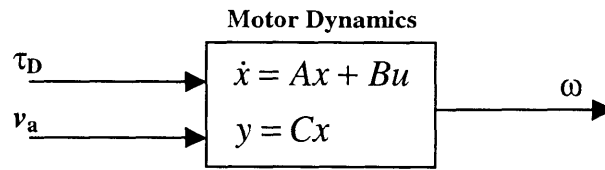
Figure 5-2: Block diagram representation of state-space model

Using equations 5-1 and 5-2, and input-output map from applied voltage to motor speed can be determined. The above description and state-space model can be translated directly to a block diagram.
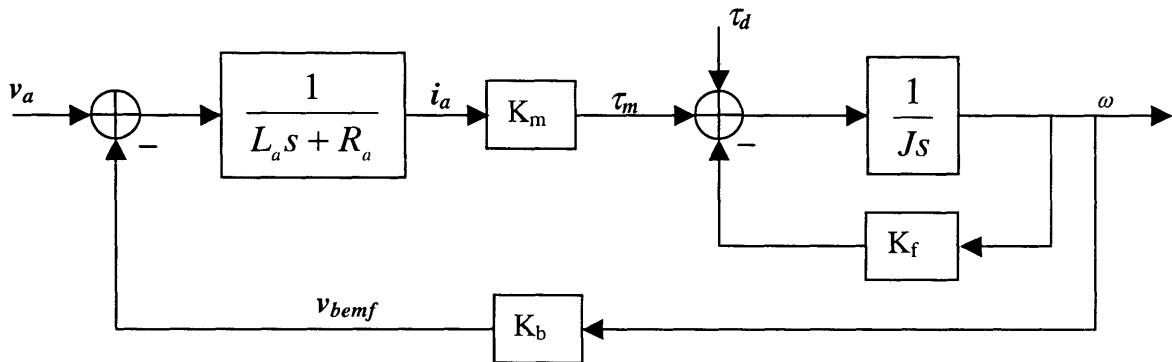
Figure 5-3: Revised block diagram of the DC motor

The transfer function from input voltage to motor speed is given in equation 5-6.

$$\frac{\omega}{v_a} = \frac{K_m}{\left(L_a + J\right)s^2 + \left(L_a K_f + R_a J\right)s + \left(R_a K_f + K_m K_b\right)} \tag{5-6}$$

5.2 Controller Design and Implementation

With the above model in place, the controller can now be designed. The basic scheme for the closed-loop system is simple. As the motor shaft speed slows down, the control input

to the motor must increase to speed up the shaft. Likewise, if the motor shaft begins rotating too quickly, the control input must decrease to slow down the motor shaft. This control law is easily implemented with an output-feedback scheme. Figure 5-4 shows the block diagram of the closed loop system. The single block labeled M(s) represents the motor dynamics described in equation 5-6.
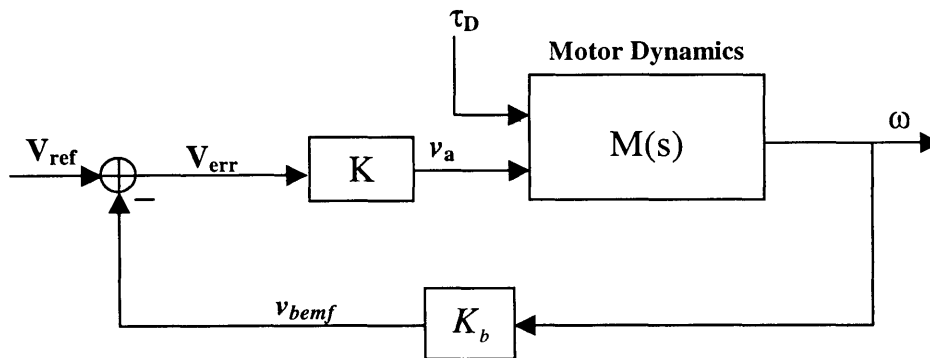
Figure 5-4: Block Diagram of closed-loop system

The implementation of the above feedback scheme is not as trivial as the figure suggests. The main problem is that there is no sensor available to measure the speed of the motor shaft. The controller must use the physical nature of the motor to generate a feedback signal that is proportional to the speed. The physical model of the motor developed earlier can help develop the necessary implementation.

Figure 5-5 shows a simple circuit that will help build intuition on how the motor can generate a voltage proportional to the motor shaft speed. The circuit shown creates a voltage divider between the applied voltage, v_{app}, and ground. The voltage applied at the motor terminals is given by the following equation:

$$V_m = \frac{R_a + L_a s}{R + R_a + L_a s} V_{app}$$

(5-7)

However, equation 5-7 does not paint the entire picture. As the speed of the motor increases, the back emf will also increase creating a smaller potential difference between

61

v_m and v_{bemf}, ultimately reducing the current through the motor. Furthermore, the current that flows through the motor must also flow through the series resistor. Equation 5-8 defines the current i_m through the motor, and equation 5-9 gives the true description v_m.

$$i_m = \frac{1}{R + R_a + L_a s}\left(V_{app} - V_{bemf}\right) = \frac{1}{R_a + L_a s}\left(V_m - V_{bemf}\right) \tag{5-8}$$

$$V_m = \frac{R_a + L_a s}{R + R_a + L_a s}V_{app} + \frac{R}{R + R_a + L_a s}V_{bemf} \tag{5-9}$$
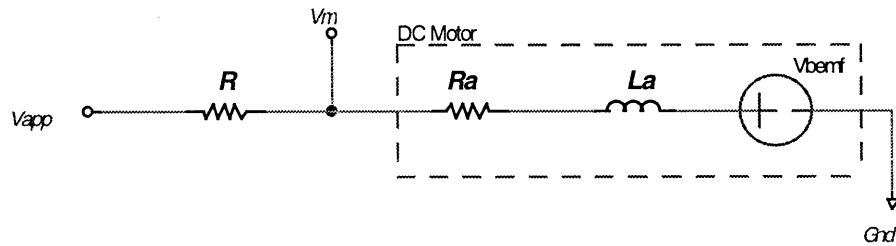
Figure 5-5: DC Motor with a series resistance

Combining equation 5-9 with equation 5-1 results in an equation relating the motor voltage to motor speed.

$$V_m = \frac{R_a + L_a s}{R + R_a + L_a s}V_{app} + \frac{R}{R + R_a + L_a s}K_b \omega \tag{5-10}$$

This voltage can now be fed back to a differential amplifier that subtracts v_m from a reference voltage. Appropriate gains can be added to complete the circuit. Figure 5-6 shows the circuit implementation of the described feedback scheme.
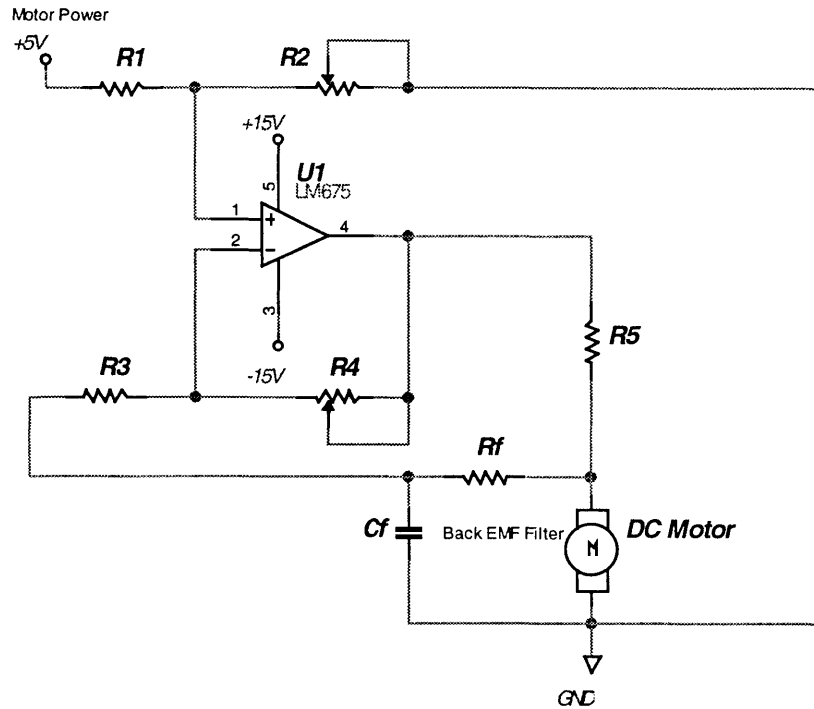
Figure 5-6: Circuit schematic for closed loop speed control of a DC motor

Note that in the schematic an RC-filter was added in parallel to the motor. The voltage across the terminals of the motor has two components: the DC component (which is what is important to the feedback loop) and a noise component due to noise in the motor commutation. The filter acts to remove the effects of the noise. However, it also introduces more impedance to the example shown in figure 5-5. Figure 5-7 shows an updated version of figure 5-5 with the RC-circuit in place. The voltage that is fed back to the differential amplifier is the output of the RC-filter.
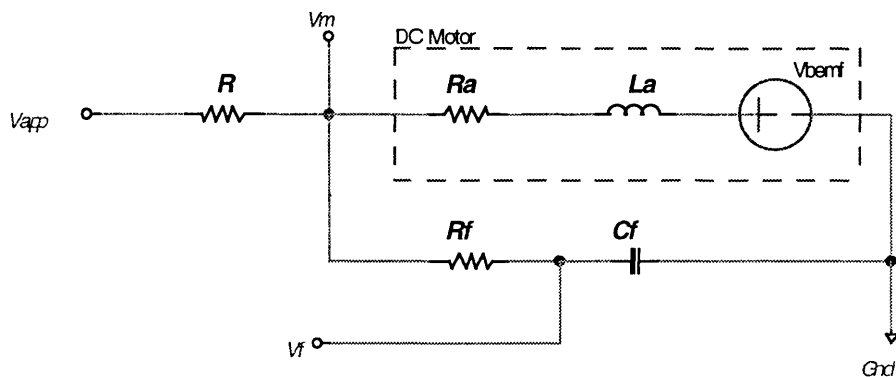
Figure 5-7: DC motor with RC-filter

The voltage v_m and v_f are given in equations 5-11 and 5-12 respectively. To make the notation more compact, the impedance of the motor will be labeled Z_m and the impedance of the filter will be labeled Z_f.

$$V_m = \frac{Z_f Z_m}{Z_f Z_m + R(Z_f + Z_m)} V_{app} + \frac{RZ_f}{Z_f Z_m + R(Z_f + Z_m)} V_{bemf} \qquad (5\text{-}11)$$

$$V_f = \frac{1}{R_f C_f s + 1} V_m \qquad (5\text{-}12)$$

As mentioned earlier, the manufacturer predetermines the impedance of the motor. The value of the filter impedance must be chosen to satisfy two requirements. The time constant of the filter must be faster than the speed that the motor will be running at, and the impedance of the filter must be large enough so as not to compete with the motor for current. Therefore, it is a good choice for $R_f \approx 10 * Z_m(2\text{Hz})$ and $R_f C_f << (1/2\pi f)$.

The potentiometer R2 in figure 5-6 allows easy adjustment of the input reference voltage. The potentiometer R4 adjusts the gain of the error voltage (the difference between the reference voltage and the feedback voltage). A power op-amp was chosen in order to supply enough current to the motor. Table 5-1 summarizes all the component values used in figure 5-6.

R1, R3	10 kΩ
R2, R4	100 kΩ (pot)
R5	51 Ω
Rf	150 Ω
Cf	220 μF

Table 5-1: Summary of component values for speed controller

Using the above circuit, a block diagram of the control system is developed below.
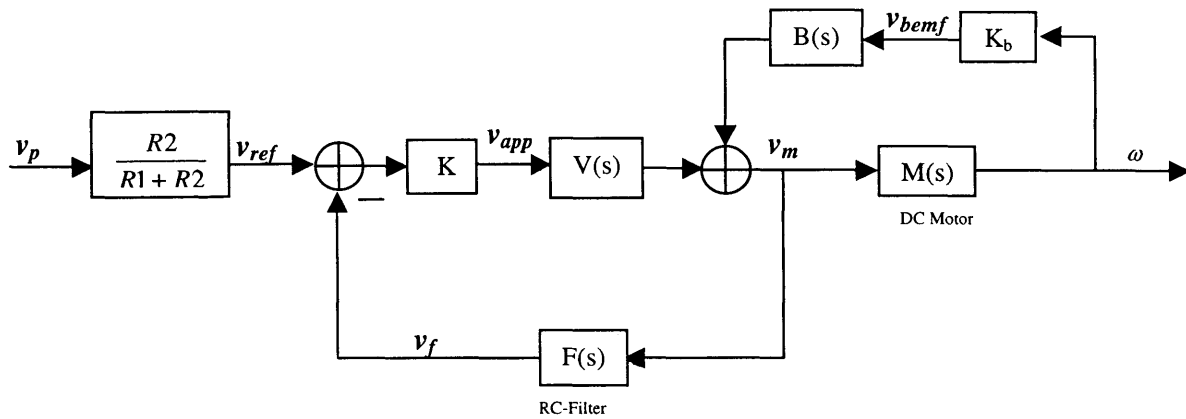
Figure 5-8: Block Diagram of DC Motor Speed Control with back emf feedback

In the above figure, V(s) and B(s) come from equation 5-11. The gain block is set through the potentiometer R4. It should also be noted that the applied voltage will move around the offset of the differential amplifier, set by v_{ref}. Using figure 5-8, the transfer function relating the input voltage v_{ref} to the output motor speed can be calculated.

$$\frac{\omega}{v_{ref}} = \frac{KVM}{1 - K_b BM + KFV} \tag{5-13}$$

Chapter 6

Inner-Axis Control

The inner-axis of the system consists of a permanent magnet embedded inside a MEMS mirror structure connected to torsion springs. The mirror assembly is positioned inside the gap of an electromagnet, which is used to actuate the system. The system specifications require that the inner-axis resonate at a desired frequency while maintaining a fixed scan amplitude. The controller must also stabilize the closed loop system.

The design of the controller is dependent on the dynamics of the system. A descriptive model of the system was developed using modeling techniques and system identification techniques from open-loop measurements. In this chapter, the dynamic model of the system will be presented. A description of the open-loop measurements along with the data collected will then be presented and compared to the dynamic model developed earlier. The proposed control scheme will then be presented, with appropriate analysis.

6.1 Dynamic Model of the Inner-Axis

The analysis of this system involves understanding the dynamics of an electro-magnet, a spring-mass system, and electro-mechanical coupling. Rather than study each element individually, the analysis can become much easier if the problem is mapped to one that is well understood.

When a voltage is applied across the terminals of the electro-magnet, the impedance of the electro-magnet causes a current, i_{mag}, to flow through the coils. This generates a magnetic field that flows through the core and the air gap. The magnetic field strength is proportional to the number of turns of wire (N_{mag}), the magnitude of the current, and the gap width (L). A first-order approximation of the field strength is given in equation 6-1. This approximation ignores fringe effects in the gap, and also assumes that there are no losses due to flux leakage in the core.

$$B_{mag} = \frac{\mu_o N_{mag} i_{mag}}{L} \tag{6-1}$$

Sitting in the gap of the electro-magnet is the mirror assembly with the permanent magnet. The magnetic field produced by the permanent magnet is initially perpendicular to the magnetic field generated by the electro-magnet. This produces a torque on the permanent magnet, which in turn causes the mirror assembly to rotate about the flexure axis. A first-order approximation of the torque is given in equation 6-2. In the equation, M_{mag} is the magnetization vector of the permanent magnet, and φ is the angle formed between the electromagnetic field vector and the magnetization vector.

$$\tau_{mag} = B_{mag} M_{mag} \cos(\varphi) \tag{6-2}$$

The flexures act as a restoring force causing the assembly to oscillate. Furthermore, as the mirror rotates, the direction of the magnetic field of the permanent magnet changes, and points more towards the core. This creates a back emf current through the coils of the electromagnet.

The above simple description of the system is very similar, if not identical, to the operation of a DC motor. The only difference is that a motor typically does not have a restoring force on the rotor. With this in mind, a block diagram describing the above system can be drawn by using the same structure as the block diagram used in the motor

model derived in Chapter 5. From the block diagram, all transfer functions of interest can be readily calculated. As with the motor, the constant K is a function of the electromagnet and permanent magnet properties.
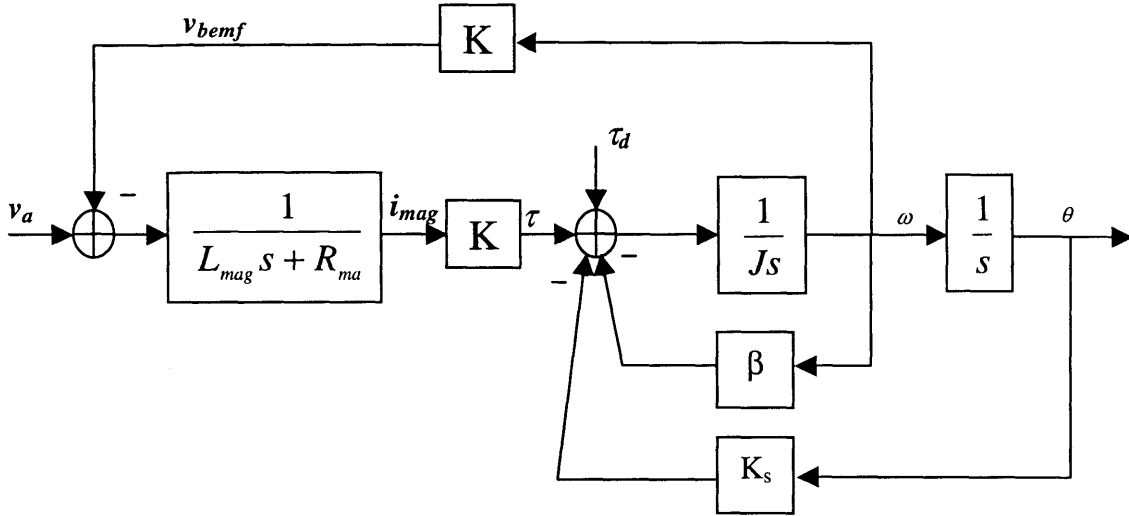
Figure 6-1: Block Diagram of Inner-axis system

$$\frac{\theta}{v_a} = \frac{K}{(JL_{mag})s^3 + (JR_{mag} + BL_{mag})s^2 + (BR_{mag} + K_sL_{mag} + K^2)s + K_sR_{mag}} \qquad (6\text{-}3)$$

$$\frac{i_{mag}}{v_a} = \frac{Js^2 + Bs + K_s}{(JL_{mag})s^3 + (JR_{mag} + BL_{mag})s^2 + (BR_{mag} + K_sL_{mag} + K^2)s + K_sR_{mag}} \qquad (6\text{-}4)$$

The parameters of the system, such as the electromagnet impedance, the damping, and the spring constant were all obtained experimentally and will be presented in the next subsection.

6.2 Experimental System Identification

The experimental set-up used to determine the parameters of the system is shown in figure 6-2. The electro-magnet was driven with a function generator and a series resistance. A laser pointer was used as the light source to reflect off the mirror. The reflected beam was projected onto a white wall, and its amplitude was measured.
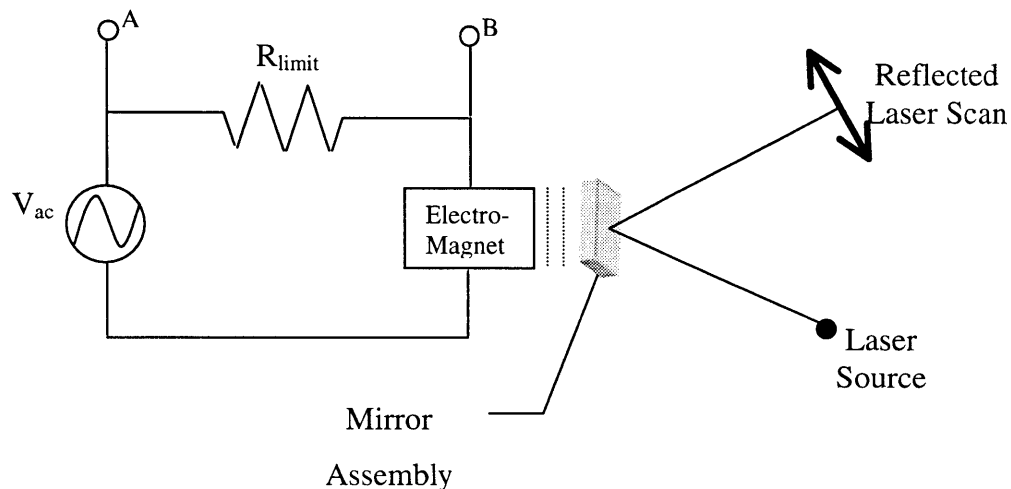
Figure 6-2: Experimental set-up for system identification

Using an oscilloscope, measurements were taken at nodes A and B as the input frequency was swept. For each frequency, the reflected scan width was also measured.

The resonant frequency of the system occurs when the amplitude of the laser scan reaches a maximum value. This frequency, however, is not the true resonant frequency, but the damped natural frequency of the system. In a lightly damped oscillator, as is the case with this system, the damped natural frequency and the true resonant frequency differ by a very small amount. The relationship is given below with ω_d representing the damped natural frequency, ω_n representing the resonant frequency, and ξ representing the damping ratio of the system.

$$\omega_d = \omega_n \sqrt{1 - \xi^2} \qquad \text{(6-5)}$$

$$\xi = \frac{B}{2\sqrt{JK_s}} \qquad \text{(6-6)}$$

The damping ratio can be determined by measuring the Quality factor of the system. The Quality factor is a measure of the "peakiness" of a resonant system. It is found by finding the frequency above and below resonance where the amplitude decreases to half the amplitude at resonance.

$$Q = \frac{\omega_d}{\left(\omega_{+half-max} - \omega_{-half-max}\right)} \qquad \text{(6-7)}$$

$$\xi = \frac{1}{2Q} \qquad \text{(6-8)}$$

The damping coefficient B and the spring constant K_s can be determined using equation 6-6 and the following equation relating the resonant frequency to the inertia and spring constant of the system.

$$\omega_n = \sqrt{\frac{K_s}{J}} \qquad \text{(6-9)}$$

The inertia of J of the mirror/magnet assembly is calculated in Appendix C. The calculated and measured values are presented below in table 6-1. It is important to note here that these measurements correspond to only one mirror/magnet assembly. Each mirror that is fabricated will have wide variations in their mechanical properties. For each assembly that is used, the same measurements must be made to ensure proper characterization of the system.

71

ω_d	1683.27 rad/sec
$\omega_{+half-max}$	1687.66 rad/sec
$\omega_{-half-max}$	1679.50 rad/sec
Q	206.28
ξ	2.42×10^{-3}
ω_n	1683.27 rad/sec
J	1.27×10^{-9} Kg-m^2
B	1.035×10^{-8} Kg-m^2/sec
K_s	3.60×10^{-3} Kg-m^2/sec^2

Table 6-1: Summary of measured and calculated system parameters

Figure 6-3 shows the measured frequency response of the system in a dB-log scale. The small spike found at the lower frequencies is not modeled. It is most likely another resonant mode and can be ignored.
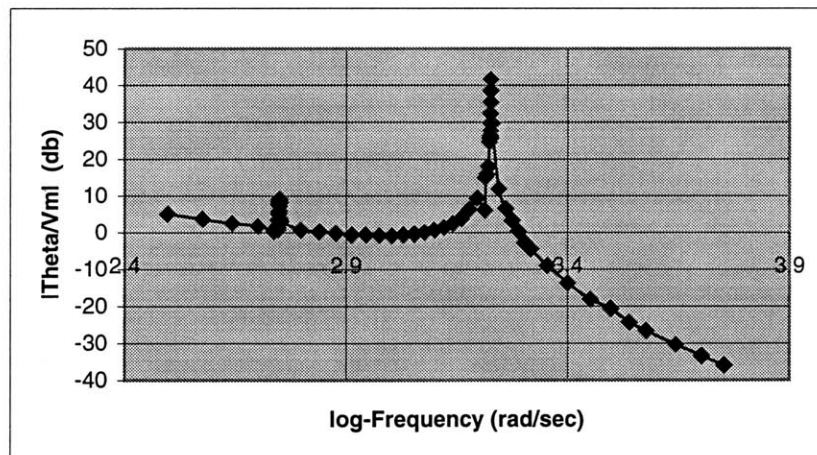
Figure 6-3: Measured frequency response of the inner-axis

The electromagnetic characteristics of the system were also measured using the above set-up. The potential drop across the limiting resistor was measured to calculate the

current flowing through the circuit. The impedance of the magnet as a function of frequency was calculated using the following relationship.

$$Z_{mag}(s) = \frac{V_B}{i} \qquad (6\text{-}10)$$

Figure 6-4 is a plot of $\dfrac{1}{Z_{mag}}(s)$. Notice that the plot almost looks like a first-order system except for the downward and upward spikes that occur in the vicinity of the mechanical resonant frequency of the system. This spike is a direct consequence of the induced back emf from permanent magnet, and is accurately described in equation 6-4.
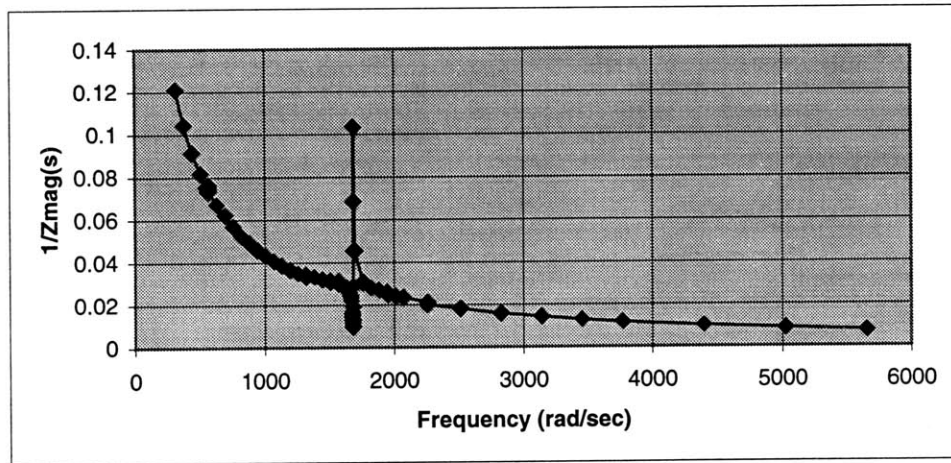
Figure 6-4: Impedance of the electromagnet as a function of frequency

The DC-resistance of the electromagnet was measured directly. The inductance was determined by finding the best-fit curve for the first-order portion of the data (ignoring the spikes). Using the values for the inductance and resistance, and using the values from table 6-1, the magnet constant K was determined by using equation 6-4 to produce a best-fit curve of the data. The results are presented in table 6-2. Figure 6-5 is a plot of equation 6-4 using all the calculated and measured parameters.

The measurements verified the model very accurately. This allows for the design of a model-based control, and is presented in the next section.

R_{mag}	3.26 Ω
L_{mag}	0.0235 H
K	0.0018 V-sec

Table 6-2: Summary of electromagnet measurements
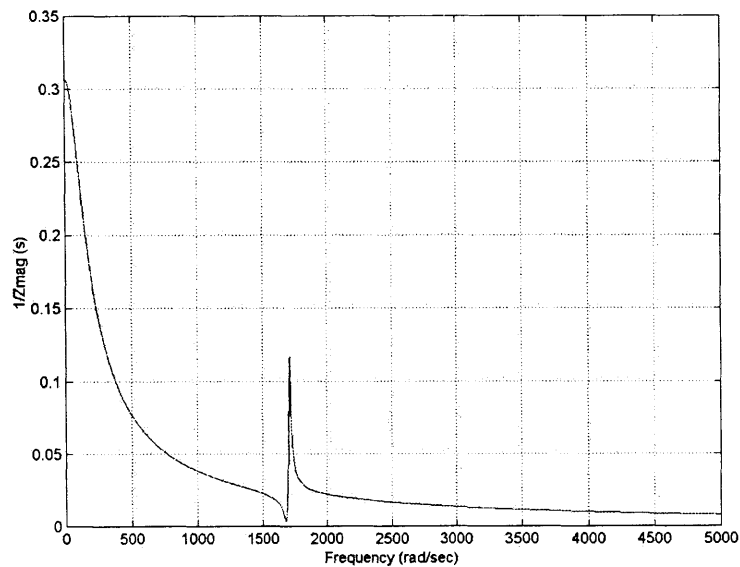
Figure 6-5: Impedance of electromagnet using the system model

6.3 Controller Design

The controller for the inner-axis has a few objectives. Any control that is used must ensure that the closed loop system remains stable. For this particular application, the controller must also maintain a fixed amplitude scan of the mirror. To minimize the power consumption of the system, it is desirable to drive the system near its resonant frequency. This corresponds to driving the system in the frequency band that has the

74

greatest gain. The main problem with this, and one of the reasons why amplitude control is necessary, is that small variations in the frequency of the drive signal, or variations in the dynamics of the physical plant* can result in a dramatic change in the amplitude due to the system's high Q-value.
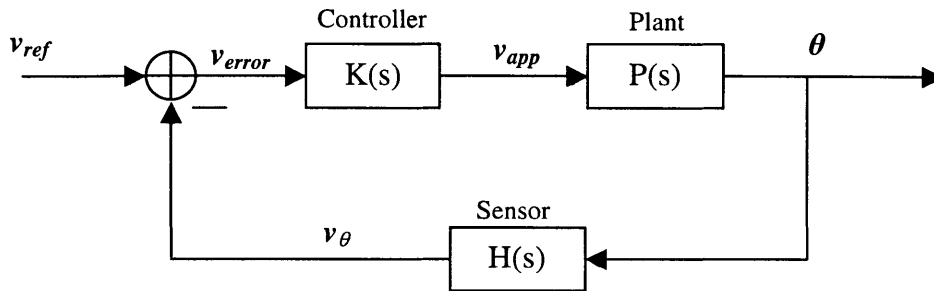
Figure 6-6: Block diagram of simplified closed loop control

Figure 6-6 shows a simplistic closed loop control scheme for the inner-axis control. The system input is a sinusoid with some predetermined frequency and amplitude corresponding to the desired scan amplitude of the system. The reference amplitude is compared to the actual amplitude of the system, as measured by the sensor. An error term is produced and the controller converts that signal into an applied command to the plant.

The first step in the control design is to determine the stability margins of the system. In order to gain some intuition on how the system might behave in a closed loop configuration, a root-locus plot of the configuration shown in figure 6-7 is given below. The root-locus assumes the controller is only a proportional gain. Also, recall from chapter 3 that the sensor has no significant frequency dependency, and for this analysis can be modeled as a unity gain sensor without loss of generality. The root-locus shows that as the gain is increased, the poles of the closed loop system will move into the right half of the s-plane, which will guarantee instability.

---

* Changes in temperature and fatigue in the system can cause the resonant frequency of the plant to drift over time.

Another useful measure of the stability of a closed loop system is to look at the phase margin of the open loop frequency response of the system. The open loop frequency response is defined in equation 6-11.

$$L(s) = K(s)P(s) \qquad (6\text{-}11)$$
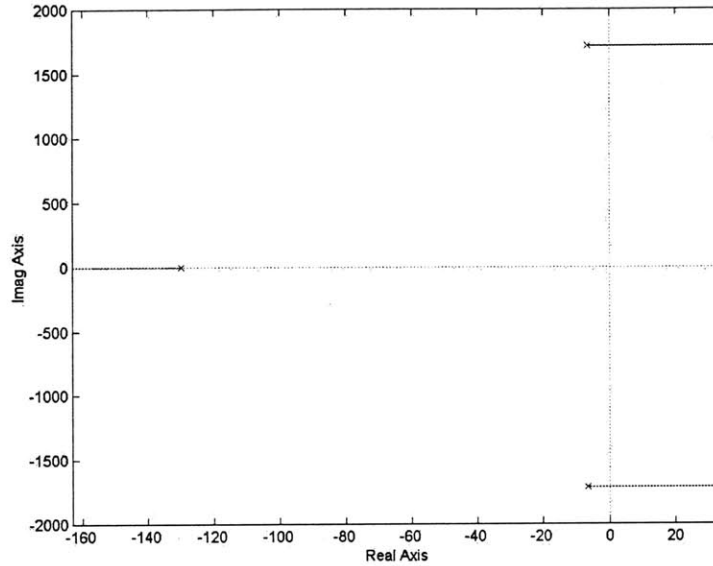
Figure 6-7: Root-locus of for proportional control of inner-axis

Instability occurs if the phase of the L(s) is greater or equal to -180° at the crossover frequency, the frequency where the magnitude is unity. The phase margin is the amount of negative phase shift that when added to the phase at the crossover frequency will produce instability. The example shown above has an infinite phase margin.

To ensure stability, the controller must provide additional phase to the loop transmission around the crossover frequency. A common way to add the necessary phase is by using a lead-compensator. A lead transfer function has the following form:

$$K_{lead}(s) = \frac{1}{\alpha} \frac{\alpha \tau s + 1}{\tau s + 1} \qquad (6\text{-}12)$$

76

Ideally, a pole would not be needed in a lead, but this causes problems with the implementation of the system. The zero is designed to add enough phase in the vicinity of the crossover frequency, and the pole must be placed so as to have a minimal impact on the response around the crossover frequency.

For this system, two cascaded lead compensators were used to generate enough phase margin. The lead network used is given in equation 6-13. Figure 6-8 shows a bode plot of the compensator, and figure 6-9 shows a bode plot of the loop transmission, L(s), with the stability margins labeled.

$$K_{lead}(s) = \frac{1}{10000}\left(\frac{s+1}{\frac{1}{5000}s+1}\right)^{2} \tag{6-13}$$
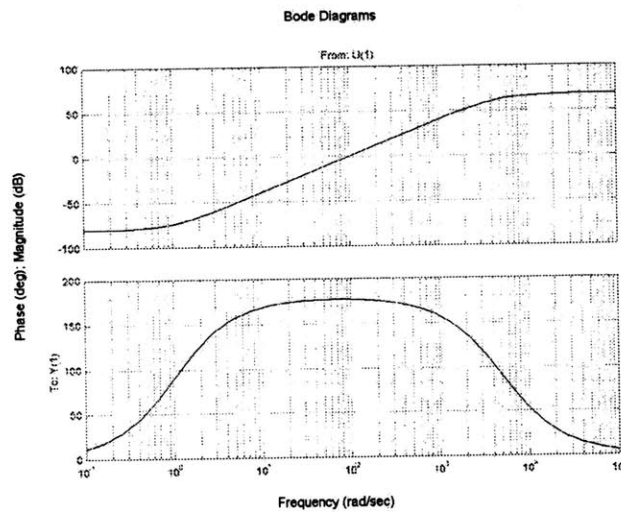
Figure 6-8: Bode plot of 2nd-Order lead compensator
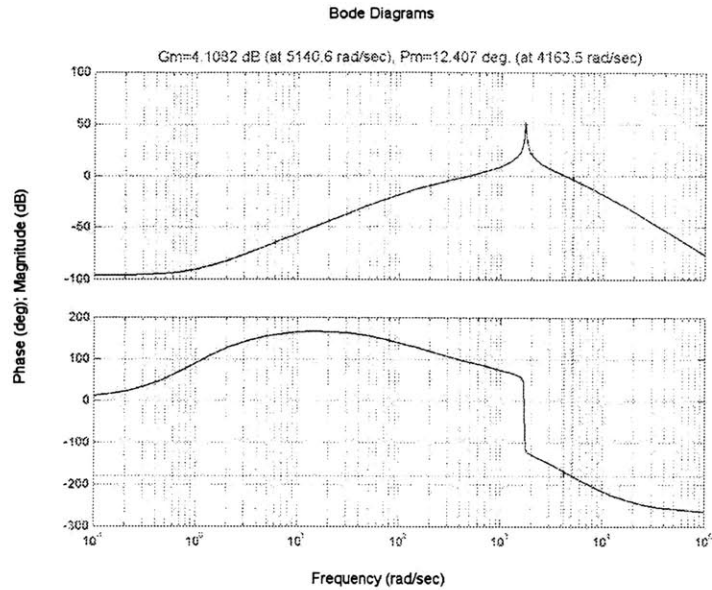
Figure 6-9: Bode plot of loop transmission with 2nd-Order lead compensation. Phase margin is 12.4°.

The phase margin can be improved by appropriately adjusting the gain of the compensator. The lead compensator improved the stability margins, but it greatly reduced the low frequency response of the system. For a system to track an input command well, it must have reasonably high gain at frequencies below the crossover frequency. An improvement of the low frequency gain of the loop transmission without disrupting the phase margin can be accomplished with the addition of a lag compensator. The general form for a lag compensator is given in equation 6-14.

$$K_{lag}(s) = \frac{\tau s + 1}{\alpha \tau s + 1} \qquad (6\text{-}14)$$

As with the lead design, MATLAB was used to determine a suitable lag compensator. The lag used is given in equation 6-15. The bode plot of the lag compensator is also shown in figure 6-10. The loop transmission bode plot with the lead and lag compensators is shown in figure 6-11.

78

$$K_{lag}(s) = 20 \frac{\frac{1}{1000}s + 1}{2s + 1} \qquad (6\text{-}15)$$
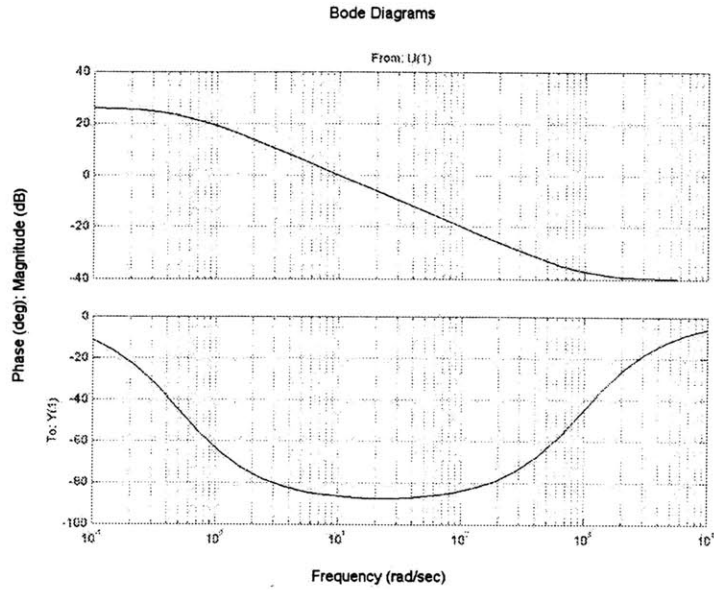
Figure 6-10: Bode plot of lag compensator
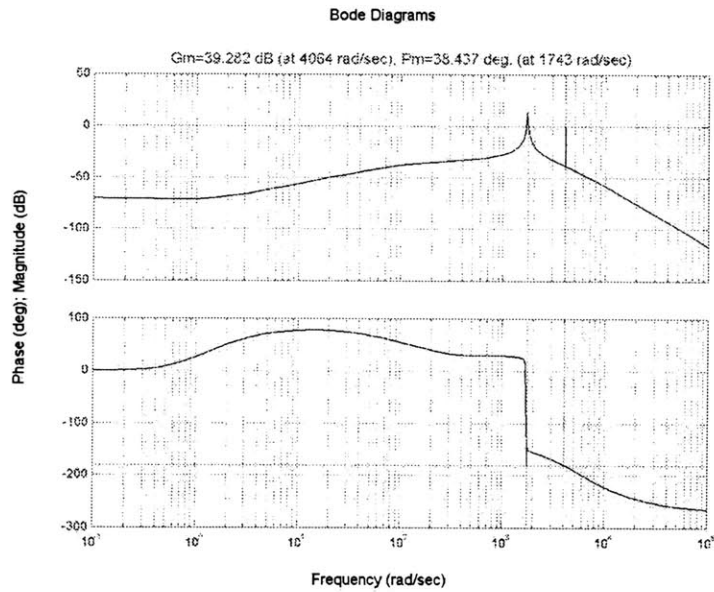
Figure 6-11: Bode plot of loop transmission with lead-lag compensator. Phase margin is 38.437°.

The lag compensator greatly improved the low frequency gain, and increased the overall phase margin of the system.

The above analysis shows that the compensator should successfully stabilize the closed loop system. The performance of the closed loop system is also greatly improved over the uncompensated system. Figure 6-12 shows the step response of the uncompensated plant in an open loop configuration, and the step response of the compensated closed loop system. Note that the compensated system brings the steady-state error to 0, and the peak response is much lower than the uncompensated system. Furthermore, the settling time is also greatly improved. As with the phase margin, the peak overshoot and settling time of the system can be adjusted by changing the gain of the compensator.

The lead-lag compensator chosen is only one possible control solution. There are many other compensators that could produce similar or even better results. However, implementation must also be considered when designing any compensator. The next section will discuss the implementation of the controller.
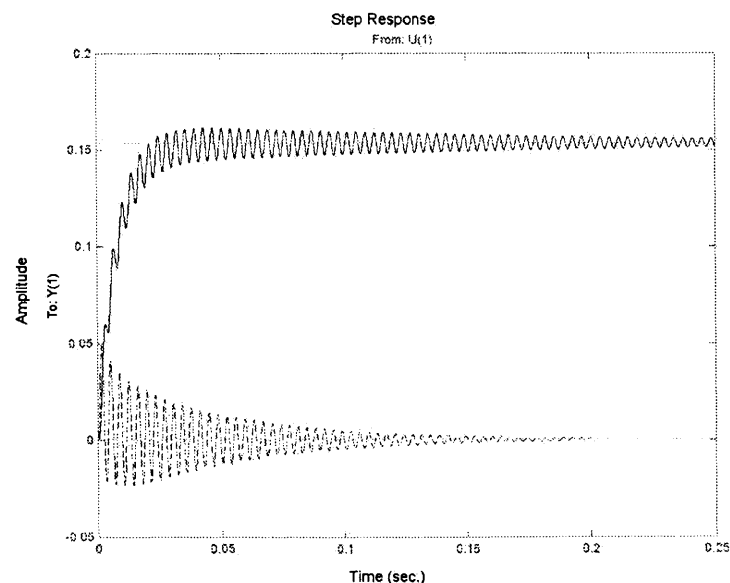
Figure 6-12: Step response of uncompensated system (solid line) and compensated closed loop system (dashed line)

6.4 System Implementation

The implementation of the closed system can be divided into specific stages. There is a signal generation stage that is responsible for generating a sinusoid with variable amplitude and frequency control. A voltage-controlled oscillator (VCO) is used to create the sinusoid. The next stage is the implementation of the compensator followed by a power stage that is necessary to provide enough current to drive the electromagnet. The sensor electronics comprises the next stage, and has already been described in chapter 3. Finally, there must be a stage that converts the sensor output into a DC value that can be compared to a reference voltage that determines the amplitude of the sinusoid. Figure 6-13 shows a block diagram of the implementation described above.
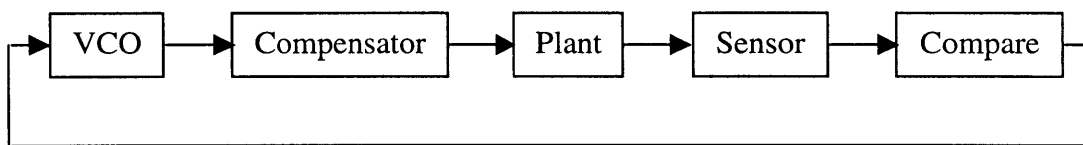
Figure 6-13: Block diagram of closed loop implementation

This section will detail each of the stages described above.

6.4.1 Voltage-Controlled Oscillator (VCO)

A monolithic function generator is a desirable choice because the amplitude and frequency of the output signals can be modulated with external voltages. The VCO used for this application is the XR-2206. The details of the XR-2206 can be found in the data sheet. This sub-section will present the configuration used for this application. Figure 6-14 shows the schematic of the XR-2206.

81

Figure 6-14: Schematic of VCO

The maximum amplitude of the output sine wave is proportional to the resistor R1 at pin 3. The amplitude is approximately 60mV (peak) for every kΩ at pin 3. A 2.2kΩ resistor was used to generate a maximum amplitude of ~132mV (peak). Resistors R7 and R8 create a voltage divider which can be used to adjust the DC bias of the output sinusoid. The frequency of operation is determined by the capacitor between pins 5 and 6, and the resistor R2 and R3. The potentiometer at R4 is used to modulate the frequency. The data sheet gives the following equation to pick the frequency. V_c is the output from the voltage divider formed by the potentiometer R4.

$$f = \frac{1}{R_2 C_1}\left(1 + \frac{R_2}{R_3}\left(1 - \frac{V_c}{3}\right)\right) \tag{6-16}$$

However, this equation did not seem to correspond to the actual operation. The values chosen produced the desired frequency range. The potentiometer R5 and R6 are used to adjust the harmonic distortion and symmetry of the output sine wave. The voltage level at pin 1 should be between 0 and 4 volts. A mechanical switch was placed at pin 1 to

toggle between open loop and closed loop operation. While in open loop, the voltage applied at pin 1 is adjusted with the potentiometer, R9. Table 6-3 summarizes all the resistor and capacitor values.

R1	2.2 kΩ
R2	16 kΩ
R3	82 kΩ
R4	100 kΩ (pot)
R5, R7, R9	25 kΩ (pot)
R6	200 Ω
R8	56 kΩ
C1	0.047 μF
C2, C3	1μF

Table 6-3: Component values for VCO

6.4.2 Compensator and Power Stage

The compensator designed earlier can be implemented using two operational amplifiers. The power output stage is a power amplifier that is able to supply enough current to drive the electromagnet. The schematic of the compensator is shown in figure 6-15.

83
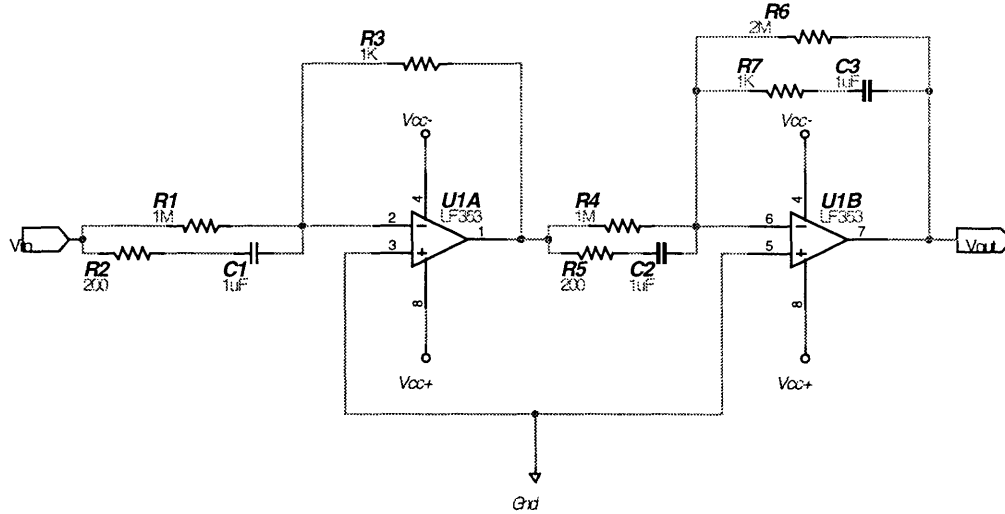
Figure 6-15: Compensator schematic

The transfer function of this implementation is given below.

$$\frac{V_{out}}{V_{in}} = \left(\frac{R_3 R_6}{R_1 R_4}\right)\left(\frac{((R_1 + R_2)C_1 s + 1)((R_4 + R_5)C_2 s + 1)(R_7 C_3 s + 1)}{(R_2 C_1 s + 1)(R_5 C_2 s + 1)((R_6 + R_7)C_3 s + 1)}\right) \quad (6\text{-}17)$$

The compensator transfer function described in section 6-3 cannot be implemented exactly due to limitations in resistor values and their accuracies. The values chosen approximate the desired response and are given below in table 6-4.

R1, R4	1 MΩ
R2, R5	200 Ω
R3, R7	1 kΩ
R6	2 MΩ
C1, C2, C3	1 μF

Table 6-4: Summary of components for compensator

The power output stage is shown in figure 6-16. It is in a non-inverting configuration.
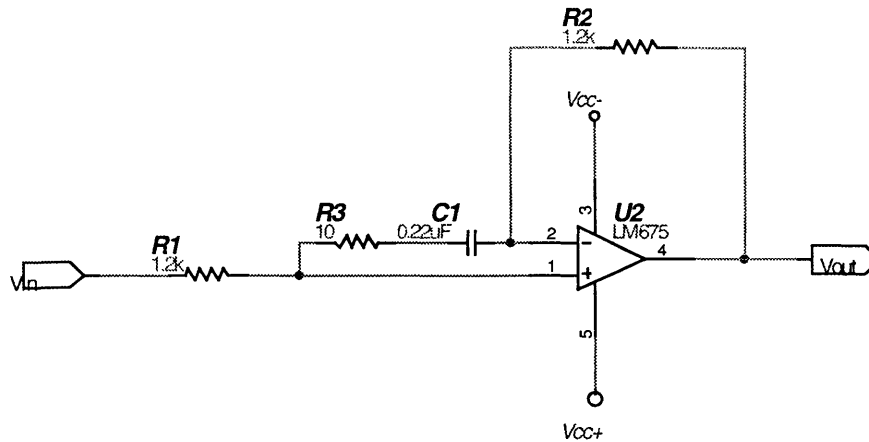
Figure 6-16: Schematic of power output stage

The LM675 is an attractive power op-amp because of its high output current capability. It should, however, be used with an appropriate sized heat sink. The component values are summarized in table 6-5.

R1, R2	1.2 kΩ
R3	10 Ω
C1	0.22 μ

Table 6-5: Summary of components for power output stage

6.4.3 Compare Stage

The next stage must convert the ac output from the sensor into a DC value that is of the same scale as the reference voltage used to set the amplitude at the input of the VCO. The first step is to rectify the ac signal and then use an active peak detection circuit to create a DC output corresponding to the maximum amplitude of the scan. Germanium diodes were used in the rectifier because of their lower voltage drop. The schematic for the rectifier with peak detection is given in figure 6-17. The component values are given in table 6-6.
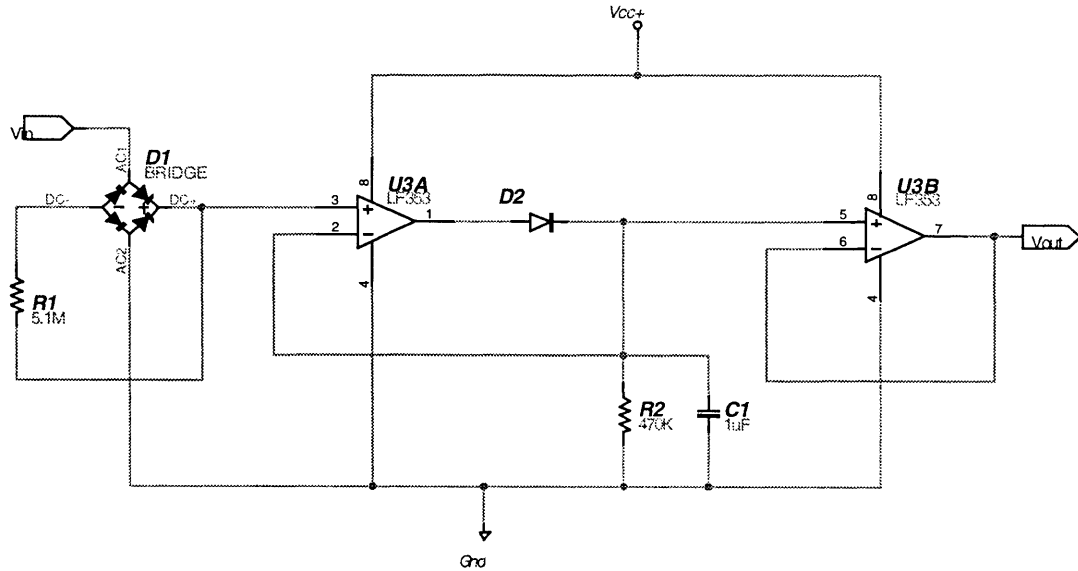
Figure 6-17: Schematic of rectifier with active peak detector

R1	5.1 MΩ
R2	470 kΩ
C1	1 μF
D1 (Bridge)	1N27 (Ge diode)
D2	1N400

Table 6-6: Summary of component values for rectifier and peak detector

The output of the peak detector will be on the order of mV and the reference voltage that sets the amplitude of the VCO sine wave is on a full volt scale. The peak detector output must be scaled appropriately so the two voltages can be compared. The main problem with this stage is the system gain changes dramatically with small variations in frequency when operating near resonance. The optimal way to implement this stage would be to have a frequency dependent gain. However, choosing a fixed gain produces acceptable results. The gain stage is shown below in figure 6-18. A gain of 18 was used, and an additional inverting op-amp was used to make the signal a positive voltage.
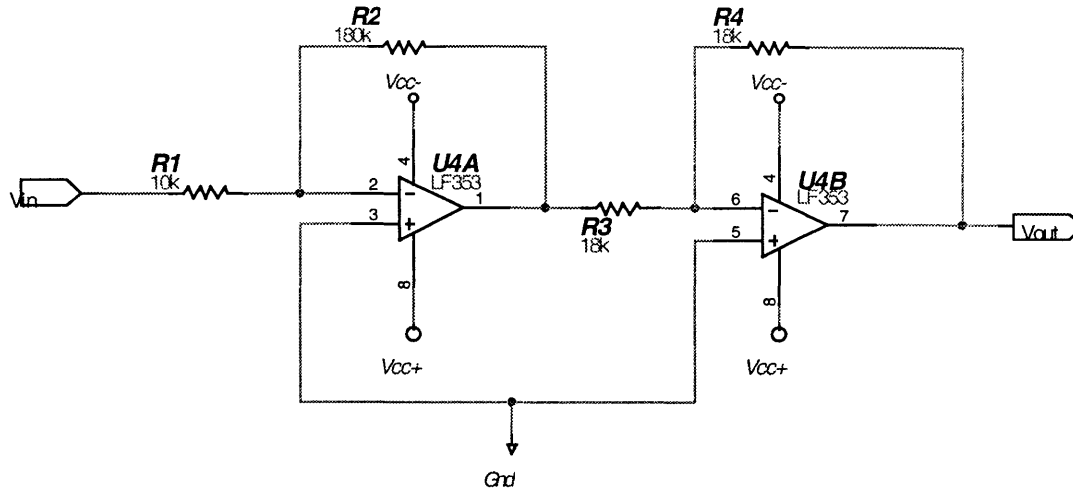
Figure 6-18: Schematic of gain stage with inverting output

Now the measured amplitude of the scan can be compared to the reference amplitude voltage. This is accomplished using a differential amplifier. There is also a variable gain associated with the difference. The schematic is shown in figure 6-19.
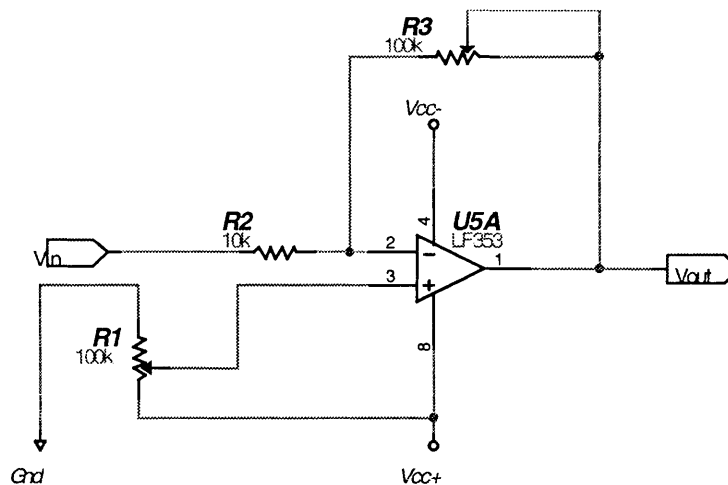
Figure 6-19: Schematic of compare stage

The potentiometer R1 adjusts the reference voltage. The transfer function for this schematic is given below. The potentiometer R3 varies the gain associated with the error term. This gain also affects the gain of the compensators overall performance. This stage can be thought of as the proportional gain portion of the controller.

$$V_{out} = V_{ref} + \frac{R_3}{R_2}\left(V_{ref} - V_{in}\right) \hspace{3cm} (6\text{-}18)$$

Table 6-7 summarizes the components used for this stage.

R1, R3	100 kΩ (pot)
R2	10 kΩ

Table 6-7: Summary of component values for compare stage

In addition to all the schematics shown above, by-pass capacitors were placed between the power supply rails where necessary.

Chapter 7

Experimental Measurements and Results

The previous chapters outlined the implementation scheme for the controllers. Measurements were taken to test the performance of the system. A photograph of the experimental set-up is shown below in figure 7-1.
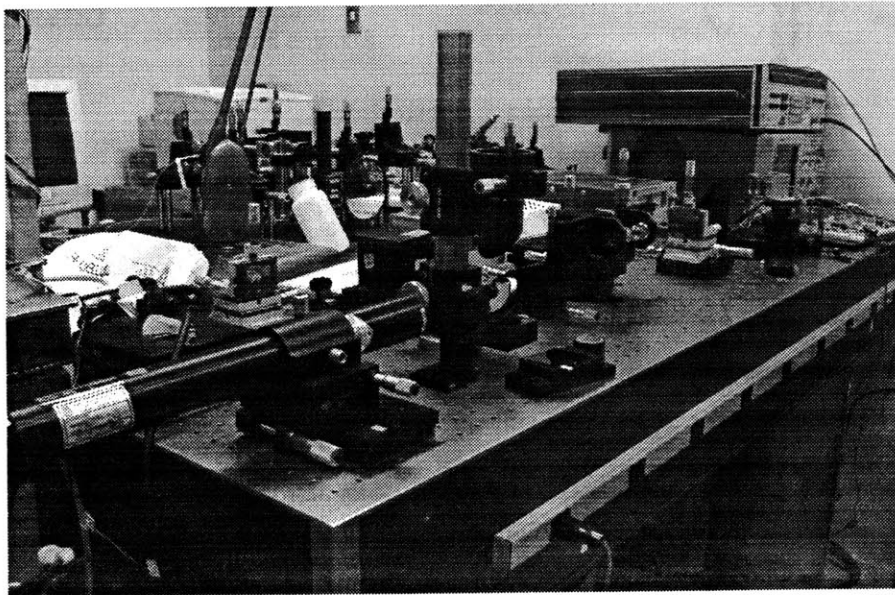
Figure 7-1: Experimental Set-up

This chapter will explain the experimental test set-up. It will also include the procedures for all measurements, including sensor calibration. The experimental data will then be presented with a brief discussion of their implications.

7.1 Experimental Test Set-up

The experiments were conducted in the Fiber Optics Laboratory at Draper Labs. The set-up allowed for easy calibration of the sensor. Figure 7-2 shows a simplistic outline of the set-up.
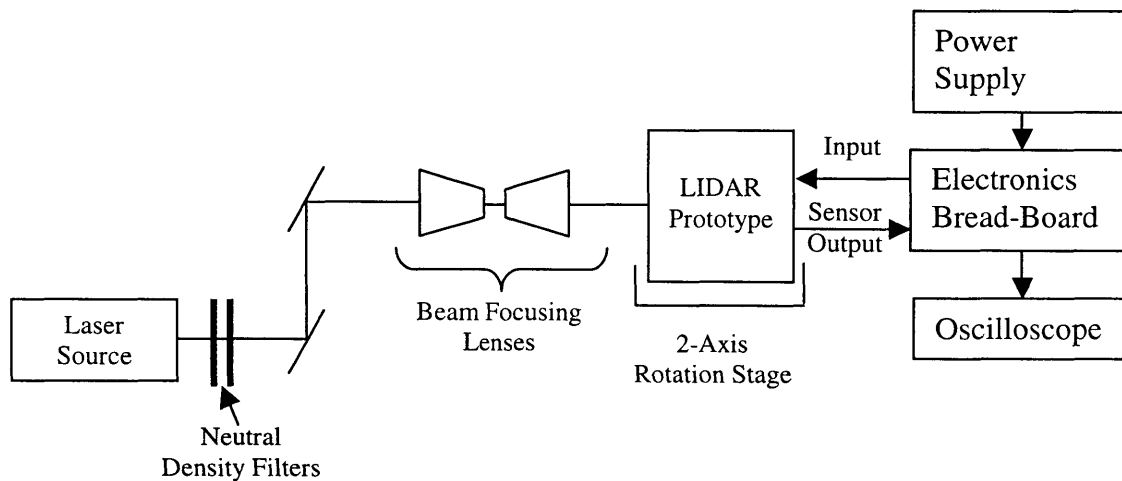
Figure 7-2: Experimental Set-up

The laser used was a Helium-Neon (HeNe) gas laser with a power rating of 20mW. The output of the laser was passed through a pair of neutral density filters that attenuated the power by approximately 3162, reducing the optical power to about 6.32μW. The laser beam is then passed through a periscope to translate the beam to the right height. A pair of matched objectives was used to focus the beam in order to adjust the beam waist diameter. All of these stages were necessary so as not to overpower the position sensor.

The LIDAR prototype was placed on a 2-axis rotation stage to allow for easy adjustments of the mirror relative to the incident laser beam. One concern with this setup was the actual angle of incidence of the laser onto the MEMS mirror could not be determined. The optimal incident angle was calculated in Chapter 3, and variations in that angle could result in non-linearities in the sensor output.

A DC power supply was used to power the electronics. The power supply provided a stable ±10V, +5V, and a common ground signal. The electronics were built on a prototyping bread-board. All measurements were taken using a 4-channel digital oscilloscope.

7.2 Sensor Calibration

The first step in the measurement process was to find the operating center of the sensor. As discussed in Chapter 3, when an incident beam hits the center of the sensor, the outputs should all have equal magnitudes. The outputs of all the current-to-voltage converters were viewed on the oscilloscope. The adjustable 2-axis stage that the LIDAR was positioned on was adjusted until the outputs matched each other.

After system calibration, it was noted that the laser did not hit the MEMS mirror near its geometric center. This suggests that the incident angle was in fact not at its optimal angle. A second calibration is performed while the mirror is oscillating. This produces an AC signal out of the sensor. Ideally, the output of the divider (representing the normalized position of the beam) should have a zero DC bias. However, due to incorrect incident angle, the output actually has a DC offset. The x-y stage was adjusted appropriately to minimize that offset. As a consequence, the results of all subsequent measurements were likely to have been affected.

It should also be noted that the sensor has a significant settling (on the order of 5 seconds) time before its output reaches a steady-state value. Therefore, the sensor should be allowed to "warm up" before any significant testing is performed.

Another major concern that was not evaluated during the design process was the possibility of multi-reflection paths between the sensor and the mirror. Figure 7-3 shows a possible scenario of the multi-path problem. More then one incident beam spot on the sensor could produce major errors in the measurements. The output of the sensor would represent a weighted average of the distances of the two spots, rather then the distance of just the primary spot. Fortunately, the multi-path problem did not seem to be a factor in the experimentation.
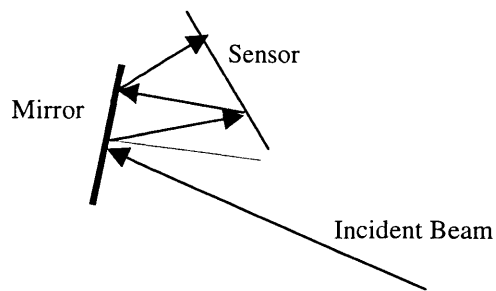
Figure 7-3: Illustration of Multi-path problem

7.3 System Measurements

The measurements taken validated the need for a good amplitude controller for the inner axis scan, but also highlighted many of the inadequacies in the components used to implement the control, and the control scheme itself.

The voltage-controlled oscillator is an essential part to the overall system, but its performance was far from ideal. Ideally, the VCO should output a sine wave with a stable frequency and amplitude that are functions of the input frequency and amplitude modulating voltages. The data sheet claims a typical frequency error of 1% and a maximum error of 4%. In either case, the error is significant enough to cause problems

for the closed loop system. The implication of these error margins will be discussed later. The output amplitude is also unstable. The amplitude also did not show stable performance. Figure 7-4 shows a sample output of the VCO.
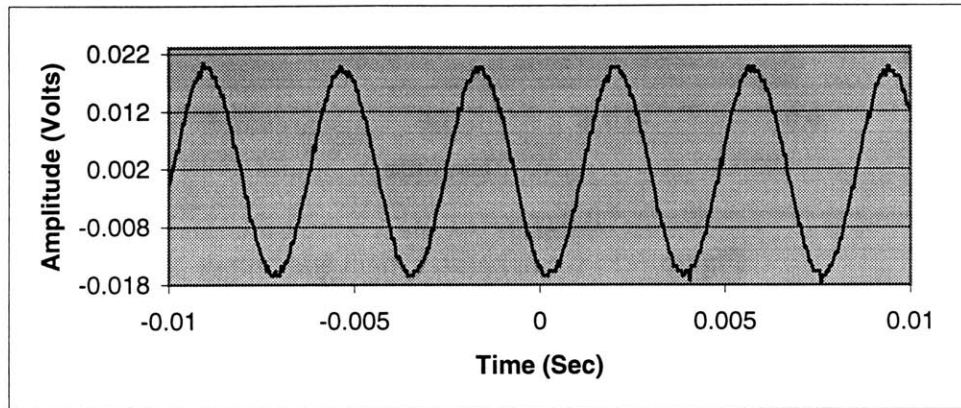
Figure 7-4: VCO Output

The harmonic distortion in the output can be adjusted, but the distortion changes as the amplitude and frequency are modulated, making it a very impractical adjustment. The DC bias of the output can also be adjusted, but the bias also drifts as the amplitude and frequency are modulated.

The compensator and power output stage performed very well. Figure 7-5 shows the input to the compensator (from the VCO) and the output of the compensator. The input amplitude is ~96mV (peak-to-peak) and the output amplitude is ~138mV (peak-to-peak). The frequency is ~175Hz, with approximately a 110° phase difference between the two signals. The phase difference agrees with the compensator design.
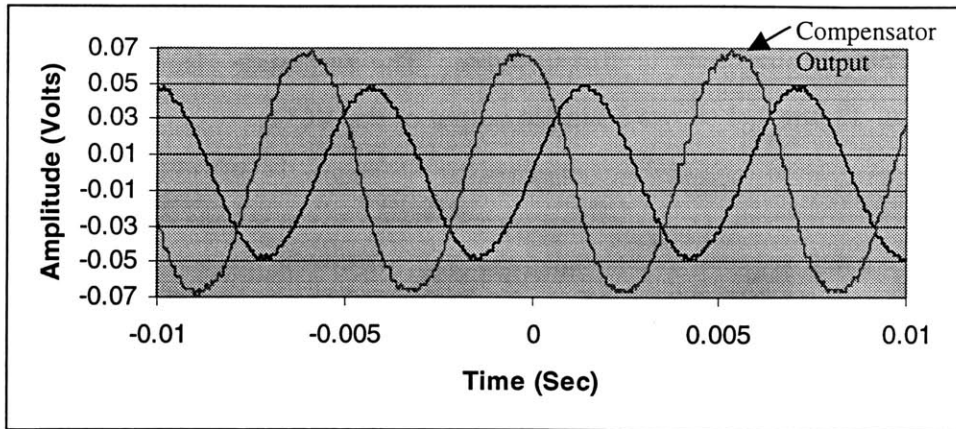
Figure 7-5: Compensator input and output

As a result of the instabilities in the VCO, the open loop performance of the inner axis will show rapid amplitude variations. Figure 7-6 shows a sample output of the sensor. The output displayed is the normalized output that comes from the divider (discussed in Chapter 3).
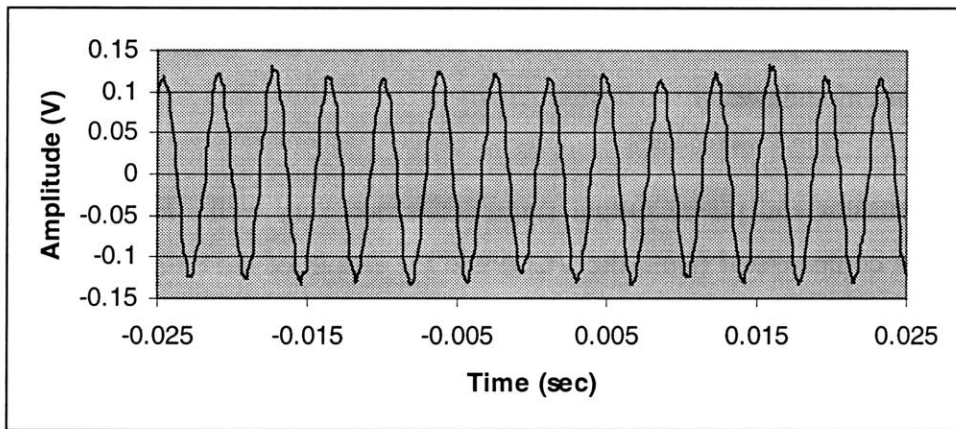
Figure 7-6: Sensor output (Open-loop)

The feedback signal should control the amplitude level at the VCO to compensate for the changes. Figure 7-7 shows the feedback signal and the reference signal. The feedback signal should attempt to minimize the difference between it and the reference voltage. The feedback signal does oscillate around the reference voltage as the amplitude changes. However, when the system was driven with the loop closed (using the feedback signal

shown in figure 7-6 to modulate the amplitude), the output oscillations of the sensor did not stabilize. In fact, the amplitude jitter increased.
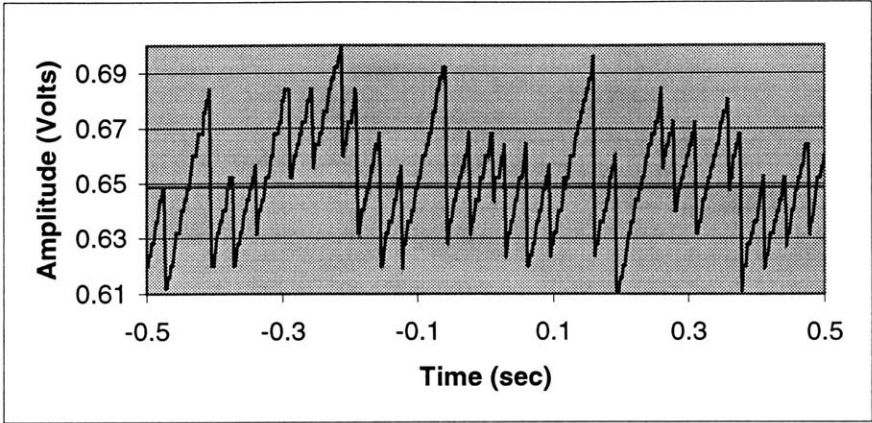
Figure 7-7: Feedback signal with reference voltage

A still image of a portion of the 2-dimensional scan is shown in figure 7-8. The scan image was made with the outer axis running in closed loop, and the inner axis running open loop.
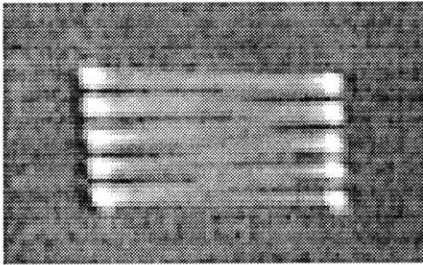
Figure 7-8: 2-Dimensionsal scan

Chapter 8

Conclusions

This thesis examined the feasibility of a MEMS-based scanning laser range finder. It produced an accurate model of the system dynamics and demonstrated the necessity for feedback control of its scan amplitude and frame rate.

Any attempt to design a model-based controller requires an accurate model description of the system. This thesis approached the development of a working model in two stages. The first stage developed a general model for the dynamics of a 2-axis mirror, described in Chapter 4. The rotational dynamics of such a system are highly non-linear with coupling between the rotation axes. In order to simplify the control design, it was shown using the method of multiple scales (Appendix D) that the dynamics could be decoupled and linearized. The implication of this analysis is that the control for the inner and outer axes could be designed independently without considering the coupling effects.

Using these results, detailed models of the outer and inner axes were developed. Chapter 5 described the model for the DC-motor used to actuate the outer-axis. Using that model a design for the outer axis speed controller was implemented. Chapter 6 derived the inner axis model. The DC-motor model developed in Chapter 5 was mapped to the inner axis

97

problem. Using the motor model to describe the inner axis produced excellent results as verified by experimentation (section 6.2). The design of the inner axis controller involved the use of classical control theory. A second order lead network cascaded with a lag network was used to stabilize the system. The implementation of the control scheme is discussed in section 6.4.

Experimental measurements verified the need for a robust controller, and also highlighted the inadequacies of the proposed control solution. One of the primary concerns during the experimentation was the instability of the voltage-controlled oscillator (VCO) used to generate the actuating signal for the inner axis. Variations in the VCO's output amplitude and frequency produced a jiggling effect on the output of the scan. The controller did not model the VCO's performance, and therefore the closed loop performance of the inner axis did not meet expectations. The controller did produce the proper feedback signal, as shown in figure 7-7, however it is suspected that the VCO could not follow the rapid changes of the feedback control signal. A more detailed discussion of the experimental procedure and results are given in Chapter 7.

The general approach of this thesis proved to be very effective. Rigorous analysis followed by experimental verification helped develop a thorough understanding of the system as a whole. It becomes a much easier process to identify problems and explain achievements with this understanding. Inadequacies in the system model are quickly unveiled through experimentation and provide immediate direction for further improvements.

8.1   Suggestions for Future Work

The results of this thesis should provide enough motivation to continue work on the LIDAR. The LIDAR can be improved with regards to all its parameters, including size, weight, power consumption, and feedback performance. It is the hope of the author that this thesis provided the necessary framework to continue the development of the LIDAR. The author therefore presents the following suggestions for improvements.

8.1.1 LIDAR Size Improvements

Decreasing the size of the LIDAR is not only desirable for the sensor as a whole, but can actually improve the performance of the sensor itself. One of the main sources of inefficiency of the system comes from the large air gap of the electromagnet. This is a direct consequence of the size and design of the MEMS mirror. By decreasing the size of the mirror, the electromagnet air gap can also be reduced which will greatly increase the available torque to drive the mirror. Furthermore, a more compact design in the MEMS mirror could result in a smaller moment of inertia, also resulting in less power consumption for the overall system.

Currently, the position sensor dominates the overall size of the sensor. Unfortunately, there are not many commercial sensors available that can give the desired performance. There are two general options to decrease the sensor size. The first involves the development of a custom optical sensor that meets performance and size specifications. The other option is to investigate different sensor options that can be used to close a feedback loop. One possible option is to incorporate a piezo-electric sensor on the actual flexure in the MEMS mirror assembly. The deflection of the flexure beam is proportional to the position of the mirror. This type of a sensor would offer a dramatic reduction in size.

The outer axis actuation could also be modified to reduce the size of the LIDAR. The DC motor offered a simple and quick solution to generate the outer axis scan. However, the motor is relatively large, and its physical integration into the overall package can be difficult. Different actuation methods should be investigated. One possible alternative is to attempt to incorporate an electromagnetic actuation similar to the inner axis. This would result in significant size improvements, but would increase the complexity of the control system.

8.1.2 Power Consumption Improvements

The power consumption of the LIDAR prototype approached 1 Watt. Clearly, the size improvements suggested above will result in less power consumption. Small gains in power consumption can always be achieved by optimizing the electronics. The circuit implementation of the system is not an optimal implementation and a little more effort in the design could reduce the overall power consumption.

Another main loss in power comes from the electromagnet core. The core used was made from a solid piece of steel. This design was chosen to speed the development of the prototype and does not represent the ideal solution. In future models, the electromagnet core should be laminated and constructed with ferrite. This will reduce the eddy current losses and leakage losses that were predominate with the solid core design.

It should be noted that a complete LIDAR system will also have an optical portion that includes the laser source, laser driver, and collection optics and electronics. This portion will dominate the power consumption of the overall system, and care should be taken with its design.

8.1.3 Control Improvements

The control system has much room for improvement. The scheme used to control the system only dealt with one parameter of the system: the scan amplitude. However, due to the high Q of the mirror, the frequency of the output must also be measured and used in the control. There is a direct relationship between the gain of the plant and the frequency at which it is driven. A top-level block diagram of a modified control solution is given in figure 8-1.

Currently, the controller assumes that the system will be driven at a fixed frequency. Assuming that the VCO is stable, the system gain can be predetermined for that

frequency and hard wired into the control. However, the moment the frequency drifts (either due to instability in the VCO, or temperature variations), the predetermined gain will not be correct resulting in incorrect control.
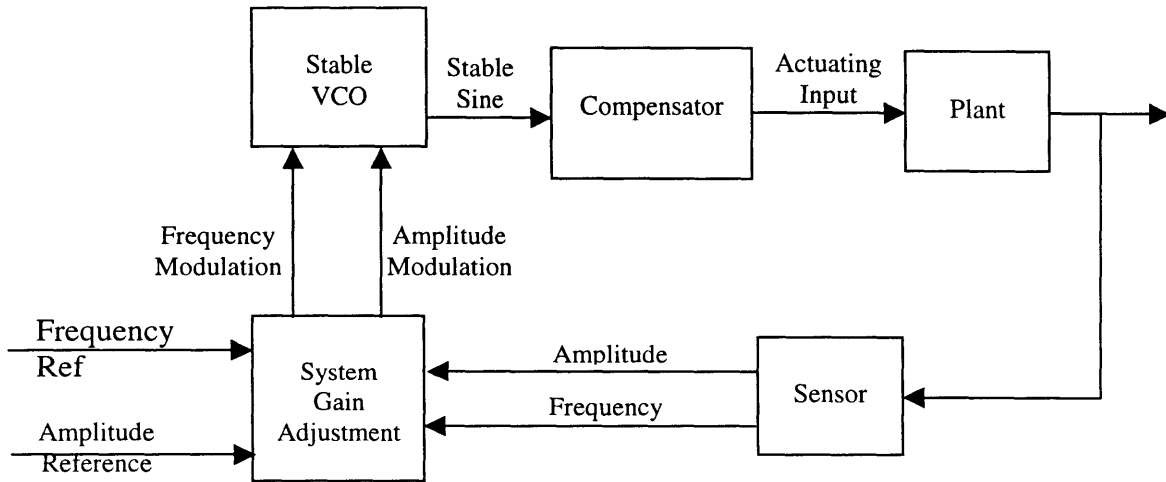
Figure 8-1: Improved controller design

The proposed improvement consists of three primary additions. The first involves internal compensatoin of the VCO. Using well known methods such as Phase-locked loops, the VCO output can be compensated to produce a stable frequency and amplitude output. This alone would greatly improve the performance of the system.

The next addition involves the processing of the sensor output. Currently, only the amplitude is used in the controller. The frequency of the output should also be measured.

The last addition represents the main improvement. The system gain adjustment block accomplishes many tasks, and might be best implemented using a digital microcontroller. This block will control the scan amplitude by adjusting either the amplitude or the frequency of the VCO output. It takes advantage of the frequency dependant gain of the system. If the amplitude is too small, it might make more sense to move the frequency closer to resonance rather then trying to make large sweeps in the amplitude.

This new control scheme is more complicated than the original implementation. A multi-input system requires more analysis and the implementation would most likely involve both analog and digital components.

Appendix A

Beam Trace Analysis for LIDAR

This appendix details the analytical solution for plotting the beam trace of a scanning laser range finder. In order to interpret the data from the scanning laser correctly, a model of the scan image projected onto the real world must be generated. This map will allow any distortions in the image to be corrected.

For simplicity, it is assumed that the laser beam hits the mirror at its geometric center. It is also assumed that all the rotations of the mirror occur about its geometric center (i.e. there are no off-center rotations). The trace of the reflected beam is measured on either a flat screen located a fixed distance away from the mirror, or a spherical screen located at a fixed radius from the mirror.

The first step in the analysis was to set up a fixed reference frame and determine which position vectors are known, and which vectors need to be calculated. Figure A-1 shows a simplified version of the optical system with labeled vectors and coordinate frame.
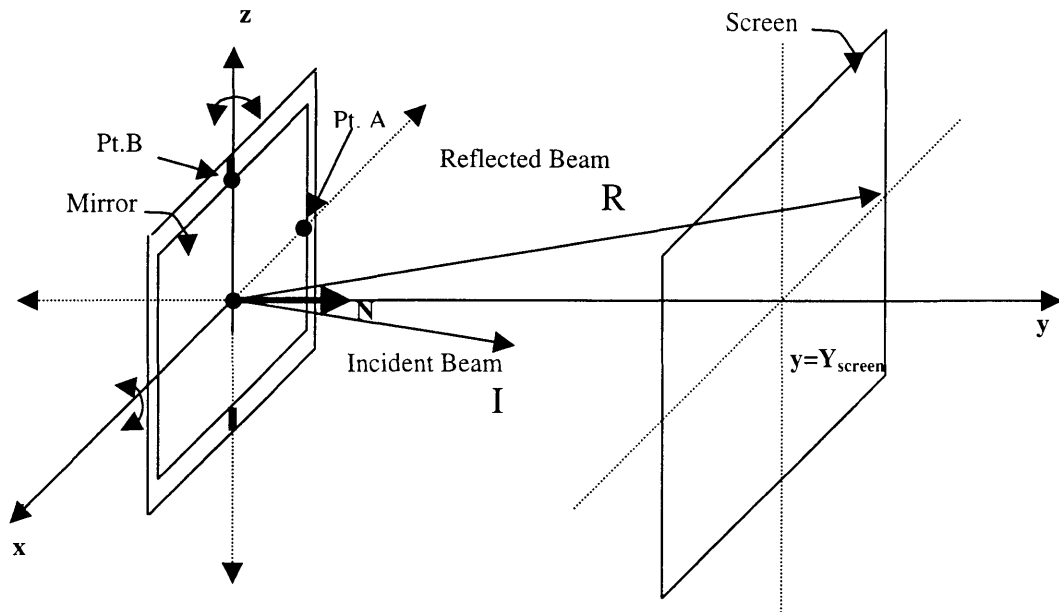
Figure A-1: Vector representation of optical system

Given the previous assumptions and the above diagram, all the vectors can be calculated. The following information is known or assumed:

- The Incident Beam Vector.

$$\vec{I} = \begin{bmatrix} I_x & I_y & I_z \end{bmatrix} \qquad \text{(A-1)}$$

- The plane of the screen.

$$y = Y_{screen} \qquad \text{(A-2)}$$

- The mirror plane can rotate about the **x**-axis, sweeping through an angle φ in the **y-z** plane.

- The mirror plane can rotate about the line defined by the origin and point **B**, sweeping through an angle θ in the plane defined by the Normal vector and the vector defined by the origin and point **A**, the θ-plane.
- The mirror has length l and height h.

The following information must be determined or calculated from the above assumptions.

- The points **A** and **B** as a function of θ and φ. Once those points are determined, the plane of the mirror can be defined given any rotation of θ and φ.
- The normal vector N, to the plane of the mirror. This normal vector is the cross product of the vectors defined by the origin and points **A** and **B**.

$$\vec{N} = \vec{B} \times \vec{A} \tag{A-3}$$

- The reflected beam vector R.

Determining the points **A** and **B** involves simple trigonometry. Point **B** is much simpler to calculate due to the dynamics of the mirror rotation. Point **B** is always located on one of the axes of rotation. Its position only changes with rotations about the **x**-axis. Therefore, point **B** only has a φ dependence. Furthermore, at φ=0°, B=[0 0 *h/2*], and at φ=90°, B=[0 –*h/2* 0]. Given this information, it is clear that point **B** traces out a circle in the **y-z** plane. Finally, the point can be written in general as:

$$B = \left[0 \quad -\frac{h}{2}\sin\varphi \quad \frac{h}{2}\cos\varphi \right] \tag{A-4}$$

Point **A** involves a little more analysis. Unlike point **B**, point **A** is not fixed on any of the axes of rotation. It has both a θ and φ dependencies. Figure A-2 is a graphical representation of some of the possible paths point **A** could follow. Given this picture, the exact coordinates of point **A** given any θ or φ can be determined.
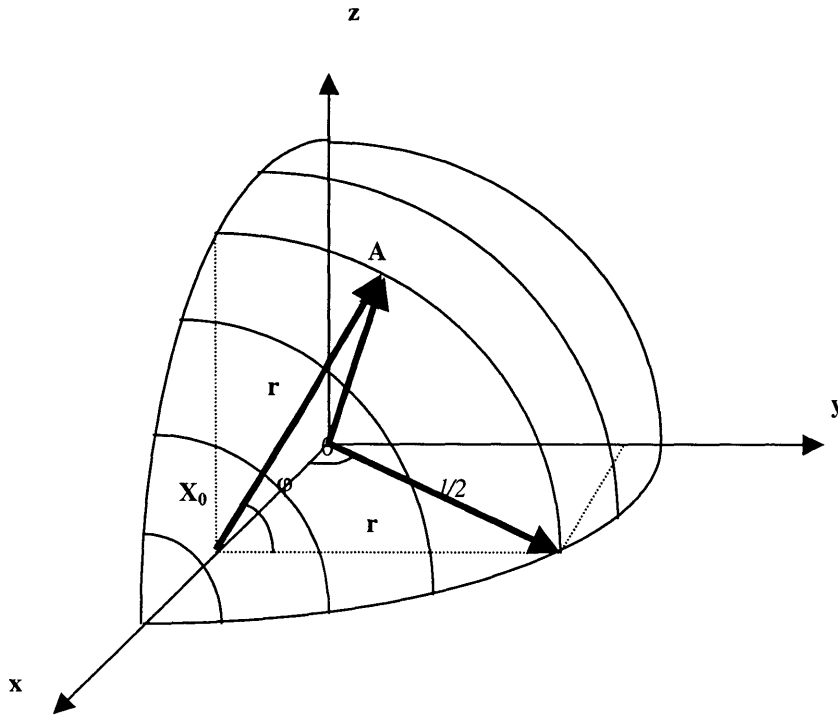
Figure A-2: Sample paths of point A

From the diagram, it can be seen that the x-coordinate of point **A** only depends on θ: $A_x = (l/2)\cos(\theta)$. To determine the **y** and **z** coordinates, notice what happens given the following sequence of rotations. A rotation through the θ-plane of an angle θ will move the **y** coordinate to $(l/2)\sin(\theta)$. Now, rotating the point about the **x**-axis will trace a circle of radius $r = (l/2)\sin(\theta)$. Determining the **y** and **z** coordinates now reduces to simple trigonometry again: $A_y = r\cos(\varphi)$ and $A_z = r\sin(\varphi)$. Now, point **A** can be completely written as a function of θ and φ.

$$A = \left[\frac{l}{2}\cos\theta \quad \frac{l}{2}\sin\theta\cos\varphi \quad \frac{l}{2}\sin\theta\sin\varphi\right] \qquad \text{(A-5)}$$

Now that points **A** and **B** are completely determined, calculating the normal vector to the plane of the mirror is straight forward using equation A-3.

$$\bar{N} = \begin{bmatrix} \hat{i} & \hat{j} & \hat{k} \\ 0 & -\dfrac{h}{2}\sin\varphi & \dfrac{h}{2}\cos\varphi \\ \dfrac{l}{2}\cos\theta & \dfrac{l}{2}\sin\theta\cos\varphi & \dfrac{l}{2}\sin\theta\sin\varphi \end{bmatrix} \qquad \text{(A-6)}$$

Explicit computation of the normal vector will be performed using MATLAB. For simplicity, the normal vector will be denoted as follows:

$$\bar{N} = \begin{bmatrix} N_x & N_y & N_z \end{bmatrix} \qquad \text{(A-7)}$$

The next step in the analysis is to determine the reflected beam vector. From basic principles in optics, it is known that the angle of incidence = angle of reflection. In vector terms, this means that <I,N> = <R,N> (<> is a projection, or 'dot' product). The reflected beam vector is the rotation of the incident beam vector through the normal vector by an angle of 2γ, where γ is the angle between **I** and **N**. Given any 3-D vector **I** and **N**, the described rotation is non-trivial in the original coordinate frame. The problem can be simplified by defining a new coordinate frame with the normal vector as one of the axes. The new axes will be defined as follows:

$$\bar{Q} = \bar{I} \times \bar{N} \qquad \text{(A-8)}$$

$$\bar{L} = \bar{N} \times \bar{Q} \qquad \text{(A-9)}$$

The vectors **N, L,** and **Q** form an orthogonal coordinate frame. The vectors **n, l,** and **q** represent the normalized vectors **N, L,** and **Q**. Given the new set of axes, the incident beam vector must be rewritten in terms of the new coordinate frame.

$$\vec{I}_{\hat{n},\hat{l},\hat{q}} = \begin{bmatrix} \vec{I} \cdot \hat{n} & \vec{I} \cdot \hat{l} & \vec{I} \cdot \hat{q} \end{bmatrix} \tag{A-10}$$

Now, the reflected beam vector can be written by inspection.

$$\vec{R}_{\hat{n},\hat{l},\hat{q}} = \begin{bmatrix} \vec{I} \cdot \hat{n} & -\vec{I} \cdot \hat{l} & -\vec{I} \cdot \hat{q} \end{bmatrix} \tag{A-11}$$

Finally, the reflected beam vector can now be written in terms of the original coordinate system:

$$\vec{R} = \left(\vec{I} \cdot \hat{n} \right)\hat{n} + \left(-\vec{I} \cdot \hat{l} \right)\hat{l} + \left(-\vec{I} \cdot \hat{q} \right)\hat{q} \tag{A-12}$$

The last step in the analysis is to determine where the reflected beam hits the screen. This problem becomes simplified if the reflected beam vector is decomposed into its component vectors; the projection onto the **x-y** plane and the projection onto the **y-z** plane. Figure A-3 illustrates how to determine the **x**-coordinate of the reflected beam onto the screen using only the **x-y** plane projection of the reflected beam vector.

$$\theta_{x-y} = \tan^{-1} \frac{R_y}{R_x} \tag{A-13}$$

$$\varphi_{y-z} = \tan^{-1} \frac{R_z}{R_y} \tag{A-14}$$

$$X_{screen} = \frac{Y_{screen}}{\tan \theta_{x-y}} \tag{A-15}$$

$$Z_{screen} = Y_{screen} \tan \varphi_{y-z} \tag{A-16}$$

108
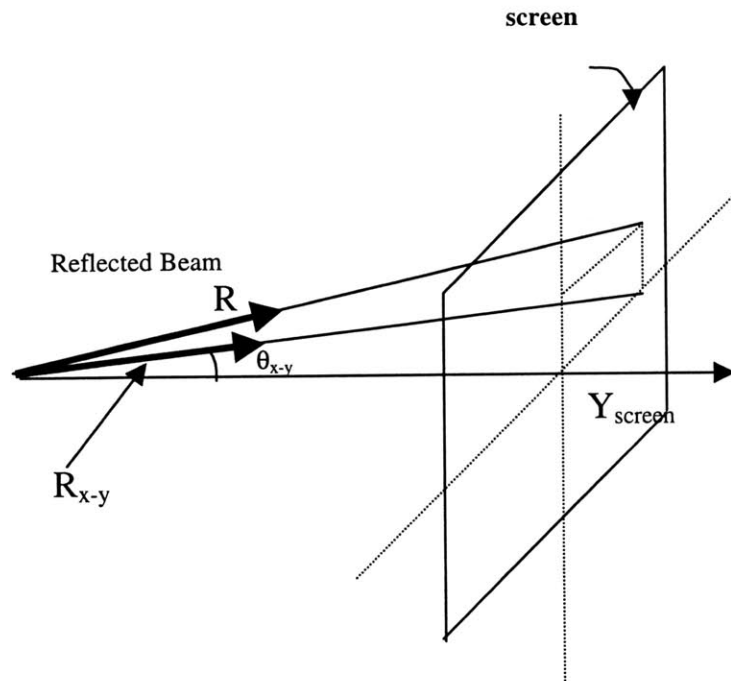
Figure A-3: Projection of reflected beam vector onto the x-y plane, and its extension
onto the screen

The above analysis was implemented in MATLAB. The MATLAB script is appended at the end of this document. Figure A-4 shows the beam trace for a rotation of +/- 25° in both θ and φ with the laser source located along the **y-axis**.
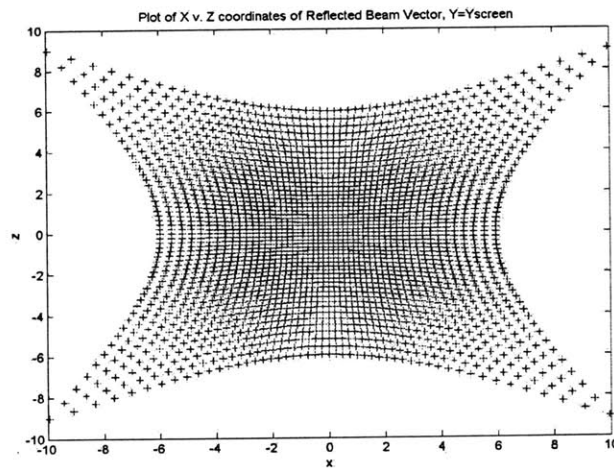
Figure A-4: Sample beam trace (50°x50°) on a rectangular screen

This plot clearly shows the non-linearity of the beam trace. The beam trace moves like **tanθ**, which accounts for the curvature. The non-linearity in the trace can be corrected for at the computational level (i.e. in MATLAB) to produce a more "linear" trace.

Figure A-5 shows the same trace as figure A-4, except now a spherical screen was used rather then a flat screen. This is a more natural representation of the data, since in reality the scanner will usually not be interrogating a flat screen. It will be scanning an arbitrary environment with objects located at coordinates (r, θ, φ).
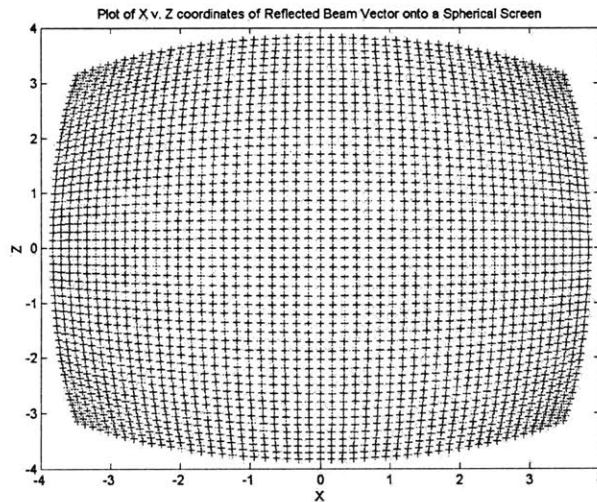
Figure A-5: Sample beam trace (50°x50°) on a spherical screen

Although there is still some curvature at the edges of the trace, it is not as pronounced as the flat screen trace. The exact function describing the curvature onto a spherical screen has not been determined. Further analysis should lead to a screen shape that produces a rectangular beam trace.

The sample traces shown above do not represent an accurate description of the real system. The laser source cannot be placed normal to the mirror, or it would interfere with the reflected beam. This means that the laser must be placed at an angle γ to the normal of the mirror in its θ=0, φ=0 position. The larger γ is the sooner the tanθ characteristics begin appear. Figure A-6, A-7, and A-8 shows three scans with the laser placed at 10°,

20°, and 45° to the normal of the mirror in its θ=0, φ=0 position. Clearly, the larger the angle between the laser and the nominal position of the mirror is, the greater the tanθ affects become. The optimal position for the laser is the point where the angle between the laser and the normal of the mirror at its nominal position is the smallest, while not interfering with the actual beam path.
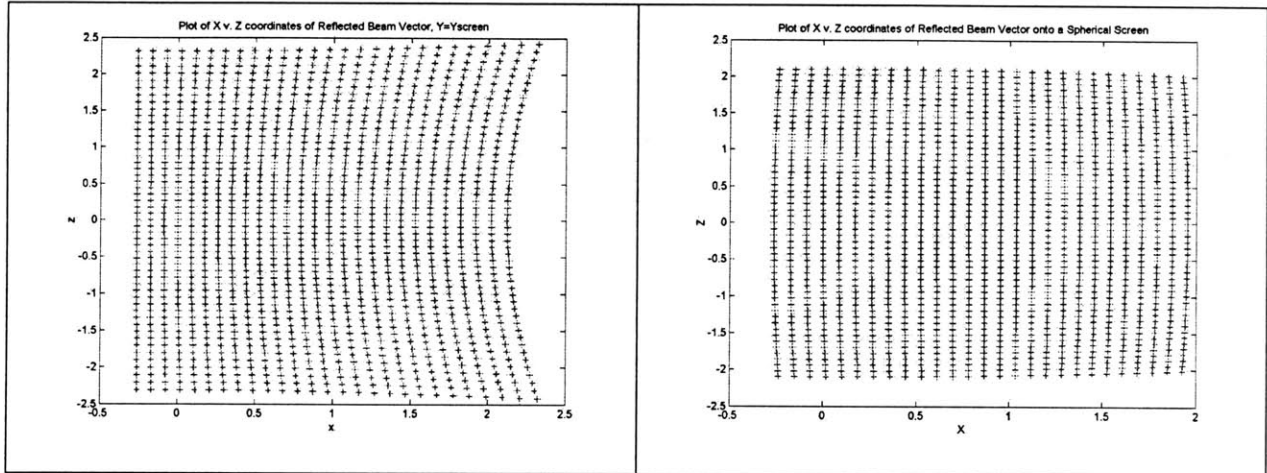
(a)   (b)

Figure A-6: Sample beam trace (13°x25°), γ=10° (a) Flat screen (b) Spherical screen
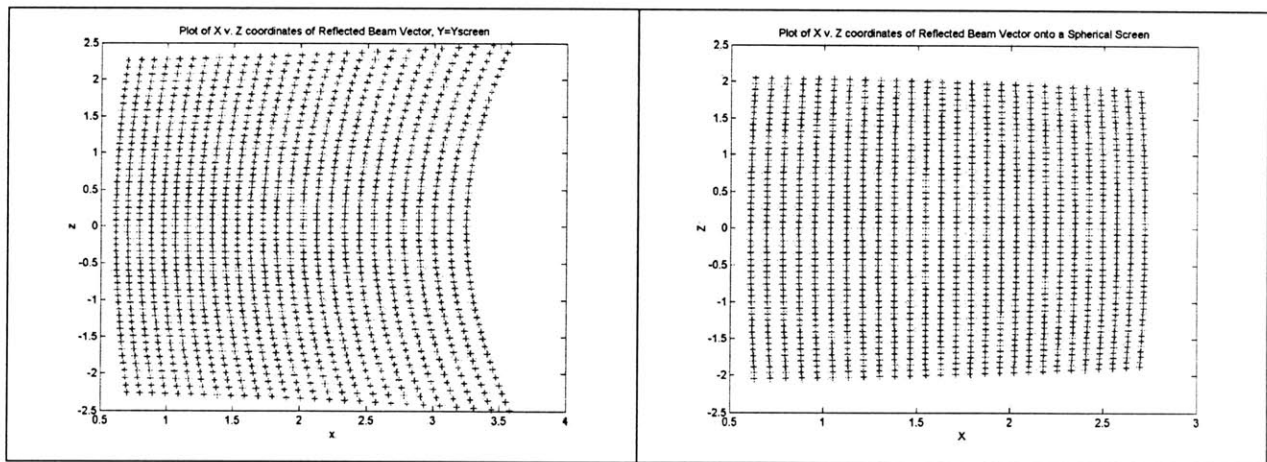
(a)   (b)

Figure A-7: Sample beam trace (13°x25°), γ=20° (a) Flat screen (b) Spherical screen
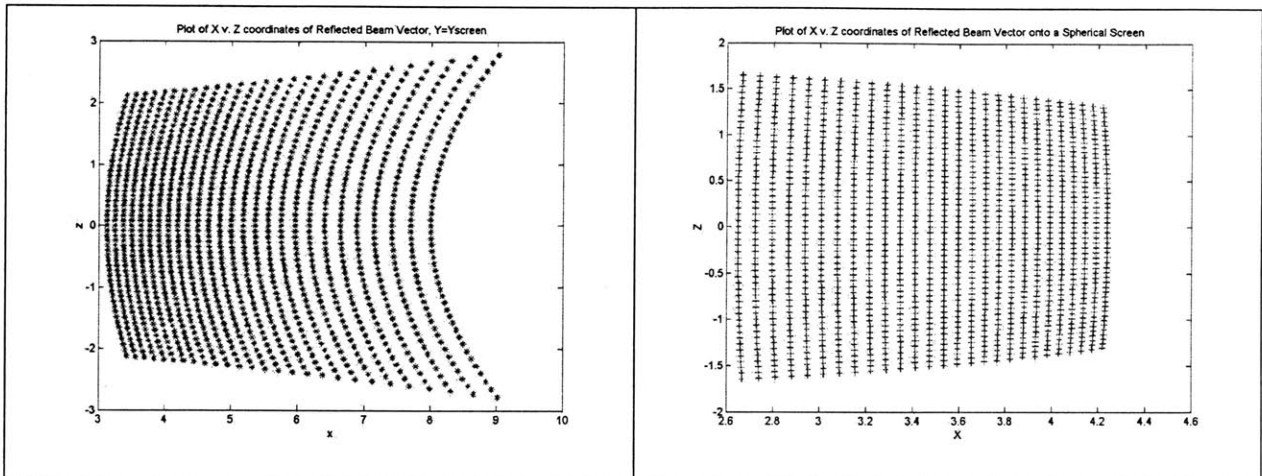
(a)   (b)

Figure A-8: Sample beam trace (13°x25°), γ=45° (a) Flat screen (b) Spherical screen

A.1 MATLAB Script

```
function [Normal0, RBeam0, SCREEN] =
BeamTrace(thetad,phid,l,h,Yscreen,Laser)

%BeamTrace will produce the Laser-Beam Trace of a Laser that is
reflected off
%a double-gimbled mirror onto a screen.  The function will output the
Normal
%vector to the mirror, the Reflected Beam vector, and a 2-D plot of the
beam
%trace.
%
%The program was written with the following specifications/assumptions:
%
%The mirror is centered about the origin of an x-y-z coordinate frame.
%The mirror lies in the x-z plane defined by y=0.
%The mirror rotates about the z-axis by an angle theta (user input;
vector, degrees)
%The mirror rotates about the x-axis by an angle phi  (user input;
vector, degrees)
%The length of the mirror is l (user input; scalar)
%The height of the mirror is h (user input; scalar)
%The screen lies in the x-z plane defined by y=Yscreen (user input;
scalar)
%The laser is located 3-space and is specified by Laser = [Xlaser
Ylaser Zlaser]

%Normalized Laser vector
Laser0 = Laser/(norm(Laser));
```

```
%Convert theta and phi vectors into radians
theta = (pi/180)*thetad;
phi   = (pi/180)*phid;

%Find length of theta and phi vectors
ltheta = length(theta);             %N-D vector
lphi   = length(phi);               %K-D vector
NK     = ltheta*lphi;

%Given an angle theta and phi, determine three points that completley
%define the plane of the mirror.  For every value theta the mirror will
%sweep through all values of phi.  There are NK possible angle
combinations.
%Each point is a 3-D vector.  Each mirror point will be a NKx3 vector.
%In general, the 3 points are:
%[0 0 0]
%[(1/2)cos(theta) (1/2)sin(theta)cos(phi) (1/2)sin(theta)sin(phi)]
%[0 -(h/2)sin(phi) (h/2)cos(phi)]


O = [0 0 0];


MirrorPt1 = repmat(O,NK,1);  %First point of Mirror plane is a vector
                             %composed of NK origin pts (3xNK Matrix)

row = 1;                     %Initilize variable for row of matrix
while row < (NK)+1,              %Build vector of mirror point 2
    for T = 1:ltheta
      for P = 1:lphi
          MirrorPt2(row,1) = (1/2)*cos(theta(T));
              MirrorPt2(row,2) = (1/2)*sin(theta(T))*cos(phi(P));
              MirrorPt2(row,3) = (1/2)*sin(theta(T))*sin(phi(P));
          row = row + 1;
        end
    end
end


row = 1;                 %Initilize variable for row of matrix
while row < (NK)+1,          %Build vector of mirror point 3
    for T = 1:ltheta
      for P = 1:lphi
          MirrorPt3(row,1) = 0;
              MirrorPt3(row,2) = -(h/2)*sin(phi(P));
              MirrorPt3(row,3) = (h/2)*cos(phi(P));
          row = row + 1;
        end
    end
end

%Calculate the Normal vector for each mirror plane.
%Normal will be a NKx3 matrix
%Take cross product of each row MirrorPt2 and MirrorPt3
Normal = cross(MirrorPt3',MirrorPt2')';

%Due to MATLAB precision, a threshold for allowable values
%must be set.  An value<1e-8 will be set to 0
[i,j] = find((abs(Normal)<1e-8)&(abs(Normal)>0));
if isempty([i,j])==0
```

```
        for fixij = 1:length(i)
            Normal(i(fixij),j(fixij)) = 0;
        end
    end

%Normalize the Normal vector
for row = 1:NK
    mag(row,1)=(norm(Normal(row,:)));
    if mag(row,1)==0
        mag(row,1)=1;
    end
    Normal0(row,1)  = (1/mag(row,1))*Normal(row,1);
    Normal0(row,2)  = (1/mag(row,1))*Normal(row,2);
    Normal0(row,3)  = (1/mag(row,1))*Normal(row,3);
end
[i,j]   = find(((abs(Normal0)<1e-8)&(abs(Normal0)>0)));
if isempty([i,j])==0
    for fixij = 1:length(i)
        Normal0(i(fixij),j(fixij)) = 0;
    end
end

%To calculate the Reflected Beam vector, a new coordinate frame
%will be defined.  NORMAL0,Q0,L0

%First, construct an NKx3 matrix of the Laser vector
LASER0=repmat(Laser0,NK,1);
[i,j]   = find(((abs(LASER0)<1e-8)&(abs(LASER0)>0)));
if isempty([i,j])==0
    for fixij = 1:length(i)
        LASER0(i(fixij),j(fixij)) = 0;
    end
end
%Create a set of vectors Q that are orthogonal to the Laser0 vectors
%and the Normal vectors
Q=cross(LASER0',Normal0')';
[i,j]   = find(((abs(Q)<1e-8)&(abs(Q)>0)));
if isempty([i,j])==0
    for fixij = 1:length(i)
        Q(i(fixij),j(fixij)) = 0;
    end
end

%Normalize Q vectors
for row = 1:NK
    mag(row,1)=(norm(Q(row,:)));
    if mag(row,1)==0
        mag(row,1)=1;
    end
    Q0(row,1)=(1/mag(row,1))*Q(row,1);
    Q0(row,2)=(1/mag(row,1))*Q(row,2);
    Q0(row,3)=(1/mag(row,1))*Q(row,3);
end
[i,j]   = find(((abs(Q0)<1e-8)&(abs(Q0)>0)));
if isempty([i,j])==0
    for fixij = 1:length(i)
        Q0(i(fixij),j(fixij)) = 0;
```

```
        end
end

%Create a set of vectors L that are orthogonal to the Normal and Q
vectors
L=cross(Normal0',Q0')';
[i,j]  = find((abs(L)<1e-8)&(abs(L)>0));
if isempty([i,j])==0
    for fixij = 1:length(i)
        L(i(fixij),j(fixij)) = 0;
    end
end

%Normalize L vectors
for row = 1:NK
    mag(row,1)=(norm(L(row,:)));
    if mag(row,1)==0
        mag(row,1)=1;
    end
    L0(row,1)=(1/mag(row,1))*L(row,1);
    L0(row,2)=(1/mag(row,1))*L(row,2);
    L0(row,3)=(1/mag(row,1))*L(row,3);
end
[i,j]  = find((abs(L0)<1e-8)&(abs(L0)>0));
if isempty([i,j])==0
    for fixij = 1:length(i)
        L0(i(fixij),j(fixij)) = 0;
    end
end

%Redefine the Laser vector in terms of the new coordinate frame.
LaserNQL =[(sum(LASER0'.*Normal0'))'  (sum(LASER0'.*Q0'))'
(sum(LASER0'.*L0'))'];

[i,j]  = find((abs(LaserNQL)<1e-8)&(abs(LaserNQL)>0));
if isempty([i,j])==0
    for fixij = 1:length(i)
        LaserNQL(i(fixij),j(fixij)) = 0;
    end
end

%Normalize the new Laser vectors
for row = 1:NK
    mag(row,1)=(norm(LaserNQL(row,:)));
    if mag(row,1)==0
        mag(row,1)=1;
    end
    LaserNQL0(row,1)=(1/mag(row,1))*LaserNQL(row,1);
    LaserNQL0(row,2)=(1/mag(row,1))*LaserNQL(row,2);
    LaserNQL0(row,3)=(1/mag(row,1))*LaserNQL(row,3);
end
[i,j]  = find((abs(LaserNQL0)<1e-8)&(abs(LaserNQL0)>0));
if isempty([i,j])==0
    for fixij = 1:length(i)
        LaserNQL0(i(fixij),j(fixij)) = 0;
    end
end
```

```
%The reflected beam is the incident beam rotated through the normal
vector
%by an angle of 2*gamma  (gamma is the angle between the incident and
normal)
%This is easily found by changing the sign of the Q and L components of
the
%LaserNQL0 vector
%Create a diagnol matrix that will change the sign of the last 2 col of
a vector
A=-eye(3);
A(1,1)=1;

RBeamNQL0 = LaserNQL0*A;

%Now, convert RBeamNQL0 back into original coordinate frame
RBeam = diag(RBeamNQL0(:,1))*Normal0 + diag(RBeamNQL0(:,2))*Q0 +
diag(RBeamNQL0(:,3))*L0;

%Normalize RBeam
for row = 1:NK
    mag(row,1)=(norm(RBeam(row,:)));
    if mag(row,1)==0
        mag(row,1)=1;
    end
    RBeam0(row,1)=(1/mag(row,1))*RBeam(row,1);
    RBeam0(row,2)=(1/mag(row,1))*RBeam(row,2);
    RBeam0(row,3)=(1/mag(row,1))*RBeam(row,3);
end
[i,j]  = find((abs(RBeam0)<1e-8)&(abs(RBeam0)>0));
if isempty([i,j])==0
    for fixij = 1:length(i)
        RBeam0(i(fixij),j(fixij)) = 0;
    end
end

%Calculate the points where the Reflected beam vector intersects
%the screen at y=Ys.

for row = 1:NK
    magxy=norm(RBeam0(row,1),RBeam0(row,2));
    magyz=norm(RBeam0(row,2),RBeam0(row,3));
    if magxy==0
        magxy=1;
    end
    if magyz==0
        magyz=1;
    end
    SCREEN(row,1)=Yscreen/(tan(atan(RBeam(row,2)/RBeam(row,1))));
    SCREEN(row,2)=Yscreen*(tan(atan(RBeam(row,3)/RBeam(row,2))));
end
[i,j]  = find((abs(SCREEN)<1e-8)&(abs(SCREEN)>0));
if isempty([i,j])==0
    for fixij = 1:length(i)
        SCREEN(i(fixij),j(fixij)) = 0;
    end
end
```

```
%Plot the Beam Trace
figure(1);
plot(SCREEN(:,1),SCREEN(:,2),'b*');
title('Plot of X v. Z coordinates of Reflected Beam Vector,
Y=Yscreen');
xlabel('x');
ylabel('z');

%figure(2);
%plot(Yscreen*RBeam0(:,1),Yscreen*RBeam0(:,3),'r*');
%title('Plot of X v. Z coordinates of Reflected Beam Vector onto a
Spherical Screen');
%xlabel('X');
%ylabel('Z');
```

Appendix B

Mechanical Drawings of LIDAR Prototype

The following drawings were used by the Draper Labs Machine Shop to build the LIDAR prototype.
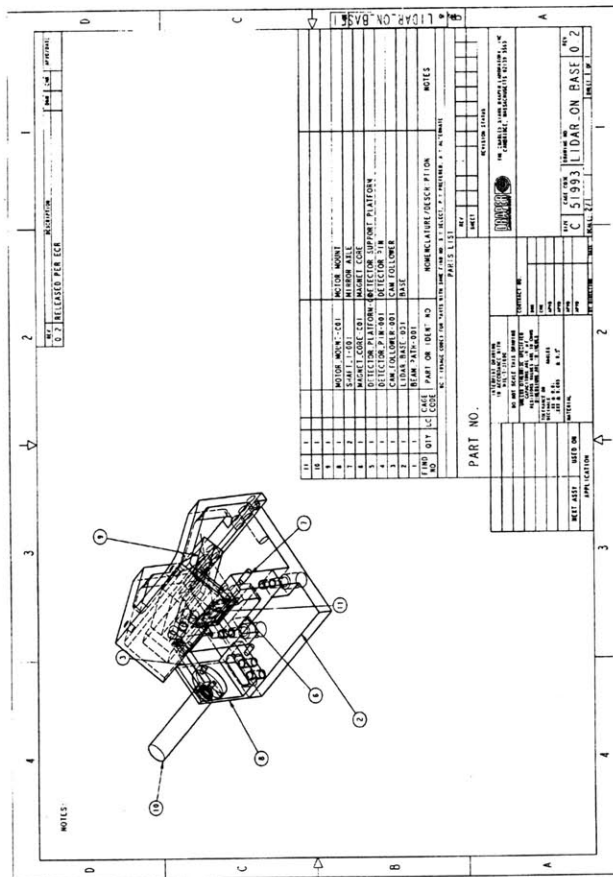
Figure B-1: LIDAR on base

Figure B-2: LIDAR base plate

Figure B-3: Magnet core
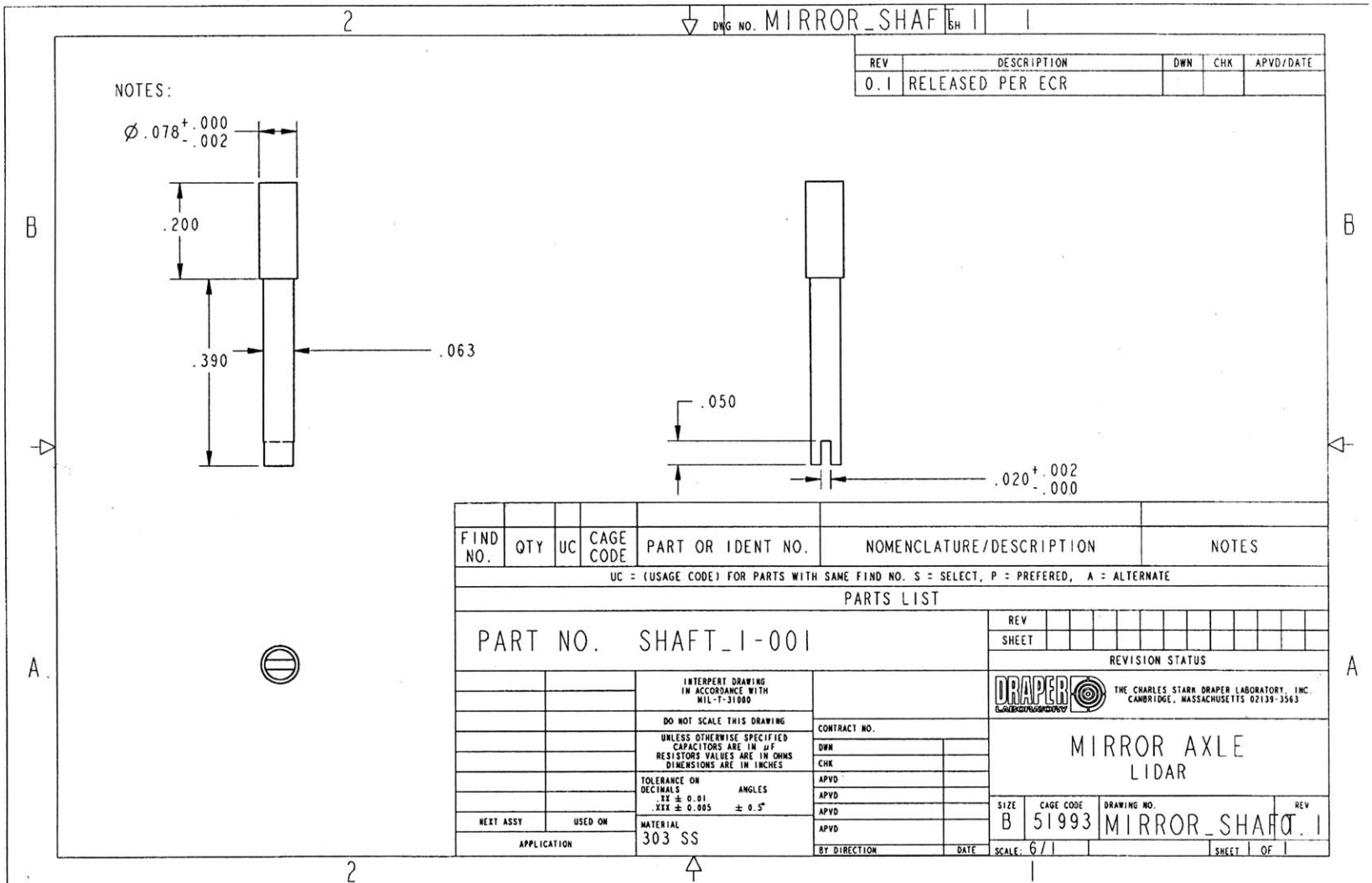
Figure B-4: MEMS outer frame post

NOTES:

METRIC M5 THREAD THRU

.90

.150

.60

.370

.120

.200

Ø.125

.40

.15

.40

PRESS FIT Ø0.062 STEEL PIN

1.20

.100

1.00

.050
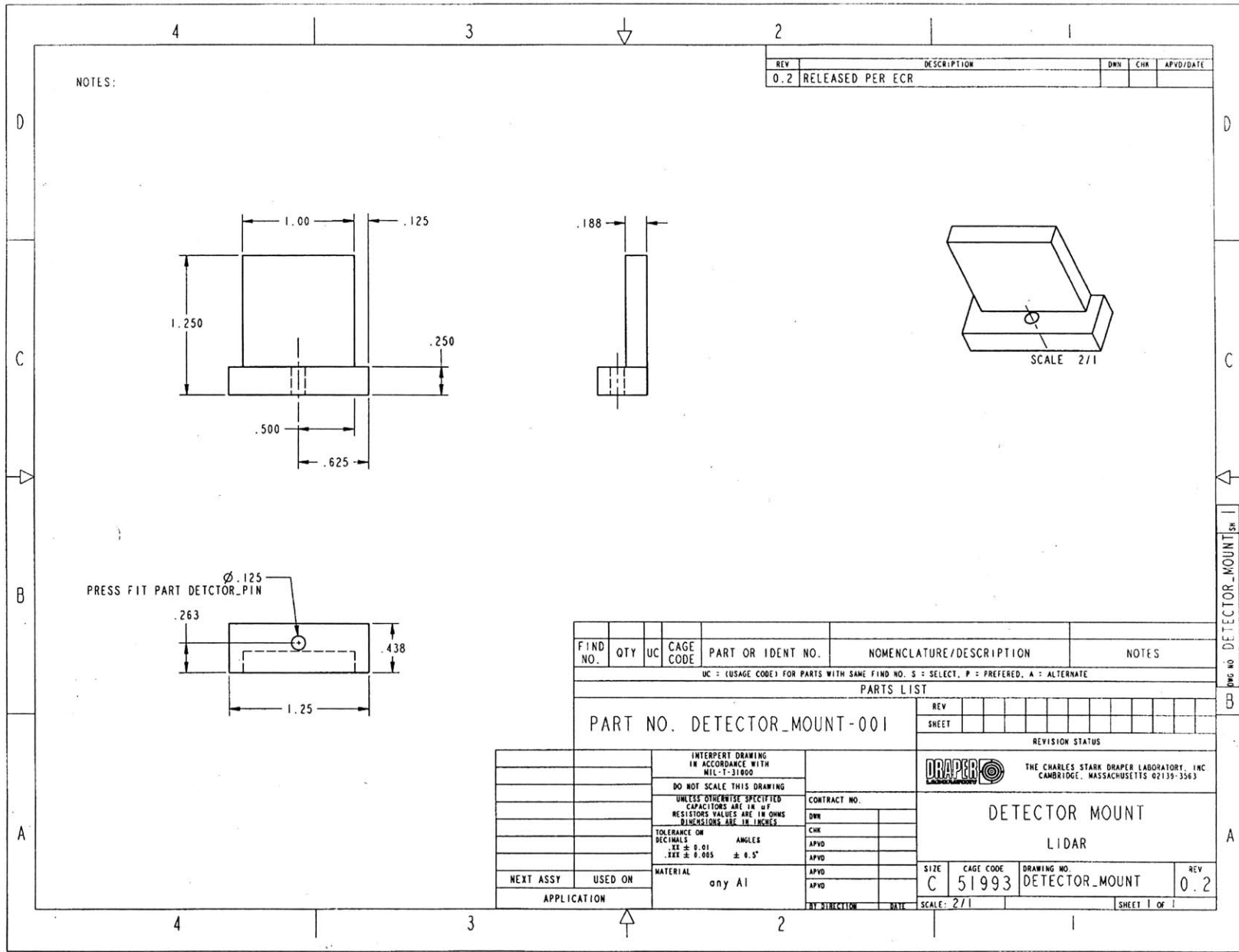
REV	DESCRIPTION	DWN	CHK	APVD/DATE
0.1	RELEASED PER ECR			

FIND NO.	QTY	UC	CAGE CODE	PART OR IDENT NO.	NOMENCLATURE/DESCRIPTION		NOTES
UC = (USAGE CODE) FOR PARTS WITH SAME FIND NO. S = SELECT, P = PREFERED, A = ALTERNATE							

PARTS LIST

PART NO.   MOTOR_MOUNT-001

	REV							
	SHEET							

REVISION STATUS

INTERPERT DRAWING IN ACCORDANCE WITH MIL-T-31000

DO NOT SCALE THIS DRAWING

UNLESS OTHERWISE SPECIFIED
CAPACITORS ARE IN µF
RESISTORS VALUES ARE IN OHMS
DIMENSIONS ARE IN INCHES

TOLERANCE ON
DECIMALS   ANGLES
.XX ± 0.01
.XXX ± 0.005   ± 0.5°

NEXT ASSY	USED ON	MATERIAL
APPLICATION		

CONTRACT NO.

DWN	
CHK	
APVD	
APVD	
APVD	
APVD	

BY DIRECTION   DATE

DRAPER
THE CHARLES STARK DRAPER LABORATORY, INC.
CAMBRIDGE, MASSACHUSETTS 02139-3563

MOTOR MOUNT
LIDAR

SIZE	CAGE CODE	DRAWING NO.		REV
B	51993	MOTOR_MOUNT	0.1	

SCALE: 2/1   SHEET 1 OF 1

Figure B-5: Motor mount

123

Figure B-6: Cam profile

REV	DESCRIPTION	DWN	CHK	APVD/DATE
0.1	RELEASED PER ECR			

NOTES:

$\emptyset .0785^{+.0005}_{-.0000}$

.720

.150

.075

.170

.100

PRESS FIT $\emptyset 0.062$ STEEL DOWEL PINS FOR THESE FEATURES

.250

.100

.390

.500

C   C

.010

CLEARANCE FOR #0-80

SECTION C-C

#0-80 THREAD

FIND NO.	QTY	UC	CAGE CODE	PART OR IDENT NO.	NOMENCLATURE/DESCRIPTION	NOTES
				UC = (USAGE CODE) FOR PARTS WITH SAME FIND NO. S = SELECT, P = PREFERED, A = ALTERNATE		
				PARTS LIST		

PART NO.   CAM_FOLLOWER-001

	REV	
	SHEET	
	REVISION STATUS	

INTERPERT DRAWING IN ACCORDANCE WITH MIL-T-31000

DO NOT SCALE THIS DRAWING

UNLESS OTHERWISE SPECIFIED CAPACITORS ARE IN µF RESISTORS VALUES ARE IN OHMS DIMENSIONS ARE IN INCHES

TOLERANCE ON
DECIMALS   ANGLES
.XX ± 0.01
.XXX ± 0.005   ± 0.5°

NEXT ASSY   USED ON   MATERIAL
7075 Al

APPLICATION

CONTRACT NO.

DWN
CHK
APVD
APVD
APVD
APVD

BY DIRECTION   DATE

DRAPER
THE CHARLES STARK DRAPER LABORATORY, INC.
CAMBRIDGE, MASSACHUSETTS 02139-3563

CAM FOLLOWER
LIDAR

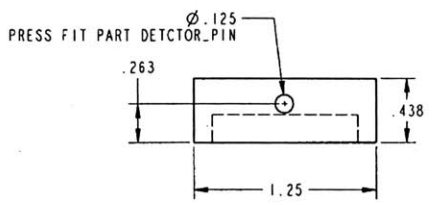| SIZE	CAGE CODE	DRAWING NO.	REV
B	51993	CAM_FOLLOWER.1	

SCALE: 5/1   SHEET 1 OF 1

Figure B-7: Cam arm with follower and spring pins

125

NOTES:

1.00   .125   .188

1.250   .250

.500

.625

SCALE 2/1

PRESS FIT PART DETCTOR_PIN
Ø.125

.263   .438

1.25

FIND NO.	QTY	UC	CAGE CODE	PART OR IDENT NO.	NOMENCLATURE/DESCRIPTION	NOTES

UC : (USAGE CODE) FOR PARTS WITH SAME FIND NO. S : SELECT, P : PREFERED, A : ALTERNATE

PARTS LIST

PART NO. DETECTOR_MOUNT-001

	REV														
	SHEET														

REVISION STATUS

INTERPERT DRAWING
IN ACCORDANCE WITH
MIL-T-31000

DO NOT SCALE THIS DRAWING

UNLESS OTHERWISE SPECIFIED
CAPACITORS ARE IN uF
RESISTORS VALUES ARE IN OHMS
DIMENSIONS ARE IN INCHES

TOLERANCE ON
DECIMALS   ANGLES
.XX ± 0.01
.XXX ± 0.005   ± 0.5°

MATERIAL
any Al

NEXT ASSY   USED ON

APPLICATION

CONTRACT NO.

DWN
CHK
APVD
APVD
APVD

DRAPER
LABORATORY
THE CHARLES STARK DRAPER LABORATORY, INC
CAMBRIDGE, MASSACHUSETTS 02139-3563

DETECTOR MOUNT

LIDAR

SIZE	CAGE CODE	DRAWING NO.	REV
C	51993	DETECTOR_MOUNT	0.2

BY DIRECTION   DATE   SCALE: 2/1   SHEET 1 OF 1

DWG NO DETECTOR_MOUNT SH 1
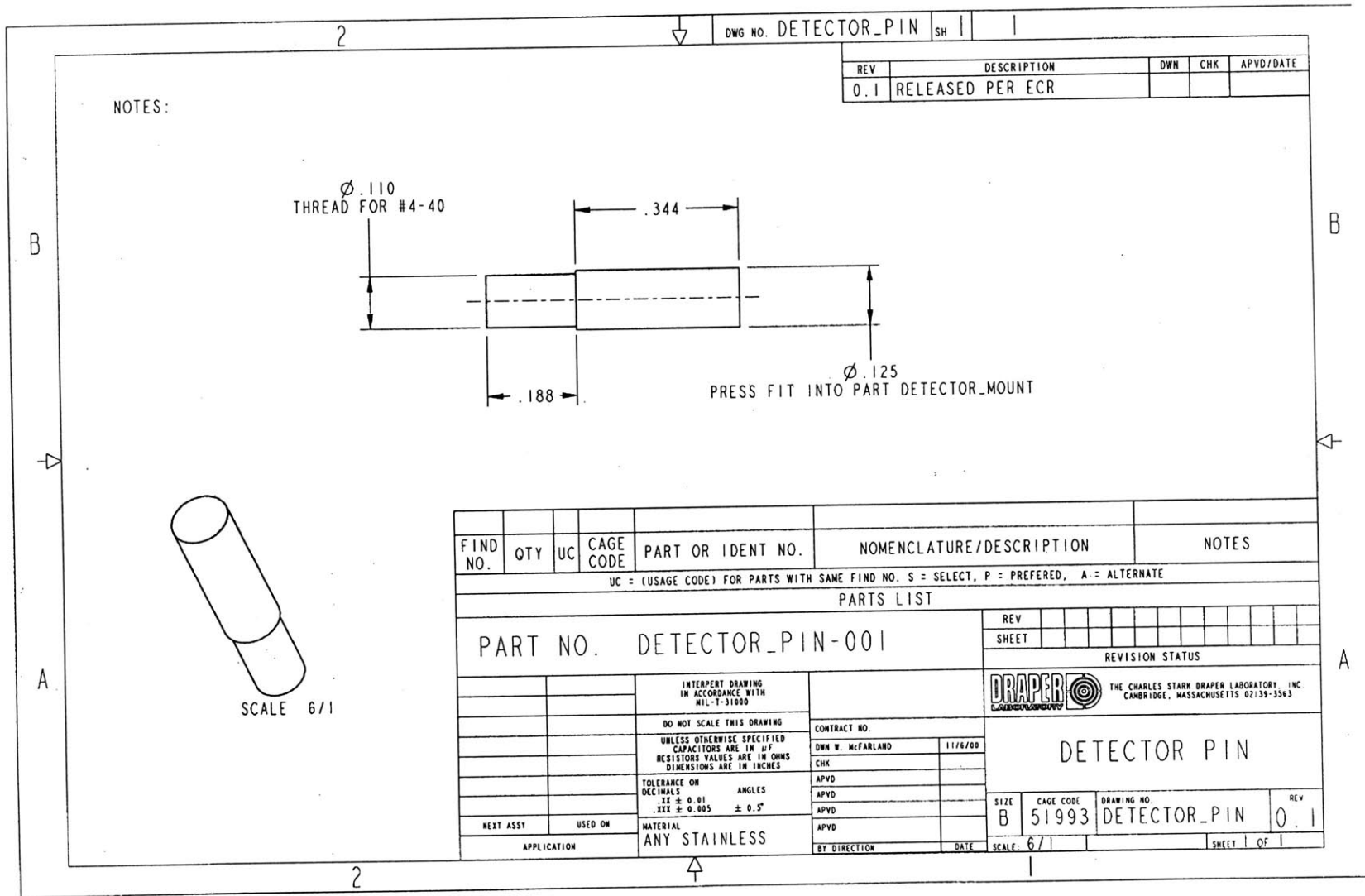
Figure B-8: Sensor mount

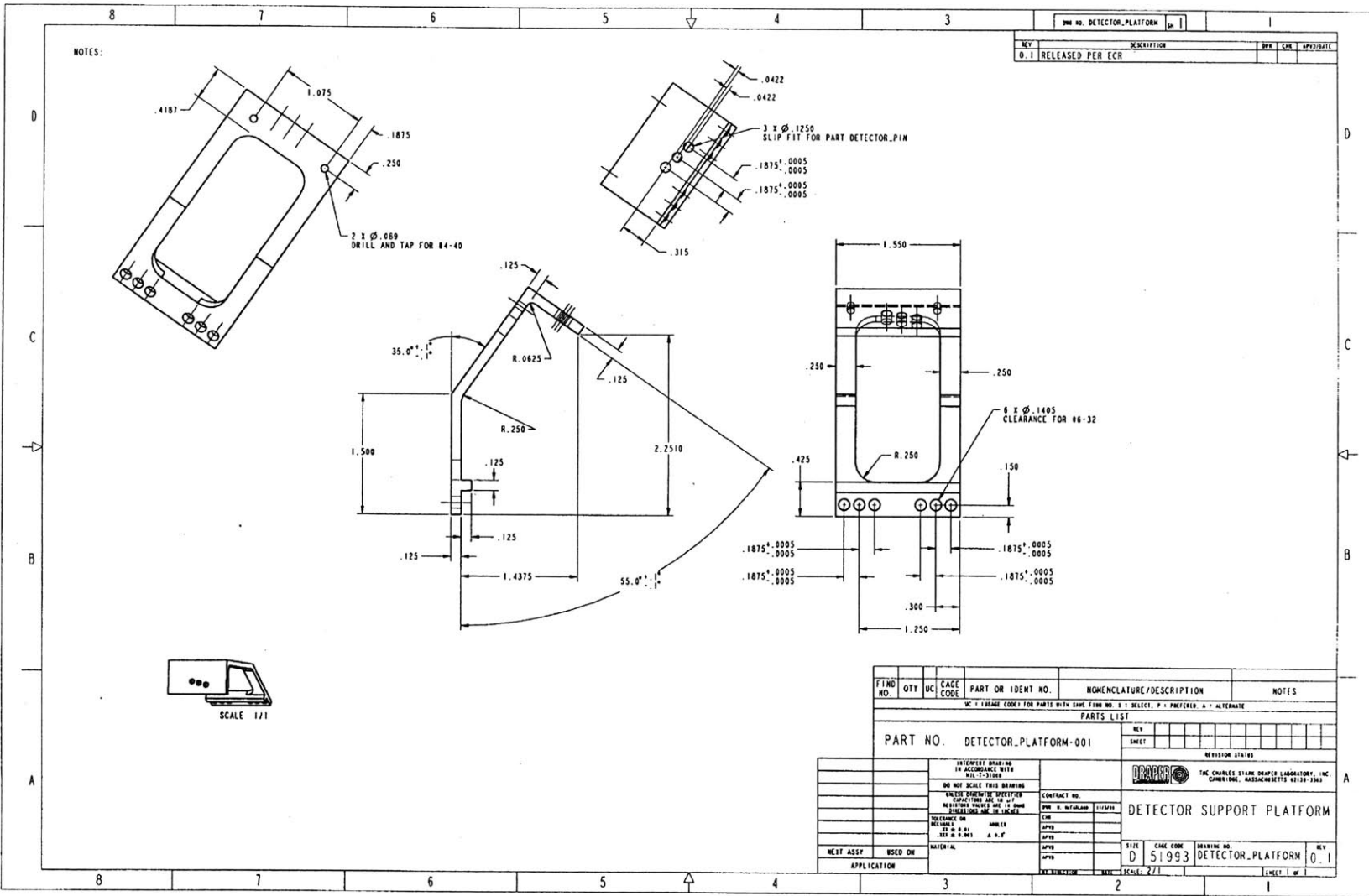Figure B-9: Sensor mount pin

127

Figure B-10: Sensor mount platform

128

Appendix C

Moment of Inertia Calculations

This appendix shows all the moment of inertia calculations relevant to the LIDAR system. The inertia calculations include the MEMS mirror assembly (outer frame, magnet, and mirror), the cam, cam arm, and the posts that connect the mirror to the cam arm.

C.1 MEMS Mirror Assembly

Calculating the moment of inertia tensor of the 2-axis mirror is a very involved process. The geometry, mass distribution, and rotational degrees of freedom of the 2-axis mirror must be analyzed. To begin the analysis, a brief description of the material and geometric construction of the 2-axis mirror will be presented. Figure C-1 shows a detailed picture of the 2-axis mirror set-up.

The 2-axis mirror contains two rotating bodies that are coupled by flexures (the thin lines in Figure C-1). For simplicity, it is assumed that the flexures are massless and frictionless, and all the bodies discussed are assumed to be rigid. The outer frame is composed of Silicon with density ρ_{Si}. The dimensions of the outer frame will be denoted by h_1, l_1, and w for the height, length and width of the outside part of the frame. The inside dimensions of the outer frame will be denoted by h_2, l_2, and w (the width of the outer frame is uniform). Although the figure shows small notches and bulges in the outer

frame, it will be assumed (to simplify calculations) that the outer frame has a uniform rectangular shape.
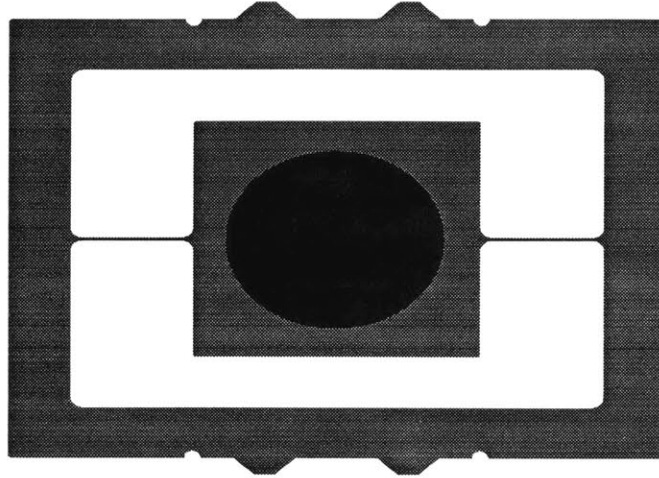

Figure C-1: 2-axis Mirror. Different Colors represent different material densities

The inner frame is composed of two different materials. The blue rectangular portion of the inner frame is composed of Silicon with density ρ_{Si} (identical to the outer frame material). It has dimensions h_i, l_i, and w (the width is the same as the outer frame). The circular black portion of the inner frame is the permanent magnet with density ρ_{mag}. It has a radius r and width w_{mag}.

The components of the moment of inertia tensor can be calculated by the following equation:

$$I_{ij} = \int_v \rho(\delta_{ij} \sum_{k=1}^{3} x_k^2 - x_i x_j) \, dv \qquad (C-1)$$

Where x_i are the integration variables along each of the dimensions of the mirror. The density ρ is defined as:

130

$$\rho = \frac{Mass}{Volume} \tag{C-2}$$

Fortunately, the geometry of the inner frame and outer frame have well known moment of inertia tensors and it is not necessary to re-derive them from basic principles. The inertia tensors for a rectangular solid (dimensions l, h, w and mass M) and a cylinder (radius r, width w and mass M) are given below. Figures C-2 and C-3 show the geometry of the rectangular solid and the cylinder in the fixed coordinate frame defined in chapter 4. The origin is located at the geometric center of the object (the geometric center is also the center of mass in this example).

$$\mathbf{I}_{rect} = \frac{\mathbf{M}}{12}\begin{bmatrix} h^2 + l^2 & 0 & 0 \\ 0 & h^2 + w^2 & 0 \\ 0 & 0 & l^2 + w^2 \end{bmatrix} \tag{C-3}$$
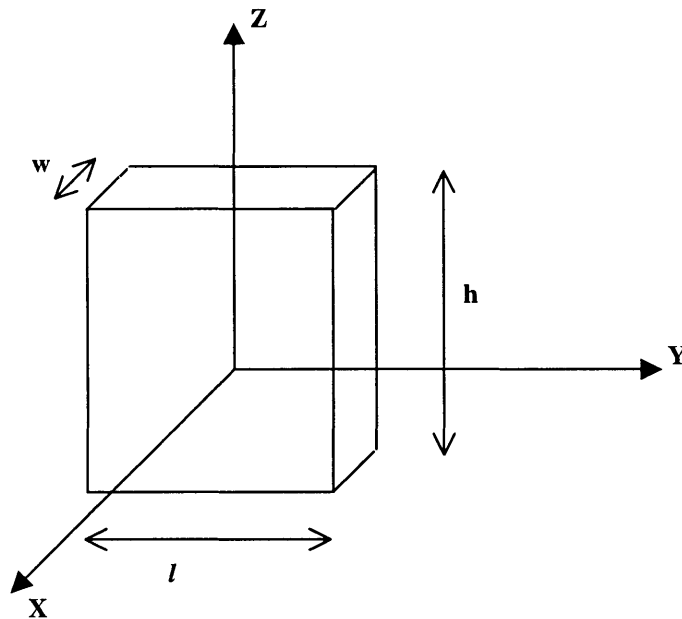

Figure C-2: Rectangular Solid in a Fixed Coordinate Frame

$$I_{cyl} = \frac{M}{2} \begin{bmatrix} r^2 & 0 & 0 \\ 0 & \frac{1}{6}(3r^2 + w^2) & 0 \\ 0 & 0 & \frac{1}{6}(3r^2 + w^2) \end{bmatrix} \qquad \text{(C-4)}$$
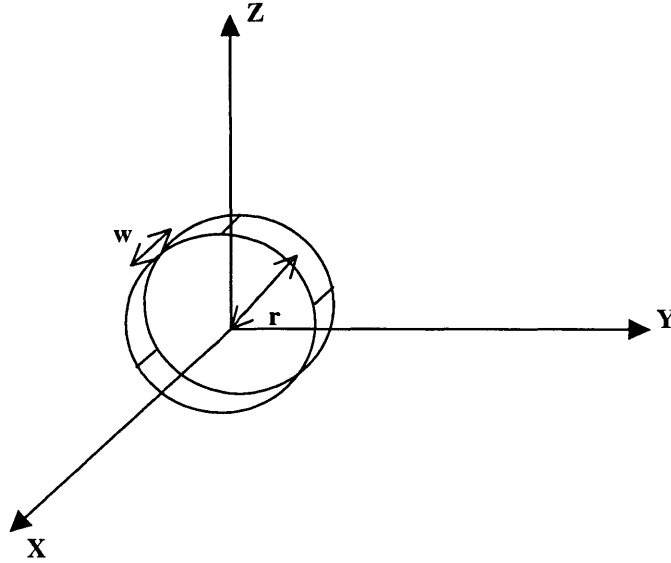

Figure C-3: Cylindrical Solid in a Fixed Coordinate Frame

The next step is to apply the principle of superposition with the moment of inertia tensors given above to generate a moment of inertia tensor for the inner axis of the 2-axis mirror. The inner axis body consists of a rectangular and a cylindrical portion. The total moment of inertia tensor of the inner body can be obtained with the following superposition equation:

$$I_{inner} = I_{rectin}(M_{Siin}, h_i, l_i, w) - I_{cyn}(M_{Sicyn}, r, w) + I_{cyn}(M_{mag}, r, w_{mag}) \qquad \text{(C-5)}$$

The notation $I(M,h,l,w)$ is a compact way to specify the parameters associated with a particular inertia tensor.

$$\mathbf{I}_{inner} = \begin{bmatrix} \mathbf{I}_1 & 0 & 0 \\ 0 & \mathbf{I}_2 & 0 \\ 0 & 0 & \mathbf{I}_3 \end{bmatrix} \qquad \text{(C-6)}$$

$$I_1 = \frac{1}{2}\left(\frac{M_{Siin}}{6}(h_i^2 + l_i^2) + r^2(M_{mag} - M_{Sicyn}) \right) \qquad \text{(C-7)}$$

$$I_2 = \frac{1}{12}\left(3r^2(M_{Mag} - M_{Sicyn}) + w^2(M_{Siin} - M_{Sicyn}) + M_{Siin}h_i^2 + M_{mag}w_{mag}^2\right) \quad \text{(C-8)}$$

$$I_3 = \frac{1}{12}\left(3r^2(M_{Mag} - M_{Sicyn}) + w^2(M_{Siin} - M_{Sicyn}) + M_{Siin}l_i^2 + M_{mag}w_{mag}^2\right) \quad \text{(C-9)}$$

Superposition is used again to find the inertia tensor for the outer frame, I_{frame}.

$$I_{frame} = I_{rect1}(M_{rectout1}, h_1, l_1, w_1) - I_{rect2}(M_{rectout2}, h_2, l_2, w_1) \qquad \text{(C-10)}$$

$$\mathbf{I}_{frame} = \begin{bmatrix} \mathbf{I}_{frame1} & 0 & 0 \\ 0 & \mathbf{I}_{frame2} & 0 \\ 0 & 0 & \mathbf{I}_{frame3} \end{bmatrix} \qquad \text{(C-11)}$$

$$I_{frame1} = \frac{1}{12}\left(M_{rectout1}(h_1^2 + l_1^2) - M_{rectout2}(h_2^2 + l_2^2)\right) \qquad \text{(C-12)}$$

$$I_{frame2} = \frac{1}{12}\left(M_{rectout1}(h_1^2 + w^2) - M_{rectout2}(h_2^2 + w^2)\right) \qquad \text{(C-13)}$$

$$I_{frame3} = \frac{1}{12}\left(M_{rectout1}(l_1^2 + w^2) - M_{rectout2}(l_2^2 + w^2)\right) \qquad \text{(C-14)}$$

The inertia calculations for the mirror is performed in using the same technique. Table C-1 summarizes the moments of inertia for the outer frame (denoted by I_{frame}), and the combined moment of inertia for the inner portion with the mirror surfaces and the magnet (denoted by I_{inner}) using the dimensions specified in chapter 2.

I_{frame1}	1.97×10^{-8} Kg-m^2
I_{frame2}	4.68×10^{-9} Kg-m^2
I_{frame3}	7.31×10^{-9} Kg-m^2
I_{inner1}	2.12×10^{-9} Kg-m^2
I_{inner2}	1.27×10^{-9} Kg-m^2
I_{inner3}	1.27×10^{-9} Kg-m^2

Table C-1: Summary of moments of inertia for MEMS assembly

C.2   Cam, Cam Arm, Motor Shaft, and MEMS Post

The cam is constrained to rotate in one direction, so the inertia calculation corresponds only to that rotation. The cam was using aluminum with a uniform thickness t. The inner radius of the cam will be denoted as R_i and the outer radius will be denoted as R_o. To simplify the calculation, it is assumed that the cam has a vertical return. Using that assumption, the radius of the cam can be written as a function of its angular position, θ.

$$r(\theta) = R_i + \frac{R_o - R_i}{2\pi}\theta \qquad \text{(C-15)}$$

The moment of inertia of the cam is easily calculated using polar coordinates, and solving the following equation:

$$I_{cam} = \rho_{al}t\int_0^{2\pi}\int_0^{r(\theta)} r^2(\theta)rdrd\theta \qquad \text{(C-16)}$$

Table C-2 lists the dimensions of the cam and the calculated moment of inertia.

ρ_{Al}	2700 Kg/m^3
t	2.23x10^{-3} m
R$_i$	4.37x10^{-3} m
R$_o$	9.45x10^{-3} m
I$_{cam}$	5.63x10^{-8} Kg-m^2

Table C-2: Dimensions and inertia of cam

The moment of inertia of the cam arm uses the parallel axis theorem. The cam arm is also constrained to rotate in only one direction, so all other moments are ignored. Figure C-4 shows the cam arm with the point of rotation labeled.

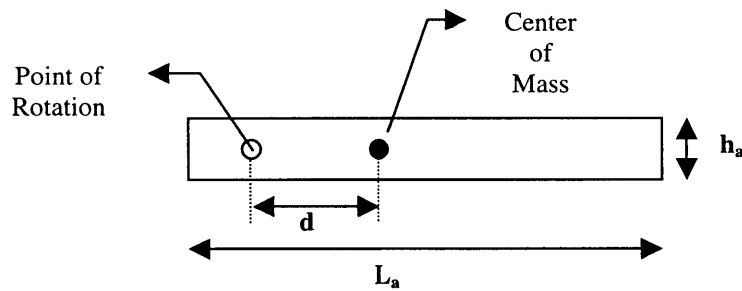Figure C-4: Cam arm

The cam arm is made with aluminum. The inertia calculation is shown below.

$$I_{arm} = \frac{1}{12} M_{arm} \left(L_a^2 + h_a^2 \right) + M_{arm} d^2 \qquad (C-17)$$

Table C-3 summarizes all the parameters in equation C-17.

M_{arm}	4.78×10^{-4} Kg
L_a	0.018 m
H_a	0.0038 m
d	0.0091 m
I_{arm}	5.39×10^{-8} Kg-m^2

Table C-3: Dimensions and inertia of cam arm

The inertia of the posts that attach to the frame of the MEMS mirror also are restricted to rotate in one direction. The post is an aluminum rod and has two sections. The section that sits in the electromagnet has a radius of R_i and the section that attaches to the cam arm has radius R_o. The inertia is calculated using equation C-18.

$$I_s = \frac{1}{2}(M_i R_i^2 + M_o R_o^2)$$
(C-18)

Table C-4 summarizes all the parameters in the above equation.

M_o	4.23×10^{-5} Kg
M_i	5.38×10^{-5} Kg
R_o	0.002 m
R_i	0.0016 m
I_s	1.21×10^{-11} Kg-m^2

Table C-4: Dimensions and inertia of posts

136

Appendix D

Method of Multiple Scales

Chapter 4 developed a complete model of the two-axis mirror system. Using the Euler-LaGrange method, the equations of motion for the system were derived. They are presented here again in equation 1 and 2.

$$\ddot{\theta}\left(I_{frame\,3} + I_1 \sin^2\varphi + I_3 \cos^2\varphi\right) + 2\,\dot{\varphi}\dot{\theta}(I_1 - I_3)\sin\varphi\cos\varphi + B_\theta\dot{\theta} = 0 \quad \text{(D-1)}$$

$$I_2\ddot{\varphi} + \dot{\theta}^2(I_3 - I_1)\sin\varphi\cos\varphi + k\varphi + B_\varphi\dot{\varphi} = 0 \quad \text{(D-2)}$$

Determining the solution to the above coupled, non-linear differential equations is essential to the design of a controller for the mirror system. There are many different analysis techniques available for non-linear systems, and each one exploits certain properties of the system. For the two-axis mirror system the method of multiple scales will be employed.

The method of multiple scales exploits the fact that certain non-linear systems can be described by more than one time scale. A simple example of a system with multiple time scales is a damped oscillator. Although it is not a non-linear system, it illustrates the main point of the method of multiple scales.

137

Consider the following second-order, linear differential equation with constant coefficients:

$$m\ddot{x} + b\dot{x} + kx = 0 \qquad \text{(D-3)}$$

The solution to this equation can be derived a number of ways using standard techniques. The solution to equation D-3 has the following general form:

$$x(t) = e^{-\alpha t}\left(C_1 \sin(\beta t) + C_2 \cos(\beta t)\right) \qquad \text{(D-4)}$$

Where α, β, C_1, and C_2 are constant functions of the initial conditions and the coefficients of equation D-3.

Equation D-4 describes a sinusoidal function with decaying amplitude. Figure D-1 shows an example of this function.
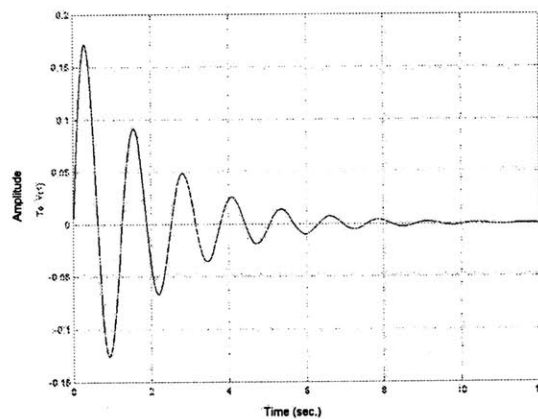
Figure D-1: Sinusoidal Oscillation with Exponentially Decaying Amplitude

In this example, there are two time scales that are of interest and importance. The first is the frequency that the system oscillates at. The second is the decay rate of the amplitude of the sinusoidal oscillations. Depending on the relative values of b and k in equation D-2, the decay rate and the oscillation frequency can occur on significantly different time

scales. If the amplitude decay rate is slow enough, it can be thought of as a constant value relative to the faster time scale of the sinusoid.

In non-linear systems, recognizing multiple time scales for the system can simplify the problem. In the 2-Axis MEMS mirror system, the outer axis is a slow moving axis whereas the inner mirror axis oscillates at a much higher frequency. It is a natural choice to use the method of multiple scales.

The method of multiple scales is an extension of perturbation analysis typically used in non-linear systems. The method of multiple scales does not impose a limit to the number of time scales that can be used. It is a natural choice to chose 2 time scales for this analysis.

The first step in the method of multiple scales is to define the new time scales for the system. The two scales will be labeled as a fast time scale and a slow time scale. Each time scale will be treated as independent variables.

$$let \qquad \gamma = t \qquad\qquad\qquad \text{(D-5)}$$

$$T = \varepsilon t \qquad\qquad\qquad \text{(D-6)}$$

Under the new time scales, functions of the slow time T are considered constant relative to the fast time scale γ.

At this point, equations D-1 and D-2 must be manipulated and some constants will be defined to ease the remainder of the method calculations. The first step is to apply a small angle approximation to eliminate the cosine and sine terms in the equations. This is a valid approximation for this system because the outer axis only sweeps through $\pm 12.5°$ and the inner axis only sweeps through $\pm 6.25°$.

$$\ddot{\theta}\left(I_{frame\,3} + I_1\varphi^2 + I_3\right) + 2\,\dot{\varphi}\dot{\theta}(I_1 - I_3)\,\varphi + B_\theta\dot{\theta} = 0 \qquad \text{(D-7)}$$

$$I_2\ddot{\varphi} + \dot{\theta}^2(I_3 - I_1)\,\varphi + k\varphi + B_\varphi\dot{\varphi} = 0 \qquad \text{(D-8)}$$

Next, some algebraic manipulation will give a more intuitive form of the equations.

$$\ddot{\theta} + \frac{I_1}{I_{frame\,3} + I_3}\varphi^2\ddot{\theta} + 2\frac{I_1 - I_3}{I_{frame\,3} + I_3}\varphi\dot{\varphi}\dot{\theta} + \frac{B_\theta}{I_{frame\,3} + I_3}\dot{\theta} = 0 \qquad \text{(D-9)}$$

$$\ddot{\varphi} + \frac{I_3 - I_1}{I_2}\dot{\theta}^2\varphi + \frac{k}{I_2}\varphi + \frac{B_\varphi}{I_2}\dot{\varphi} = 0 \qquad \text{(D-10)}$$

From equations D-9 and D-10 the natural frequency of the inner axis can be determined in addition to the quality factor of both axes (Q value).

$$\omega_\varphi = \sqrt{\frac{k}{I_2}} \qquad \text{(D-11)}$$

$$Q_{\theta\varphi} = \frac{\omega_\varphi(I_{frame\,3} + I_3)}{B_\theta} \qquad \text{(D-12)}$$

$$Q_\varphi = \frac{\omega_\varphi I_2}{B_\varphi} \qquad \text{(D-13)}$$

Using the constants defined in equations D-11 through D-13, equations D-9 and D-10 can be re-written in a cleaner form.

$$\ddot{\theta} + \frac{I_1}{I_{frame3} + I_3} \varphi^2 \ddot{\theta} + 2 \frac{I_1 - I_3}{I_{frame3} + I_3} \varphi \dot{\varphi} \dot{\theta} + \frac{\omega_\varphi}{Q_{\theta\varphi}} \dot{\theta} = 0 \qquad \text{(D-14)}$$

$$\ddot{\varphi} + \frac{I_3 - I_1}{I_2} \dot{\theta}^2 \varphi + \omega_\varphi^2 \varphi + \frac{\omega_\varphi}{Q_\varphi} \dot{\varphi} = 0 \qquad \text{(D-15)}$$

Finally, before the method of multiple scales can be applied, equations D-14 and D-15 should be normalized to a specified time unit. The normalization of the equations will create a unitless pair of equations.

The normalization variable will be defined as follows:

$$\tau = \omega_\varphi t \qquad \text{(D-16)}$$

Using the new time scale and some more algebraic manipulation, equations D-14 and D-15 become:

$$\theta'' + \frac{I_1}{I_{frame3} + I_3} \varphi^2 \theta'' + 2 \frac{I_1 - I_3}{(I_{frame3} + I_3) \omega_\varphi} \varphi \varphi' \theta' + \frac{1}{Q_{\theta\varphi}} \theta' = 0 \qquad \text{(D-17)}$$

$$\varphi'' + \frac{I_3 - I_1}{I_2} \theta'^2 \varphi + \varphi + \frac{1}{Q_\varphi} \varphi' = 0 \qquad \text{(D-18)}$$

In order to simplify the notation, primes are used to denote differentiation with respect to the new time scale τ.

The next step in the method of multiple scales is to determine the small parameter value to be used in the perturbation model, and define appropriate constants using that

parameter. For this system, the small parameter will be the inverse of Q_φ. The constants are given below.

$$\varepsilon = \frac{1}{Q_\varphi} \tag{D-19}$$

$$\frac{I_1}{I_{frame3} + I_3} = \varepsilon\alpha \tag{D-20}$$

$$2\frac{I_1 - I_3}{(I_{frame3} + I_3)\omega_\varphi} = \varepsilon\beta \tag{D-21}$$

$$\frac{I_3 - I_1}{I_2} = \varepsilon\chi \tag{D-22}$$

Rewriting equations D-17 and D-18 with the new constants yields a very compact representation of the equations.

$$\theta'' + \varepsilon\theta' + \varepsilon\left(\alpha\varphi^2\theta'' + \beta\varphi\varphi'\theta'\right) = 0 \tag{D-23}$$

$$\varphi'' + \varphi + \varepsilon\varphi' + \varepsilon\left(\chi\theta'^2\varphi\right) = 0 \tag{D-24}$$

By using order of magnitude arguments, the coupling terms in equation D-23 and D-24 can be ignored. The terms $\varepsilon\alpha$, $\varepsilon\beta$, and $\varepsilon\chi$ are much smaller then ε and can be eliminated. Therefore, the system equations can be expressed as two uncoupled linear equations.

$$\theta'' + \varepsilon\theta' = 0 \tag{D-25}$$

$$\varphi'' + \varphi + \varepsilon\varphi' = 0 \tag{D-26}$$

References

[1] Barger, Vernon and Martin Olsson Classical Mechanics: A Modern Perspective McGraw-Hill, Inc. : New York, 1995.

[2] Conant, R. A. and R. S. Muller, et. Al., A Flat High-Frequency Scanning Micromirror, Hilton Head, 2000.

[3] Crandall, Stephen and Dean Karnopp and Edward Kurtz, JR. and David Pridmore-Brown, Dynamics of Mechanical and Electromechanical Systems Krieger Publishing Company: Malabar, Florida, 1968.

[4] Gould, L.A., and W. R. Markey and J. K. Roberge, and D. L. Trumper Control Systems Theory M. I. T. Course Notes, 1994.

[5] Graeme, Jerald G. Photodiode Amplifiers: Op Amp Solutions McGraw-Hill, Inc.: New York, 1996.

[6] Horowitz, Paul and Winfield Hill The Art of Electronics Cambridge University Press: Cambridge, 1989.

[7] Hutchins, Christopher D. Dynamic Analysis of a Gyroscope with an Oscillating Momentum Vector Masters Thesis, Massachusetts Institute of Technology, Department of Mechanical Engineering, (C.S. Draper Laboratory, CSDL-T-887), Aug. 1985.

[8] Ikeda, M., and H. Goto, and H. Totani, and M. Sakata, and T. Yada Two-Dimensional Miniature Optical-Scanning Sensor with Silicon Micromachined Scanning Mirror, *Miniaturized Systems with Micro-Optics and Micromechanics II, Proc. SPIE* vol 3008, 1997.

[9] Marion, Jerry B. and Stephen T. Thornton <u>Classical Dynamics of Particles and Systems</u> Saunders College Publishing: Fort Worth 1995.

[10] Meriam, J.L. and L.G Kraige, <u>Engineering Mechanics Volume 2: Dynamics</u> John Wiley & Sons, Inc.: New York, 1992.

[11] Miller, R. and Y. Tai, <u>Micromachined Electromagnetic Scanning Mirrors</u>, *Optical Engineering*, SPIE vol 36(5), 1997.

[12] Nayfeh, Ali Hasan and Dean Mook <u>Nonlinear Oscillations</u> John Wiley & Sons, Inc.: New York, 1995.

[13] Phan, Long N., <u>Collision Avoidance Via Laser Rangefinding</u>, Bachelor and Masters Thesis, Massachussetts Institute of Technology, Department of Mechanical Engineering, (C.S. Draper Laboratory, CSDL-T-1343), May, 1999.

[14] Purcell, Edward M. <u>Electricity and Magnetism</u> McGraw-Hill, Inc.: New York, 1985.

[15] Strang, Gilbert <u>Introduction to Applied Mathematics</u> Wellesley-Cambridge Press: Wellesley, MA 1986.

[16] Young, Hugh D. <u>University Physics</u> Addison-Wesley Publishing Company: Reading, MA 1992.

[17] Zahn, Markus, <u>Electromagnetic Field Theory: A Problem Solving Approach</u>, Wiley: New York, 1979.